Eindhoven University of Technology

MASTER

Thermally stable Pd-based ceria-zirconia mixed oxides for the CO oxidation and NO reduction

Snoeckx, W.

Award date:
2019

Link to publication

Department of Chemical Engineering and Chemistry

Inorganic Materials & Catalysis Research Group

Thermally stable Pd-based ceria-zirconia mixed oxides for the CO oxidation and NO reduction

Graduation report of

Wesley Snoeckx

Supervisors:

Valerii Muravev

Dr. rer. nat. J.P. Hofmann

Prof. dr. ir. E.J.M. Hensen

Committee:

Dr. T. Noël

Eindhoven, The Netherlands, May 2019

Abstract

This work investigates the preparation of thermally stable ceria-zirconia-based mixed oxides and their catalytic performance in the $CO + O_2$ and $CO + NO$ reactions. In recent years, many studies have been focusing on the synthesis of highly active catalysts for the oxidation of CO and the reduction of NO to counter the adverse effects of gasoline-fueled vehicles on human health and the environment. Less attention, however, has been paid to their thermal stability, while it is crucial to prevent the sintering of the active phase in order to increase the lifetime of these catalysts. Thus, this work aims at the synthesis of catalysts that are both thermally stable and show high activity towards the oxidation of CO and the reduction of NO.

The synthesis of highly stable ceria-zirconia-based solid solutions is reported in Chapter 2. For this purpose, a one-step polymer-assisted sol-gel method was employed. Various transition metals (Fe, Cu, Co, Cr, Ni and Pd) with different loadings were used for doping of the ceria-zirconia support, after which the catalysts were calcined at 500 °C and 800 °C. The textural and structural properties of these solid solution systems were determined by a number of analysis methods, including X-ray diffraction (XRD), transmission electron microscopy (TEM) and N_2 physisorption. The surface composition and chemical state of the different transition metal dopants were examined by X-ray photoelectron spectroscopy (XPS). The presence of segregated oxide phases was further investigated by UV-Vis measurements, while extended X-ray absorption fine structure (EXAFS) measurements were performed to gain more insight into the local structure around the transition metal dopants. Finally, the reducibility of the catalysts was investigated by H_2-TPR analysis. It was found that sol-gel synthesized ceria-zirconia-based solid solutions exhibited high thermal stability. In particular, 1PdCZ was found to be stable at 800 °C, while earlier studies have reported that PdO in ceria-related materials thermally decomposes into metallic Pd at such high temperatures.

Chapter 3 describes the synthesis of non-noble metal and Pd-based ceria-zirconia mixed oxides, followed by their catalytic activity testing for the oxidation of CO and the reduction of NO. Various characterization techniques, such as XPS, DRIFTS and H_2-TPR, were used to identify the active phase in these catalysts for the $CO + O_2$ and $CO + NO$ reactions. It was found that the Pd-impregnated catalysts generally performed better in the $CO + O_2$ reaction compared to the Pd-doped samples, while the opposite was found to be true for the $CO + NO$ reaction.

Contents

Chapter 1

Introduction

1. Heterogeneous catalysis

By definition, a catalyst is a substance that alters the rate of a reaction without being consumed or modified by it. Provided with a different pathway with a lower activation energy, the reaction can proceed more rapidly than in the absence of a catalyst. Furthermore, the selectivity of the reaction can also be improved in the presence of catalysts in order to prevent the formation of side products. This has significant economic impact on the chemical industry. In this way, the use of catalysts is indispensable for nearly every industrial chemical process, as they allow reactions to occur more efficiently and cost-effectively. In the majority of these processes, heterogeneous catalysts are preferred over homogeneous catalysts, even though the latter provide excellent activity and selectivity. This is related to the difficulty of catalyst separation from the products typical for homogeneous catalysis, resulting in a higher overall processing cost. In addition, homogeneous catalysts are often thermally and mechanically less stable than heterogeneous analogues, thereby limiting their use in industrial processes that involve high temperatures and pressures.

One of the simplest examples of heterogeneous catalysis in industry is the oxidation of CO by molecular oxygen on the surface of a solid state catalyst. This catalytic reaction has been extensively studied because of its many applications, the most important of which is air purification. In particular, the catalytic oxidation of CO is one of the key reactions in three-way catalytic converters (TWCs), which are used to convert pollutants in automotive exhausts into less harmful compounds:

$$2CO + O_2 \rightarrow 2CO_2$$
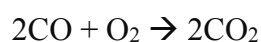
A simplified potential energy diagram of this reaction is illustrated in Figure 1.1 (adapted from [1]). Even though the oxidation of CO by O_2 is a fairly exothermic reaction, the reaction does not occur in the gas phase under ambient conditions due to a high activation energy barrier. In the absence of the catalyst, the activation energy for breaking the O-O bond in the gas phase is approximately 560 kJ/mol. In the presence of a catalyst,
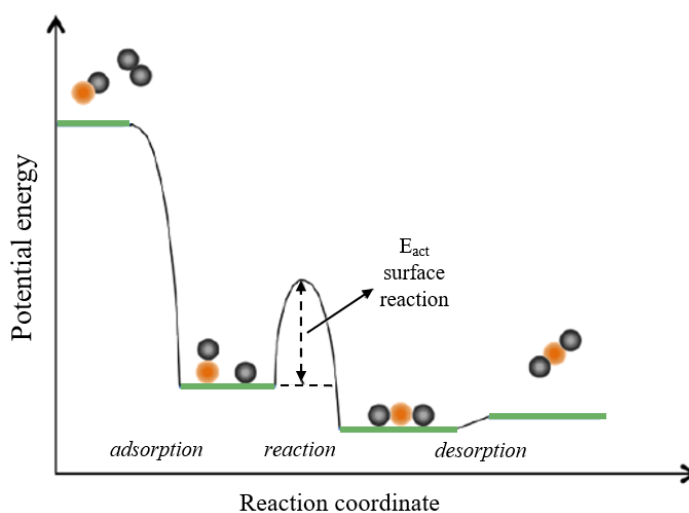

Figure 1.1: Potential energy diagram of the $CO + O_2$ reaction on a catalyst surface. After the adsorption on the catalyst, a surface reaction takes place between the reactants, leading to the product that is desorbed in the final step. Orange = carbon, grey = oxygen. Adapted from [1].

however, the O_2 molecule can dissociate relatively easily on the catalyst surface with a significantly reduced activation energy, thereby allowing the CO oxidation reaction to proceed under ambient conditions. It has been shown in literature that transition metals, and in particular platinum-group metals, are highly efficient in catalyzing the dissociation of the O-O bond [2–4]. Before the actual cleavage of the oxygen molecular bond, both CO and O_2 adsorb on the metal catalyst surface in the first step of the reaction mechanism. After the dissociation of O_2, the reactants subsequently diffuse on the catalyst surface leading to the formation of a reactive surface complex when an oxygen atom encounters a CO molecule. In the final step, the catalyst surface is regenerated through desorption of CO_2, whereupon a new catalytic cycle is initiated. Figure 1.2 (adapted from [1]) shows the catalytic cycle of the CO oxidation reaction in more detail.
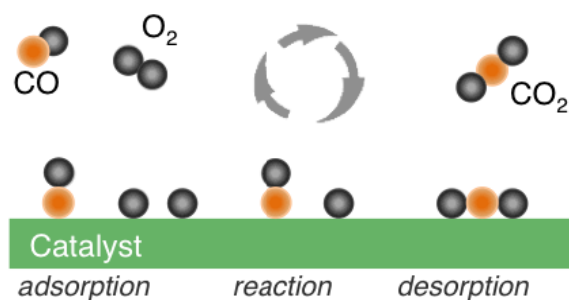
Figure 1.2: Catalytic cycle for the CO oxidation by O_2 over a catalyst surface. Orange = carbon, grey = oxygen. Adapted from [1].

The reaction mechanism described above for the CO oxidation by molecular oxygen is called the Langmuir-Hinshelwood mechanism. In this mechanism, both reactants first adsorb on the catalyst surface, and after reacting with each other the product desorbs from the surface in the final step. A second mechanism, however, also exists for this reaction depending on the support material that is used. For example, when a reducible oxide such as ceria (CeO_2) is used as the support material, the reaction might proceed via the Mars-Van Krevelen mechanism. According to this mechanism, the oxygen atom in the resulting CO_2 molecule is coming from the support itself, leading to the formation of an oxygen vacancy on the surface of the reducible oxide [5,6]. In a final step, the vacancy can be restored via the adsorption of molecular oxygen from the gas phase, after which the catalytic cycle can repeat itself. Figure 1.3 shows a simplified scheme of the Mars-Van Krevelen mechanism for platinum nanoparticles supported on a reducible oxide [7].
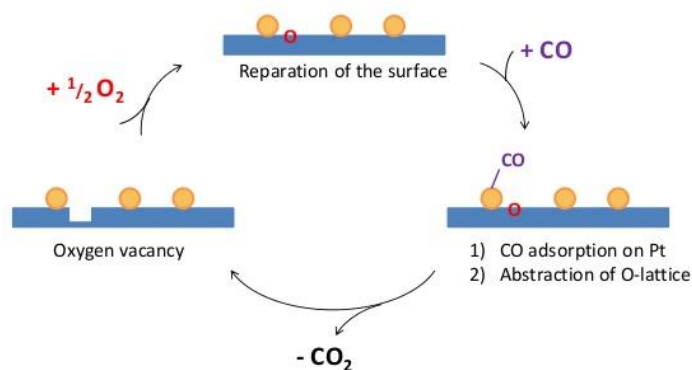
Figure 1.3: Simplified scheme of the Mars-Van Krevelen mechanism. After the desorption of CO_2, the oxygen vacancy formed on the surface of the support is replenished by gaseous O_2. Copied from [7].

As illustrated by the Mars-Van Krevelen mechanism, the nature and structure of the reducible support can strongly influence the catalytic performance. The support further plays an important role in heterogeneous catalysis by enhancing the thermal and mechanical stability of the catalyst. Anchoring sites on the surface of the support can effectively stabilize the active phase, which typically consists of supported noble metal nanoparticles which are prone to sintering [8,9]. The stabilization of these particles by the support is crucial in order to prevent catalyst deactivation due to the loss of available active sites and thus to improve the efficiency of many important heterogeneous catalytic reactions in the chemical industry. Conclusively, it is clear that the interaction between the metal and the support is of great importance for the majority of heterogeneous catalytic processes. Hence, optimization of the already existing synthesis methods and development of entirely new ones in order to enhance the metal-support interaction – is in the spotlight of the catalysis community.

2. Automotive exhaust gas emissions

Concerns about air pollution and global warming have become increasingly prominent in transport policy decision-making, leading to extensive research in recent years on the development of highly active three-way catalytic converters (TWCs). These TWCs are able to convert environmental pollutants from automobile exhausts into less harmful compounds. As the fuel combustion is not completely efficient, unburnt hydrocarbons and partially combusted compounds such as ketones, aldehydes and carboxylic acids are formed. These compounds denoted by HC, represent one of the three major pollutants in gasoline engine exhausts. The second main pollutant in the exhaust is carbon monoxide (CO), which also originates from an incomplete fuel combustion:

Fuel (hydrocarbons) $+ O_2 \rightarrow H_2O + CO$ (1)
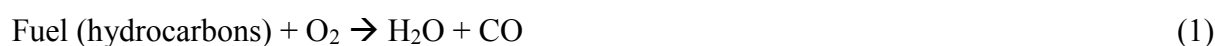
The last main pollutants present in gasoline exhausts are nitrogen oxides (NO_x). They are formed by the thermal recombination of N_2 and O_2 from air due to the high temperatures reached by the fuel combustion (reaction (2)), followed by their partial oxidation by O_2 in the vehicle tailpipe (reaction (3)):

$N_2 + O_2 \rightarrow 2\ NO$ (2)

$NO + \frac{1}{2}\ O_2 \rightarrow NO_2$ (3)

In order to prevent the emission of HC, CO and NO_x, TWCs are implemented in the vehicle tailpipe for converting these hazardous pollutants into less harmful compounds. In particular, HC and CO are oxidized to carbon dioxide (CO_2) in reaction (4) and (5), while nitrogen oxides (NO_x) are simultaneously reduced to molecular nitrogen (N_2) in reaction (6) and (7) [10]. In addition, a direct reaction also occurs between HC and NO, as illustrated in reaction (8). The presence of H_2 in the exhaust can be explained by the WGS reaction and reforming processes occurring in the catalytic converter.

$HC + O_2 \rightarrow CO_2 + H_2O$ (4)

$$CO + \frac{1}{2} O_2 \rightarrow CO_2 \qquad\qquad (5)$$

$$CO + NO \rightarrow N_2 + CO_2 \qquad\qquad (6)$$

$$NO + H_2 \rightarrow N_2 + H_2O \qquad\qquad (7)$$

$$HC + NO \rightarrow N_2 + CO_2 + H_2O \qquad\qquad (8)$$

$$H_2 + \frac{1}{2} O_2 \rightarrow H_2O \qquad\qquad (9)$$

TWCs were first implemented in the second half of the twentieth century, when human health problems related to air pollution started to emerge due to the increased use of vehicles [11]. The 1970 Clean Air Act that was mandated in the United States is an important example of the need for catalytic converters in the automobile industry. This act demanded the reduction of HC, CO and NO amounts by 90% in automotive exhaust gases, leading to the development of Pt/Pd catalysts in the late 1970s that could successfully remove 90% HC and CO from the exhausts by oxidizing them to less harmful compounds [12]. In the middle 1980s, the first catalyst was commercialized that could simultaneously abate HC, CO and NO_x to a great extent by employing a dual-bed converter. The simultaneous catalytic removal of these three major pollutants from the exhaust explains why these catalysts are called 'three-way' catalysts. Conclusively, the 1970 Clean Air Act can be considered as a decisive turning point in climate policies, resulting in the increased authority enforcement of the Environmental Protection Agency (EPA) for fighting environmental pollution.

TWCs typically consist of a ceramic monolith of cordierite with a honeycomb structure, loaded with a 20-150 μm thin layer of a cerium-based oxide with high surface area and oxygen storage properties, one or more noble metals and, lastly, often a metal oxide promotor [11].
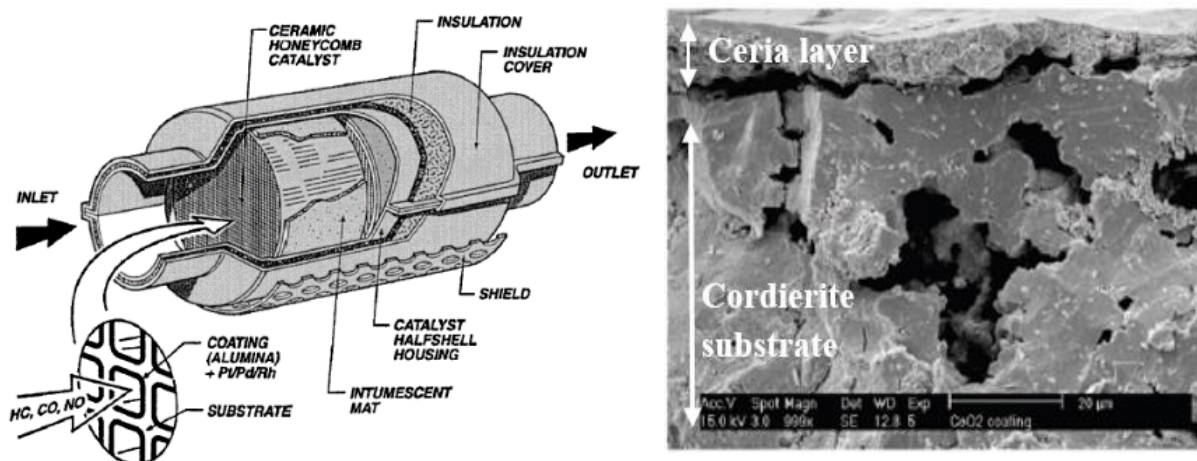
Figure 1.4: Schematic representation of an automotive catalyst (left) and SEM microscopy picture of a cordierite substrate coated with a ceria layer (right). Left figure: copied from [14], right figure: adapted from [12].

The usefulness and importance of ceria (CeO_2) in TWCs was first envisaged by scientists at Ford Motor Company in 1976 when they demonstrated the superior oxygen storage capacity (OSC) of CeO_2 compared to other metal oxides [13]. More specifically, CeO_2 is able to store

significant amounts of oxygen atoms in its lattice under fuel-lean (net oxidizing) conditions. Consequently, due to the reversible Ce^{4+}/Ce^{3+} redox couple, CeO_2 is able to assist the oxidation of HC and CO under fuel-rich (net reducing) conditions by providing its lattice oxygen. In this way, CeO_2 acts as an oxygen buffer to prevent perturbations on the catalyst and to keep the air-to-fuel (A/F) ratio at a stoichiometric value of A/F=14.6, which is necessary for the efficient operation of the TWC [14]. From this it follows that higher conversion efficiencies can be achieved with catalysts showing higher OSCs. Other benefits of using CeO_2 as the support material include the stabilization of the active noble metal in a form of single-atoms [15,16], the promotion of the water gas shift [17] and steam reforming reactions [18], the increase of the thermal stability of the alumina support and favoring catalytic activity at the interface of the metal and CeO_2 [19].

The main active components of TWCs are the noble metals, for which platinum-group metals are typically used. Osmium (Os), iridium (Ir) and ruthenium (Ru), however, cannot be used in TWCs due to the high volatility of their oxides leading to metal loss at high temperatures. Conversely, platinum (Pt), rhodium (Rh) and palladium (Pd) remain metallic under the operating conditions of TWCs, explaining their predominant use in catalytic converters. As Pd is less noble than Pt and Rh, Pd is more prone to poisoning by lead and sulfur, which are both present in gasoline and diesel. Nevertheless, Pd is more preferred due to its higher availability and lower cost as compared to Pt and Rh. After a decrease in lead concentrations in fuel in the 1980s, the more expensive Pt could partially be substituted by Pd, eventually leading to the successful commercialization of Pd/Rh catalysts in 1989 [20]. A combination of two noble metals is often used to ensure that both oxidation and reduction reactions take place: Pt and Pd primarily promote the oxidation of CO and HC, while the reduction of NO_x is most efficiently catalyzed by Rh [11].

The persistent use of Rh in TWCs can partially be explained by the segregation of Pd as PdO on the catalyst surface under oxidizing conditions [21]. Because of this segregation phenomenon the conversion of NO_x remains suppressed at lower temperatures. The reduced conversion efficiency of Pd for NO_x as compared to Rh is clear from Figure 1.5, which shows only a narrow NO_x window for a Pd-based catalyst [20]. Thus it can be concluded that the NO_x conversion by Pd will decrease significantly under fuel-lean or fuel-rich operating conditions [22]. This problem of Pd-only catalysts was mainly solved in the 1990s when solid solutions of CeO_2 with ZrO_2 were prepared for increasing the overall thermal durability of TWCs [23]. This was one of the demands imposed by the new emission regulations that time. An additional benefit that was observed after doping with ZrO_2 was the enhanced OSC of the TWC. This enhancement could be explained by the promoted oxygen transport in the bulk of the support resulting in more effective Pd-only catalysts, as the more easily formed oxygen vacancies appear to play a crucial role in the conversion of NO_x [23].
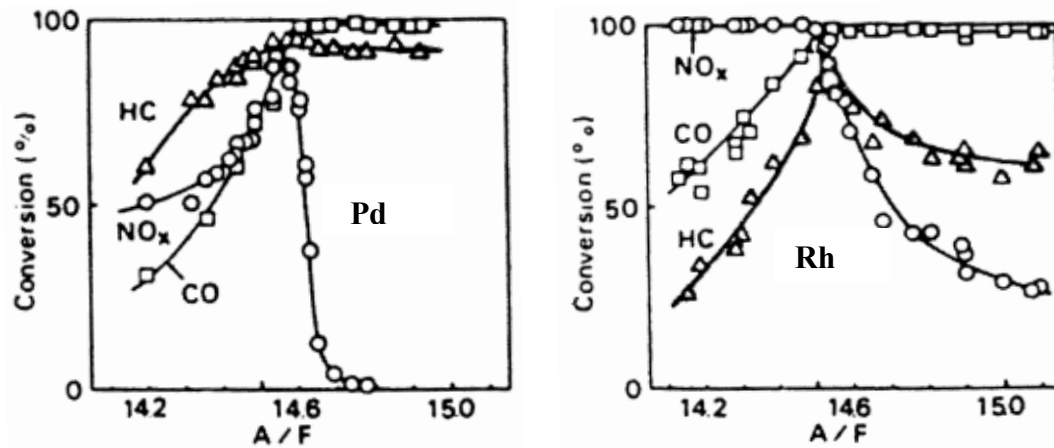
Figure 1.5: HC, CO and NO_x conversion efficiencies as a function of air-to-fuel (A/F) ratio for TWCs based on Pd (left) and Rh (right). Copied from [20].

Even though the implementation of TWCs has decreased the number of pollutants in the exhaust gas emissions of gasoline vehicles, these exhaust gases still contain undesired byproducts in the form of HC, NO_x and CO, as the TWCs are not enough efficient. In particular, during the first two minutes after the cold-start of the engine, toxic pollutants are emitted due to the low temperature in the catalyst bed. In other words, during the time period in which the temperature of the TWC is lower than the light-off temperature of around 250°C, the conversion rates of the pollutants are significantly reduced. Due to this "cold start problem", there is a strong need for catalysts that are active at low temperatures. Moreover, the selectivity of the catalyst towards a specific end-product should be considered as well, as undesired byproducts may also be formed in the low temperature regime. For instance, an important byproduct of the decomposition of NO_x at low temperatures is N_2O [24], which is one of the strongest greenhouse gases and the largest stratospheric-ozone-depleting substance [25,26]:

$$CO + 2\ NO \rightarrow N_2O + CO_2$$
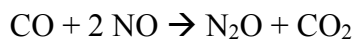
Although the adverse effects of N_2O on Earth's climate have long been known, its concentration has increased significantly in the last 150 years, as shown by Figure 1.6 [27]. Moreover, predictions made by climate models have shown that the anthropogenic N_2O emissions will almost double by 2050, and a non-negligible part of this amount will originate from mobile sources [27].
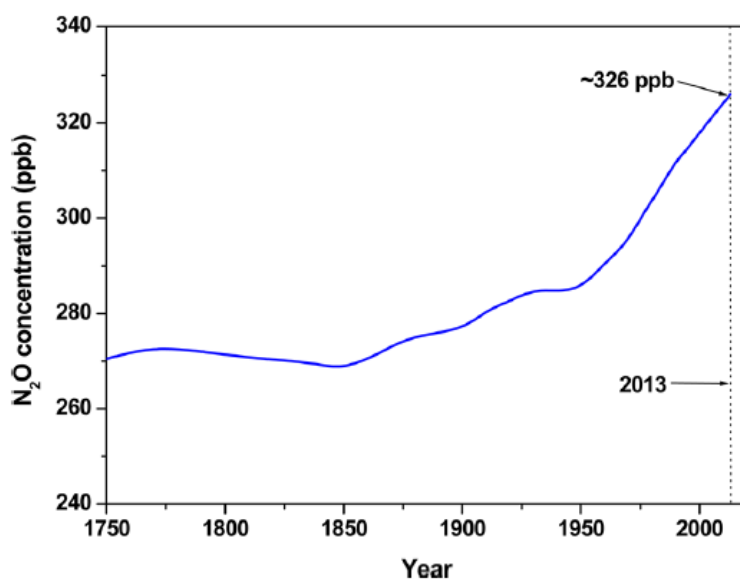
Figure 1.6: The atmospheric N_2O concentration in the period from 1750 to 2013. Copied from [27].

In order to mitigate any climate change impacts caused by harmful N_2O emissions from mobile sources, TWCs showing high selectivity towards N_2 must be developed. Even though N_2O thermally decomposes at temperatures around 200 °C, the formation of N_2O during the cold start of the engine should be prevented. The following reactions should therefore be favored:

$CO + NO \rightarrow$ ½ $N_2 + CO_2$

$CO + N_2O \rightarrow N_2 + CO_2$
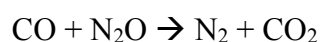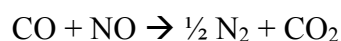
As it has been shown in the literature that oxygen vacancies can assist in the decomposition of NO_x, ceria-based systems showing high OSC are mainly preferred to counter the emission of these harmful compounds [28,29].

3. Ceria-based systems as a support

In heterogeneous catalysis, metal oxides are of paramount importance, serving as active catalysts, catalyst supports, and as promotors and modifiers [30–32]. In addition, mixed metal oxides have also found widespread use as solid catalysts due to their altered chemical, electronic and structural properties as compared to the parent oxides. This had been attributed to synergy between the different components in the mixed oxide [33–35]. In particular, heterogeneous catalysts based on transition metal oxides have attracted special interest due to their distinct chemisorption properties, related to the partially filled d-orbitals of transition metal ions [36].

Among the numerous metal oxides, cerium dioxide (CeO_2) has attracted much attention over the past decades due to its unique physicochemical properties, which make it of great interest for various industrial applications. Its high oxygen ion conductivity, for example, in combination with its high mechanical strength, allows its effective use in Solid Oxide Fuel Cells (SOFC) [37]. Furthermore, CeO_2 is often used as the active component in oxygen sensors [38,39], and its strong UV absorption and high transparency to visible light make of CeO_2 an

interesting material to use in solar applications [40]. Finally, due to its high oxygen storage capacity (OSC), CeO_2 plays an important role in heterogeneous catalysis as a support or promotor material [41].

One major drawback of CeO_2, however, is its low thermal stability: CeO_2 sinters easily at temperatures higher than 1073 K, and especially under reducing conditions [42,43]. The sintering of the metal particles at high temperatures must be prevented at any cost, as this will lead to a lower surface area of the support resulting in a lower OSC and thus negatively affecting its catalytic redox activity. To counteract the thermal deactivation of the support, solid solutions of CeO_2 with zirconia (ZrO_2) were prepared in the 1990s to increase the overall thermal stability [44]. However, due to the many different stable polymorphs in which ZrO_2 can exist, the phase diagram of the CeO_2-ZrO_2 solid solution system reveals a complex behavior in terms of phase transformations depending on the temperature and the mole percentage of ZrO_2 [45]. These different crystal phases and their characteristics have been extensively studied by Trovarelli et al. [46,47]. ZrO_2 adopts a monoclinic crystal structure at room temperature and tetragonal and cubic crystal structures at higher temperatures, while CeO_2 displays a CaF_2 fluorite structure (space group *Fm-3m*), which is shown in Figure 1.7 (left). In the fluorite structure of CeO_2, the oxygen anions are occupying the tetrahedral holes and they have a coordination number of 4, while the coordination number of Ce is 8.
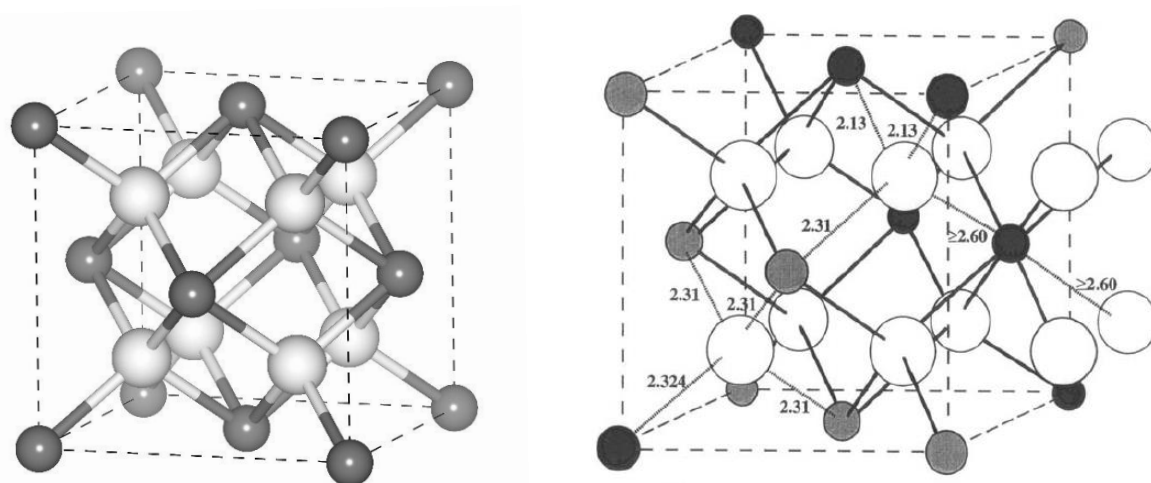
Figure 1.7: CaF_2 fluorite structure of CeO_2 (left). Doping of CeO_2 with ZrO_2 results in more labile lattice oxygen anions due to the creation of elongated Zr-O bonds, which could contribute to the increased OSC observed for $Ce_{0.5}Zr_{0.5}O_2$ (right) compared to CeO_2. Grey = Ce, white = O, black = Zr. Left figure: drawn with Vesta, right figure: copied from [46].

Doping CeO_2 with an equimolar amount of ZrO_2 leads to the crystal structure as shown in Figure 1.7 (right). This structure was evidenced by EXAFS measurements performed by Vlaic et al., who showed the existence of two different types of oxygen anions [48]. For the first type only one of the four nearest neighbor (NN) Ce^{4+} cations is substituted for a single Zr^{4+} cation, while for the second type three of the four NN Ce^{4+} cations are substituted for three Zr^{4+} cations. The oxygen anions from the second type tend to adopt a geometry similar to the one found in ZrO_2, and as a consequence these anions will move closer to two NN Zr^{4+} cations to form a

typical Zr-O bond length of 2.13 Å. Simultaneously, the bond that the oxygen anion forms with its third Zr^{4+} neighbor elongates to a nonbonding distance of 2.60 Å or higher. The formation of these elongated Zr-O bonds might explain why there are more labile oxygen anions found in $Ce_{0.5}Zr_{0.5}O_2$, which in turn leads to the improved redox properties of $Ce_{0.5}Zr_{0.5}O_2$ compared to CeO_2. In summary, the increased OSC observed for $Ce_{0.5}Zr_{0.5}O_2$ is the result of a higher reducibility of Ce^{4+} after doping with a smaller isovalent Zr^{4+} cation, leading to lattice strains and structural defects which facilitate the movement of oxygen anions through the lattice.

It has been shown in literature that ceria-zirconia solid solutions of different Ce/Zr ratio's yield different results in terms of their redox behavior. Optimal redox properties were reported for ceria-zirconia solid solutions with a composition of $Ce_{0.5}Zr_{0.5}O_2$ by Fornasiero et al. [49]. This result was confirmed by density functional theory calculations applied by Wang et al, who also found that ceria-zirconia solid solutions with a Ce/Zr ratio of one exhibits the best OSC performance [50]. Consequently, most research groups have been preparing $Ce_{0.5}Zr_{0.5}O_2$ solid solutions and they have been further optimizing them in order to meet the stringent emission regulations set by the federal environmental protection agencies.

The Ce/Zr ratio in $Ce_xZr_{1-x}O_2$ not only seems to affect the OSC, but also the thermal stability of the solid solution system. However, some contradictory results were reported in the literature regarding the content of ZrO_2 that is needed in the solid solution with CeO_2 in order to achieve the highest thermal stability. In 1997, Trovarelli et al. found that $Ce_{0.8}Zr_{0.2}O_2$ showed the highest thermal resistance as compared to other solid solution compositions [51]. In contrast, Cuif et al. observed in the same year that ZrO_2-rich compositions showed less sintering as compared to CeO_2-rich compositions [52], while $Ce_{0.5}Zr_{0.5}O_2$ compositions were found to be more thermally stable than either CeO_2-rich or ZrO_2-rich compositions by Kaspar et al. [53], who employed a citrate complexation synthesis method which allowed them to obtain homogeneous single phase products. Accordingly, it was previously reported that high phase purities are crucial for obtaining higher thermal stabilities [54]. Knowing that the pore structure of the solid solution also strongly affects its resistance to sintering [55], it can be concluded that it is difficult to establish a general rule concerning the optimal composition of $Ce_xZr_{1-x}O_2$ solid solution systems when they are synthesized with different methods and used under different reaction conditions. Another reason for this discrepancy observed in literature was given by Kaspar et al. [53], who suggested the uncontrollable formation of metastable phases at the nanoscale level with synthesis methods yielding pseudo- or non-homogeneous solid solution systems, and which are difficult to detect by the traditional characterization techniques [56]. Therefore, new synthesis methods need to be developed that can produce real homogeneous single phase materials in order to obtain reproducible results and to establish general rules concerning the effect of reaction conditions on the material's properties [53].

Various synthesis methods have been reported in the literature for preparing ceria-zirconia mixed oxides [57]. Selecting the appropriate method is of critical significance for the performance of the end-product, as the synthesis method determines its surface area, phase homogeneity and textural and morphological properties. In addition, the choice of the synthesis method is of considerable economic and environmental importance. For this reason, solid state synthesis of $Ce_xZr_{1-x}O_2$ should be abandoned not only due to the requirement of high

temperatures for firing the oxides, but also due to the low surface area of the end-product [49,58]. A second method often used for preparing solid solution systems is the co-precipitation method, which requires much lower processing temperatures than the solid state synthesis [23,59,60]. However, post-synthesis treatments (i.e., filtering and washing) makes this method not economically feasible and environmentally friendly. Moreover, a major drawback experienced with the co-precipitation method is the necessity to fully control various synthesis parameters in order to achieve high homogeneity of the end-product, hampering the reproducibility of this method. In contrast, high homogeneity can be more easily achieved with the sol-gel method, which is one of the most used wet-chemical techniques for synthesizing metal oxides [61,62]. This one-pot synthesis method allows facile formation of high purity metal oxides with uniform and small particle sizes via low-cost, low-temperature processing. Consequently, the sol-gel method is considered to be more industrially relevant than the previously mentioned synthesis methods. The high versatility of this synthesis route also ensures control of the textural and morphological properties and the composition of the end-product, hence explaining why this method has become widely popular for the synthesis of heterogeneous catalysts.

Besides doping CeO_2 with ZrO_2 to increase the thermal stability of the support, multiple transition metals such as Cu [63,64], Co [65], Ni [66] and Fe [67] have also been used as a dopant to alter the catalytic redox properties of the system. It has been shown that doping CeO_2 with transition metals increases the number of oxygen vacancies [5], which are believed to play an important role in the reduction of NO_x to N_2 [24,28,68]. Besides the creation of more oxygen vacancies, another reason for the improved catalytic activity is the presence of a synergistic effect between the reducible CeO_2 and the transition metal. For example, the exceptional high activity for NO_x reduction observed for Cu/CeO_2 systems is primarily attributed to the presence of both Cu^{2+}/Cu^+ and Ce^{4+}/Ce^{3+} redox couples, allowing active Cu^+ sites to regenerate, after having adsorbed NO or N_2O, by the subsequent reaction with Ce^{3+} sites [69]. The availability of these Ce^{3+} sites is related to the amount of oxygen vacancies in the support, and therefore more reduced CeO_2-based supports typically exhibit superior redox properties due to the improved synergistic interaction between the metal and the support. Finally, these dopant effects could lead to significant changes in the catalytic activity towards various applications such as preferential oxidation of CO [70], oxidation of hydrocarbons [18], steam reforming [71], VOCs oxidation [72,73] and the water-gas shift (WGS) reaction [17].

4. The problem of metal particle sintering

In order to meet the increasingly stringent emission standards, high conversion rates of the exhaust gas pollutants at low temperatures must be achieved. Solving the cold-start problem therefore involves the development of catalysts that are not only highly active at low temperatures, but also show high selectivity for a specific end-product. The alternative and more direct solution implemented by the automotive industry is to make use of close-coupled catalysts. These type of catalysts are mounted close to the engine exhaust manifold where it is exposed to temperatures as high as 1273-1373 K, allowing it to reach the light-off temperature much faster to limit the prolonged emission of the pollutants in the first seconds after the cold-start of the engine [74,75]. This simple and effective measure, however, involves a new problem related to the undesired thermal deactivation of the catalyst. Being exposed to higher operating temperatures means more facile sintering of the metal phase, resulting in a decrease in specific surface area and catalytic activity. Moreover, a lower selectivity to the desired end-products can be expected as well. Consequently, this thermal deactivation limits the long-term use of TWCs, bringing adverse effects on the economy and environment [76]. Therefore, new catalyst systems showing high thermal stability need to be developed to overcome the problem of thermal deactivation.

To successfully develop catalyst systems that are thermally stable at high temperatures, a proper understanding of the origin of thermal deactivation is required. The two main mechanisms that form the basis of thermal deactivation are the solid-state reaction and sintering. The first mechanism typically affects the active phase of the catalytic converter, which is transformed to a non-active phase at high temperatures. PdO species, for example, which are believed to be the active phase for full oxidation of hydrocarbons [77], are decomposed into non-active Pd at temperatures around 800 °C [78,79]. The second mechanism, which is also called coarsening or thermal aging, involves the sintering of the catalyst leading to a loss of metal or support surface area and/or pore collapse. Collapse of the material or immense sintering is often the result of a phase transformation taking place at high temperatures, by which the newly formed phase typically exhibits a lower surface area. For example, γ-alumina transforms to the sintered, densified α-phase (with lower surface area) at temperatures higher than 1000°C. Consequently, the sintering of the support material can result in a decreased OSC and in the encapsulation of the supported noble metal leading to deactivation of the TWC [80]. Whether encapsulation of the noble metal occurs, however, depends on numerous variables such as the synthesis method, reaction conditions and the support material. For example, Graham et al. observed encapsulation of supported Rh and Pd in the pores of ceria-zirconia support after high temperature aging under redox conditions, while no encapsulation was observed for Pt supported on ceria-zirconia [81].

The driving force for metal particle sintering is a decrease in surface energy when larger particles are formed, and the extent to which sintering occurs depends on various parameters such as the applied synthesis method, the choice of the support and metal, the presence of a promotor, the gas environment and, of course, the temperature. It is believed that the sintering can occur either via Ostwald ripening or via particle migration [82,83].
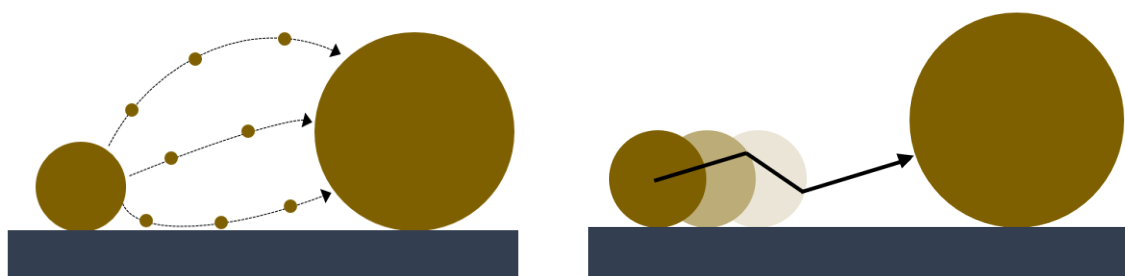
Figure 1.8: Illustration of the two different sintering phenomena that can occur for supported metal nanoparticles. In the left figure, the sintering occurs via the Ostwald ripening mechanism (atomic migration), while in the right figure sintering via the particle migration mechanism is depicted.

In the Ostwald ripening mechanism, which is also called atomic migration, atoms from small particles migrate to larger particles via diffusion, as shown in Figure 1.8 (left). This migration of atoms either takes place on the surface of the support or via the vapor phase. Conversely, in the particle migration mechanism shown in Figure 1.8 (right), not atoms but entire particles migrate over the support's surface until they eventually collide and coalesce with other particles in their path.

5. Preparation and stabilization of single-atom catalysts

Before the actual synthesis of the heterogeneous catalyst, important decisions have to be made that can significantly influence its final properties, including its catalytic activity and thermal stability. The choice of the metal oxide support, for example, plays an important role in preventing the sintering of the supported active metal phase. On a reducible support such as CeO_2 or TiO_2, metals can be stabilized in the form of single sites due to a strong electronic interaction between the metal and the reducible support. This 'strong metal-support interaction' was first reported by Tauster in 1978, and it explains why CeO_2 can disperse metals on its surface so efficiently [84]. Metal-support interactions also explain the increased catalytic activity that is observed when CeO_2 is added to ceramic supports of alumina (Al_2O_3) [20,85]: the high dispersion of supported noble metals on CeO_2 allows almost full use of the noble metal loading, and the associated decrease in particle size leads to a higher surface area and more surface noble metal atoms that can participate in the catalytic reactions.

The generation of single metal sites on the surface of a reducible support has finally led to the introduction of the term 'single atom catalysts' (SACs). These single atoms often function as active sites for many catalytic reactions, and they have already proven to be highly reactive for the oxidation of CO [86,87], the water-gas shift reaction [88], hydroformylation of olefins [89,90], hydrogenation reactions [91,92] and photo- and electrocatalytic hydrogen evolution reactions [93,94]. Consequently, multiple synthesis methods have been developed which aim to generate atomically dispersed metal species on the support's surface. Wet chemistry methods, for example, have been extensively used since the early days of heterogeneous catalyst preparation, and researchers often employ these methods to obtain single atom catalysts because of their simplicity, high versatility and often low process temperatures. Wet

impregnation, for example, involves pouring a metal salt solution over the support in excess of its pore volume, leading to the deposition of the metal on the support after mixing and evaporating the dispersion medium. With this method, atomically dispersed supported metal catalysts can be produced when one opts for a support that is reducible such as CeO_2 or TiO_2 [86,95].

It should be noted that at elevated temperatures isolated noble metal atoms supported on a reducible metal oxide might still sinter via surface diffusion to form crystals with reduced catalytic activity. Their sintering is favored because single metal atoms typically exhibit higher surface energies than metal nanoparticles and clusters. In addition, atoms are generally more mobile than nanoparticles and clusters, especially at elevated temperatures where their sintering becomes more favored. Therefore, a strong metal-support interaction is crucial in order to obtain stabilized single metal centers supported on a surface [96]. In line with this, it has been extensively reported in literature that by supporting the active phase on a reducible metal oxide, anchoring and stabilization effects can be achieved that can suppress the sintering of the supported metal to a certain extent. These results are consistent with the original study conducted by Tauster on strong metal-support interactions [84]. For example, in 2006, Nagai et al. reported the formation of stable Pt-O-Ce bonds in an oxidizing environment, and it was shown that these bonds can act as anchors to suppress sintering of the noble metal [9]. The same conclusion was reached by Shinjoh et al. in 2009 [8], and more recent studies also indicate the formation of similar bonds between CeO_2 and Pt [15,16]. Farmer et al. explained the high stability achieved with CeO_2 using calorimetric measurements, showing that the adhesion energy of Ag on CeO_2 is intrinsically higher compared to Ag supported on the non-reducible MgO support [97]. The large difference in adhesion energies was explained by the presence of both defects and (111) terraces for CeO_2, which are able to form strong bonds with metal atoms. The high amount of oxygen vacancies present in CeO_2 was also given as a partial explanation for the high sintering resistance of transition metals supported on CeO_2, as it was shown that vacancies can also act as trapping sites for the supported metal [98]. Conclusively, electronic defects associated with unsaturated sites and vacancies on the support's surface might play an important role in the resistance to sintering, as these defects can act as anchoring sites that can strongly bind metal atoms or particles.

In addition to electronic defects, functional groups on the support's surface were also shown to partially suppress the sintering of supported metal atoms or particles. For example, the modification of the surface of a rutile TiO_2 support with hydroxyl groups was shown to decrease the mobility of supported palladium atoms [99]. This was explained by Density Functional Theory (DFT) calculations which clearly showed that surface diffusion barriers for Pd atoms on hydroxylated surfaces are higher than on hydroxyl-free surfaces. However, in the end Pd clusters were also observed on the hydroxylated surfaces, even at room temperature and low noble metal loading.

Despite ample evidence demonstrating that supported noble metal atoms can be stabilized by reducible metal oxides, the observed metal-support interaction is often not strong enough to prevent sintering of the active phase. Consequently, multi-step synthesis techniques in which the noble metal is deposited on the support in a later step might suffer significantly from sintering phenomena. This conclusion indicates the significance of solid solution catalyst systems, in which the noble metals are present in the form of ions separated by O^{2-} ions of the reducible support. By substituting some of the Ce^{4+} ions in the lattice of CeO_2, the noble metal

ions are kept apart by the oxygen bonds, reducing their sintering in high temperature operating conditions. Furthermore, CeO_2 appears to be a suitable support for solid solution systems because of its Ce^{4+}/Ce^{3+} redox couple. This allows for instance Pd to cycle between its oxidation states Pd^{2+} and Pd^0, while its high dispersion in the support is maintained and no bulk Pd metal particles are being formed [100]. Examples of synthesis methods that can produce solid solution systems are co-precipitation, deposition-precipitation, sol-gel and flame-spray pyrolysis synthesis [57].

One can argue, that the drawback of the solid solution systems is that the majority of the noble metal loading is buried in the bulk of the support, leading to a significant loss of noble metal atoms available on the surface for catalyzing the intended reactions. Consequently, alternative synthesis methods have been proposed that allow full use of the noble metal loading by transferring or depositing the noble metal on the support's surface, avoiding the formation of bulky noble metal crystallites after aging at high temperatures that are observed for wet impregnated supports. A recent technique proposed is so called "atom trapping". It involves the transfer of noble metal atoms from one oxide to another oxide, with the latter having a higher affinity for the noble metal. This transfer phenomenon, shown in Figure 1.9, was observed for platinum supported on Al_2O_3 after aging in air at 800 °C [16]. After the high temperature treatment, individual platinum atoms were transferred to ceria and trapped on its surface in the form of single atoms. The efficiency and the extent of trapping the platinum atoms depended on the morphology of ceria: ceria nanorods and polyhedral ceria were more efficient than ceria nanocubes in trapping of the noble metal atoms. This observation was explained by the more defective nature of the ceria nanorods and polyhedral ceria which expose (111) facets compared with ceria cubes dominated by the (100) surfaces. These surface defects play a key role in the trapping mechanism, as they are typically characterized by coordinately unsaturated sites which can strongly bind the supported metal atoms.
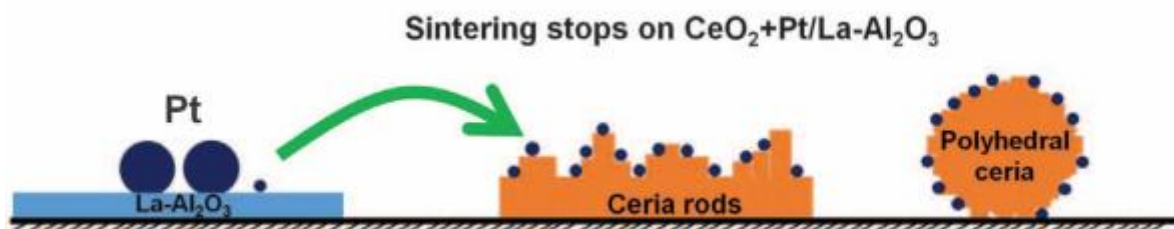
Figure 1.9: Simplified scheme of the atom trapping mechanism. After thermally aging at 800 °C, it was observed that platinum atoms were transferred from Al_2O_3 to CeO_2, resulting in the 'trapping' of the noble metal on the surface defects of the reducible support in the form of single atoms. Copied from [16].

A major benefit of atom trapping is that single atom sites can be obtained in high temperature regions, where normally Ostwald ripening or particle migration phenomena are observed. However, this method is largely dependent on the amount of defects present on the surface of ceria. Thus, applications where high noble metal loadings are preferred cannot rely on atom trapping, since the amount of noble metal atoms that can be trapped and stabilized by the defects is limited by the concentration of such anchoring sites. In addition, the amount of surface

defects exposed by each morphology ceria support can vary significantly, rendering this technique not fully reproducible if the certain loading must be kept.

Physical synthesis methods such as atomic layer deposition (ALD) have also been proposed, and they have proven to be powerful techniques for obtaining single metal sites on a support's surface [101]. The requirement of high vacuum conditions and specialized equipment makes ALD, however, expensive and not very practical. Moreover, similar to the case of atom trapping, only low noble metal loadings can be deposited on the support's surface with this technique [102].

Finally, the above examples illustrate that the metal loading can be an important factor in preventing metal sintering. Catalyst systems with high metal loadings carry an increased risk for sintering simply due to the decreased distance between each individual noble metal atom, favoring the formation of nanoparticles or clusters. Combination of different synthesis methods and noble metals yield different optimal metal loadings up to which no metallic or oxide species are observed. For example, Li et al. showed the absence of Pd metal in impregnated mesoporous Pd/CeO_2 up to 2.5 wt.% metal loading [103]. In solution combustion synthesized $Pt-CeO_2$, no Pt metal or oxide was found for a metal loading of 2 at.% as demonstrated by Bisht et al. [104], while for sol-gel synthesized $Pd-CeO_2$ no Pd metal or oxide was present for a metal loading of 1 at.% as shown by Wang et al. [105].

Chapter 2

Synthesis of thermally stable ceria-zirconia solid solution systems via a polymer-assisted sol-gel method

1. Introduction

In the sol-gel method, various synthesis parameters must be controlled that can lead to end-products showing different textural and structural properties. As a result, ceria-zirconia solid solution systems have been prepared with multiple sol-gel routes for a wide range of applications [63,106–109]. Independent of the synthesis method applied, the homogeneity of the solid solution was often found to be a key factor for the final performance of the product in a specific application. In addition, a high homogeneity appears to be crucial in preventing the segregation of the different metal components in the solid solution system [53,110,111].

Besides considering variables such as the temperature, pH, gelation time, amount of water for the hydrolysis and solvent removal, the choice of the precursor is considered as an important parameter for obtaining well-defined solid solution type systems of high homogeneity. For example, most reported sol-gel syntheses make use of metal alkoxide precursors, despite their high sensitivity to heat, moisture and long-term storage. Furthermore, different alkoxide precursors often show different hydrolysis susceptibilities leading to reduced homogeneity of the final metal oxide, which can eventually result in phase segregation [112]. Most of the alkoxide precursors are also toxic, difficult to synthesize and generally expensive. These problems can be solved by using metal salts as the precursors. However, as shown by Rossignol et al. , replacing only one of the two alkoxide precursors might not be sufficient for preparing $Ce_xZr_{1-x}O_2$ with high homogeneity [113]. In contrast, better results were obtained when non-alkoxide sol-gel routes were used [114].

Besides selecting the appropriate metal precursors, the relative rates of hydrolysis and condensation also appear to be crucial for obtaining homogenous solid solution systems [115]. For example, acid or base catalysts are often added to the solution to either promote condensation or hydrolysis, respectively, leading to different gel structures. Furthermore, these catalysts are typically added to increase the rate of the neutral reaction of some metal precursors. In particular, the reaction is slow when the partial charge on the metal is low due to a low electronegativity difference between the metal and the counterion of the precursor. The sol-gel chemistry of silica, for example, is commonly driven by these catalysts. In contrast, zirconium has a much higher partial positive charge than silicon, and as a consequence the rate of hydrolysis might be too high resulting in the formation of ill-defined zirconium-oxo/hydroxo precipitates. Control of the water content in the solution is therefore critical to adjust the hydrolysis rate, while changing the pH of the solution by adding acid or base catalysts is not sufficient anymore for highly reactive metals such as zirconium. For this reason, non-aqueous solvents are typically used. Additionally, chelating agents are often employed, as these can form

strong interactions with the metal ions to prevent excessive hydrolysis and to form a homogeneous gel [115]. The formation of an organic matrix by the chelating agent also provides evenly dispersed nucleation sites which will lead to the growth of small crystallites. Further, the presence of the organic matrix results in the mixing of the different metal components on the atomic scale, which is a key requisite for obtaining homogeneous materials.

Based on the abovementioned results reported in the literature, a sol-gel method was employed that could lead to the formation of highly stable and homogeneous ceria-zirconia solid solution systems. By using inorganic salts as the metal precursors, a non-aqueous solvent and an organic polymer as the chelating agent, a wide variety of transition metal-doped ceria-zirconia solid solutions could be successfully synthesized. The thermal stability and textural and structural properties of these solid solutions were investigated by XRD, TEM, XPS, BET, UV-Vis, H_2-TPR and EXAFS.

2. Experimental

2.1 Materials and synthesis

Ceria-zirconia support catalysts ($Ce_{0.5}Zr_{0.5}O_2$ or $CeZrO_4$) were synthesized via a polymer-assisted sol-gel method. $Ce(NO_3)_3.6H_2O$ (Alfa Aesar, 99.99%) and $ZrOCl_2.8H_2O$ (Alfa Aesar, 99.9% and Sigma Aldrich, 98%) were used as starting materials, while absolute ethanol (Biosolve, min. 99.9%) was used as the solvent. Poly(ethylene glycol)-block-poly(propylene glycol)-block-poly(ethylene glycol) with an average molecular weight of ~5800 (PEG-PPG-PEG 5800, Sigma-Aldrich) was used as a chelating agent. Ethanol solution (15 ml) of $Ce(NO_3)_3.6H_2O$ (1.736 g), $ZrOCl_2.8H_2O$ (1.288 g) and PEG-PPG-PEG 4400 (0.8 g) was prepared and stirred for approximately 2 h at room temperature until a transparent precursor sol was obtained. Next, the sol was aged at 40 °C for approximately 3 days in an oven with a beaker of water placed inside in order to keep sufficient partial pressure of water vapors. Once the rubber-like texture of gel has been employed, subsequent drying overnight at 110 °C in air was performed. After drying, the precipitate was crushed into a fine powder and calcined in air at 500 °C with a heating rate of 1 °C/min and a dwelling time of 4 hours. A schematic overview of the synthesis procedure is shown in Figure 2.1.
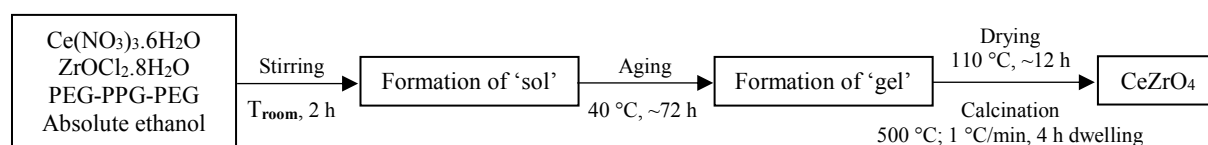

Figure 2.1: Flowchart for the preparation of $CeZrO_4$ via a polymer assisted sol-gel method.

Doped ceria-zirconia catalysts were also prepared using different transition metals with various metal loadings. The same synthesis procedure as for the bare $Ce_{0.5}Zr_{0.5}O_2$ was adopted, simply adding transition metal precursors in the first step of the synthesis procedure. The aging time

varied from 3 to 5 days, depending on the dopant and the loading chosen. All of the samples were calcined at 500 and 800 °C to investigate their thermal stability, while a temperature of 900 °C was also once used. Transition metals such as Cu, Fe, Co, Cr, Ni and Pd were chosen as dopants. Following precursors of abovementioned metals were used: $Cu(NO_3)_2.3H_2O$ (Sigma Aldrich, 99-104%), $Fe(NO_3)_3.9H_2O$ (Sigma Aldrich, $\geq$ 98%), $Co(NO_3)_2.6H_2O$ (Emsure, $\geq$ 99%), $Cr(NO_3)_3.9H_2O$ (Alfa Aesar, 98.5%), $Ni(NO_3)_2.6H_2O$ (Sigma Aldrich, $\geq$ 97%) and $Pd(acac)_2$ (acac = acetylacetonate, Sigma Aldrich, 99%). The metal loadings were kept as 2.77, 5.55 and 11.11 mol%, while for palladium 1 and 5 wt.% were used. The obtained catalysts were labeled as xMCZ, with x taking values of 1, 2, 5 and 11, standing for metal loadings of respectively 1 wt.%, 2.77 mol%, 5.55 mol% or 5 wt.% (in case of Pd) and 11.11 mol%., M reflecting the dopant used, and CZ referring to ceria-zirconia. For example, a sample doped with 2.77 mol% Fe is denoted as 2FeCZ.

Palladium (1 wt.%) was deposited on both bare and doped ceria-zirconia supports via a conventional wet impregnation method. $Pd(NO_3)_2.2H_2O$ (Sigma Aldrich, 40% Pd basis) was dissolved with demineralized water in a small snap cap vial and the solution was subsequently poured onto the support. After vigorously stirring the dispersion for approximately 30 min, the mixture was heated to 80 °C to slowly evaporate the water while stirring. The resulting solid was dried at 110 °C and crushed to a fine powder, which was finally calcined in air at 300 °C with a heating rate of 5 °C/min and a dwelling time of 3 h. The bare ceria-zirconia support impregnated with 1 wt.% Pd was denoted as 1Pd/CZ.

2.2 Catalyst characterization

X-ray diffraction (XRD)

In this work, X-ray diffraction (XRD) was used to analyze the crystal structure and thermal stability of the ceria-zirconia mixed oxides. A Bruker D2 Phaser powder diffraction system equipped with a copper anode and a thin nickel foil filter was used. The latter removes the Kβ radiation of the copper X-ray source, allowing the Cu Kα radiation (λ = 1.5406 Å) to pass. The XRD patterns were recorded in a 2θ range of 20° to 80° with a step size of 0.02° and a time per step of 0.5s. Samples calcined at 800 °C and 900 °C were recorded with 1s per step. A 0.6 mm divergence slit was used to limit the beam divergence of the source, while an anti-scatter screen with a sample-screen distance of 0.5 mm was used to block scattered radiation at low angles. The samples were rotated with a constant speed of 30 rot/min during the XRD measurements.

Transmission electron microscopy (TEM)

TEM measurements were performed on a FEI Tecnai 20 transmission electron microscope with an electron acceleration voltage of 200 kV and a LaB_6 filament. A few milligrams of each sample were sonicated in pure ethanol (Biosolve, Extra dry, 99.9%), and a few drops of the resulting dispersion were dripped over a 200 mesh Cu TEM grid with a holey carbon support film. Prior to imaging, the supported samples were left in an oven at 40 °C overnight to remove residual ethanol.

N$_2$ physisorption

The surface area of the ceria-zirconia mixed oxides was determined via N$_2$ physisorption measurements at -196 °C on a Micromeritics Tristar II 3020 instrument. Approximately 150 mg of the sample was transferred in a glass sample tube, followed by pretreatment overnight at 150 °C under a continuous N$_2$ flow to remove moisture and impurities. The Brunauer-Emmet-Teller (BET) model was applied for determining the surface area from the adsorption isotherms obtained by computer controlled gravimetric analysis.

UV-Vis spectroscopy

The metal oxide speciation and thermal stability was also studied by UV-Visible (UV-Vis) spectroscopy. The measurements were performed on a Shimadzu UV-2401PC UV-Vis spectrometer. BaSO$_4$ (first grade, Wako Chemicals) was used as a reference. The UV-Vis spectra were measured in absorbance mode in the 190-800 nm range with 0.5 nm steps. The spectra of the transition metal-doped samples were compared with those of the corresponding parent oxides, which were Fe$_2$O$_3$ (Alfa Aesar, $\geq$ 99.99%), CuO (Alfa Aesar, $\geq$ 99.99%), Co$_2$O$_3$ (Alfa Aesar, 99.7%), Cr$_2$O$_3$ (Sigma Aldrich, $\geq$ 98%) and PdO (Sigma Aldrich, 99.97%). The spectra of the Ni-doped samples were compared with the spectrum of NiO found in the literature.

X-ray photoelectron spectroscopy (XPS)

XPS measurements were carried out with a Thermo Scientific K-Alpha, equipped with a monochromatic small-spot X-ray source and a 180° double focusing hemispherical analyzer with a 128-channel detector. Spectra were obtained using an aluminium anode (Al Kα = 1486.6 eV) operating at 72W and a spot size of 400 m. Survey scans were measured at a constant pass energy of 200 eV and region scans at 50 eV. The background pressure was 2×10^{-8} mbar and during measurement 4×10^{-7} mbar Argon because of charge compensation by the dual-beam low energy electron / Arion source. Data analysis was performed using CasaXPS software. The binding energy was corrected for surface charging by taking the Ce3d$_{3/2}$ peak as a reference at 916.7 eV.

Hydrogen-Temperature Programmed Reduction (H$_2$-TPR)

The reducibility of the catalysts was determined by hydrogen-temperature programmed reduction (H$_2$-TPR) using a Micromeritics AutoChem II 2920 equipped with a computer-controlled oven and a thermal conductivity detector (TCD). Approximately 100 mg of each sample were transferred into a U-shaped quartz reactor tube and fixed between two quartz wool plugs. Before the H$_2$-TPR experiment was carried out, the samples were first pretreated *in situ* to remove moisture and impurities. The pretreatment involved calcining the samples in a 50 ml/min 5% O$_2$/He flow at 300 °C using a heating rate of 10 °C/min, after which they were subsequently cooled to room temperature at a cooling rate of 35 °C/min.

The H$_2$-TPR experiment is carried out by using a H$_2$ flow, and the reduction process of the oxidized species occurs under temperature programmed conditions by increasing the temperature with a constant heating rate. For reduction of the samples, a 50 ml/min flow of 4%

H_2/N_2 was used and the temperature was ramped to 600-800 °C at a rate of 10 °C/min. The TCD signal was normalized by the weight of the sample.

Extended X-ray absorption fine structure (EXAFS) spectroscopy

X-ray absorption spectroscopy experiments were performed at the DUBBLE beamline at ESRF Grenoble, France (Co and Fe), and at the beamline B18 at the Diamond Light Source, Rutherford Appleton laboratories, Oxford, UK (Pd and Cu). The data were collected in transmission mode (Pd and Cu) and in fluorescence mode (Co and Fe). Further, the data were collected at the Pd K-edge (24.4 keV), Cu K-edge (8.99 keV), Co K-edge (7.71 keV) and Fe K-edge (7.11 keV) at room temperature and atmospheric pressure. Foils of the corresponding metals were used for the energy calibration.

All the samples, except of the ones measured at Pd K-edge, were diluted with BN and pelletized as self-supporting discs. Proper dilution was estimated via the XAFSmass software to compromise the step-edge value and the absorption. Background subtraction was performed with the Athena software of the Demeter package [116].

3. Results and discussion

3.1 Textural and structural properties

The thermal stability of transition metal-doped ceria-zirconia solid solution systems was investigated by XRD. Figure 2.2 shows the diffraction patterns of pure ceria-zirconia and ceria-zirconia doped with different loadings of Fe calcined at 500 °C and 800 °C.
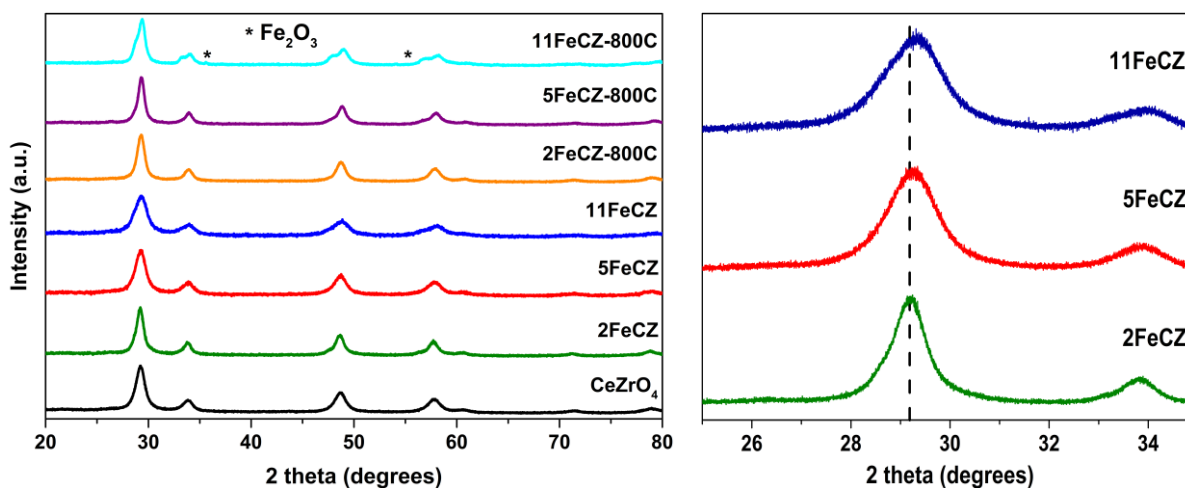
Figure 2.2: XRD patterns (left) of the Fe-doped samples calcined at 500 and 800 °C. The shift of the diffraction peaks to higher angles (right) implies that Fe is incorporated in the $CeZrO_4$ lattice and that a solid solution is formed.

The reflections as seen in the diffraction pattern of pure CZ (67 m^2/g) look similar to those of the cubic fluorite structure of CeO_2 (*Fm-3m* space group). The slight shift of the CZ reflection

peaks to higher diffraction angles can be explained by the substitution of Ce^{4+} cations (0.97 Å) with smaller Zr^{4+} cations (0.84 Å), leading to a contraction of the CeO_2 lattice [117]. This observation indicates the formation of a stable solid solution upon the introduction of Zr^{4+} in the CeO_2 lattice. Furthermore, according to Vegard's law, the dopant solubility of Zr in the CeO_2 lattice should be relatively high because of the similar cationic radii of Zr^{4+} and Ce^{4+} [118].

Doping of ceria-zirconia with different concentrations of Fe did not lead to the appearance of new reflection peaks in the XRD pattern after the calcination at 500 °C. Thus it can be concluded that Fe is incorporated into the crystal lattice or, amorphous, and very finely dispersed. However, the shift of the reflection peaks to higher angles upon higher Fe loadings, as can be clearly seen in Figure 2.2, strongly suggests the incorporation of a significant amount of Fe in the lattice and the formation of a solid solution [119]. Although it must be noted that the presence of small iron clusters on the surface of CZ cannot be solely ruled out by means of the XRD results. Just as in the case of doping CeO_2 with Zr, the smaller radius of Fe^{3+} (0.64 Å) compared to that of Ce^{4+} (0.97 Å) results in a decrease of the size of the unit cell and in a shift of the reflection peaks to higher angles, which is in agreement with the abovementioned Vegard's law. Furthermore, a broadening of the reflection peaks with increasing Fe content was also observed, suggesting that the crystallite size decreased upon the doping [120,121]. The explanation for this peak broadening might be the formation of lattice distortions such as point defects or dislocations when doping with a higher amount of Fe. Consequently, the presence of these defects might limit the growth of the crystallites formed during the calcination process, resulting in a smaller crystallite size. In addition, these defects can cause strain in the lattice leading to changes in the interplanar lattice spacing, which in turn could affect the diffraction angle of the incident X-rays and hence also the position of the reflection peaks.

After calcining the samples at 800 °C the peak widths decreased, suggesting that the crystallite size increased due to the sintering of the CZ support at elevated temperatures. The particle sizes, shown in Table 2.1, were determined from XRD by using the Scherrer equation. It was concluded from the table that a smaller particle size is not necessarily associated with a larger BET surface area, and several reasons could be given for this observation. Small metal dopant ions like Fe^{3+} tend to occupy and block the pores in a material, leading to less surface area exposed that can be measured by the physisorption techniques. However, as evidenced by the TEM images, the sol-gel method used in this study does not result in the formation of a highly porous material, and therefore there should be another reason for this observation. As the BET model is based on single site adsorption, the inhomogeneous surface of the support that might have been formed after the doping could lead to deviations in the physisorption measurements. This effect is more pronounced for higher dopant concentrations, and this could potentially explain the small specific surface area measured for 11FeCZ.

Table 2.1: Surface area and particle size determined by N_2 physisorption and the Scherrer equation for pure ceria-zirconia and Fe-doped ceria-zirconia.

Sample	BET surface area (m²/g)	Particle size Scherrer (nm)
CeZrO₄	67	8.0
2FeCZ	48	8.9
5FeCZ	60	7.2
11FeCZ	43	5.7

To investigate the thermal stability of Fe-doped CZ, the sample with the highest Fe dopant concentration (11FeCZ) was first calcined at a temperature of 800 °C. The partial splitting of the reflection peaks of 11FeCZ-800C indicates phase separation taking place, with the left and right shoulder corresponding to a CeO_2-rich and a ZrO_2-rich phase, respectively. Additionally, hematite (Fe_2O_3) reflection peaks in 11FeCZ-800C were also observed next to the CZ reflections. Conclusively, 11FeCZ was not found to be stable when calcined at 800 °C, most likely due to the Fe loading that appeared to be too high to preserve the structure of the solid solution and to prevent the crystal lattice from disintegrating at high temperatures. Subsequently, it was examined whether 5FeCZ would be stable at 800 °C, and the XRD pattern of 5FeCZ-800C evidenced that no phase separation or formation of iron oxide took place. It should be noted, however, that hematite or magnetite (Fe_3O_4) might be in the form of amorphous oxides or that the amount is too small to be detected by the XRD instrument. Nevertheless, it was concluded that xFeCZ showed high thermal stability up to a molar loading of at least 5.55 mol% Fe.
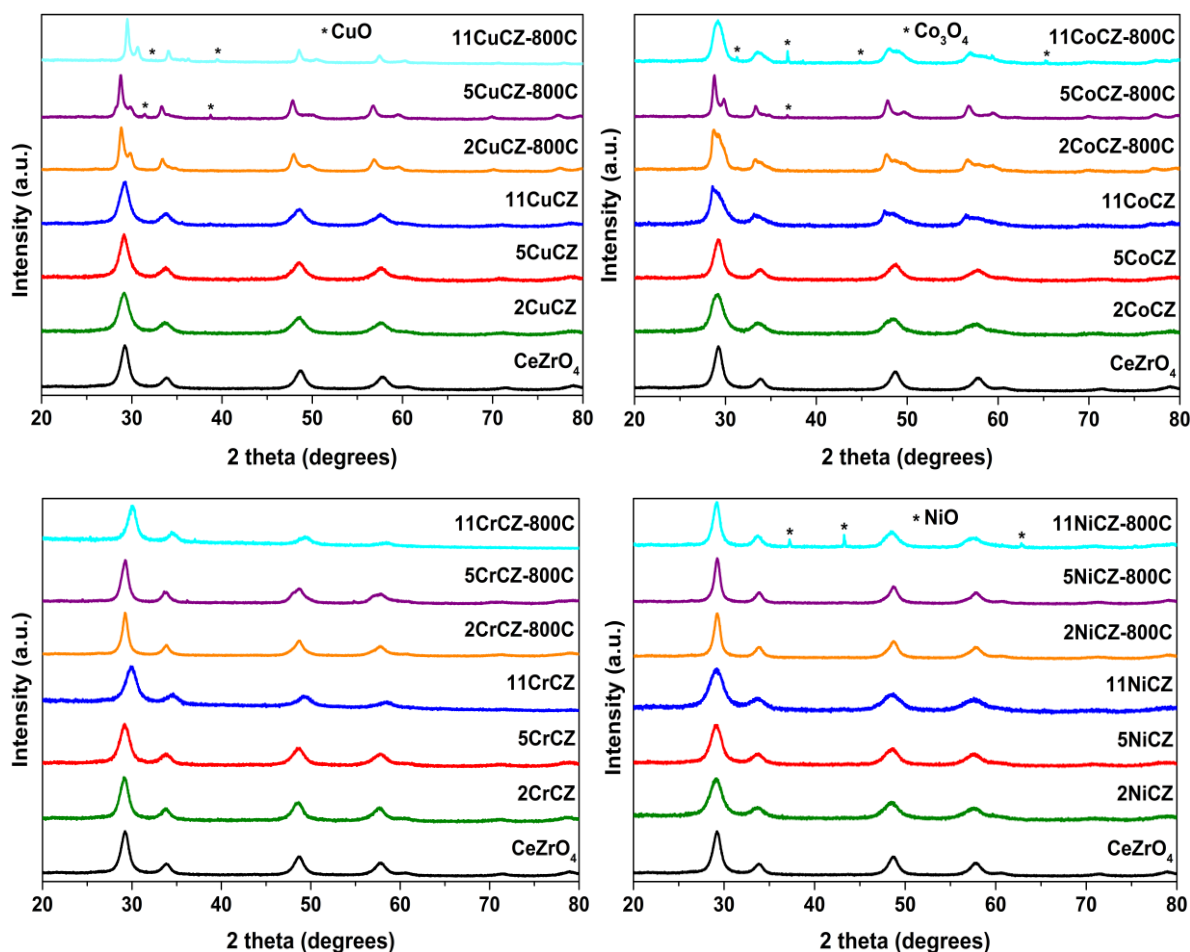
Figure 2.3: XRD patterns of Cu-, Co-, Cr- and Ni-doped ceria-zirconia samples calcined at 500 and 800 °C.

Similar trends were found for CZ doped with Cu, Co, Ni and Cr, as shown in Figure 2.3. Upon increasing the metal loading, a shift of the reflection peaks towards higher diffraction angles was observed for all dopants, which corresponds to a contraction of the fluorite lattice of CeO_2. This shift was attributed to the smaller ionic radii of Cu^{2+}, Co^{2+}, Ni^{2+} and Cr^{3+} compared to that of Ce^{4+} (0.97 Å), and it implies the inclusion of the abovementioned transition metals in the CeO_2 lattice resulting in the formation of solid solution type systems. For some doped systems (e.g. xNiCZ and xCrCZ) the shift to higher angles is more pronounced than for others (e.g. xCuCZ). This is due to the fact that a peak shift to higher or lower angles is not solely related to the ionic radius of the dopant. In particular, oxygen vacancies might be formed by charge compensation effects after doping with a lower valence ion and/or due to strain induced in the CeO_2 lattice by the inclusion of a smaller ion [122,123]. Therefore, as the amount of structural defects increases with the dopant concentration, the amount of Ce^{3+} in the lattice also increases. Since the radius of Ce^{3+} (1.143 Å) is larger than that of Ce^{4+} (0.97 Å), an increase in the lattice parameter can be expected that can compensate lattice contraction after doping with a smaller ion. As a result, the peak shift to higher angles after doping might be lower than initially expected. In addition, the synthesis procedure might also determine the extent to which crystal lattice changes are observed by XRD. For example, a net change in the peak positions was reported by Pino et al. after doping CeO_2 with Ni^{2+} ions, using a combustion synthesis method

[124]. Barrio et al., however, did not observe a change in the peak positions for the same doped CeO_2 system, but now prepared via a reverse microemulsion method [125]. This observation was finally explained by the formation of a large amount of oxygen vacancies that can compensate the lattice contraction upon doping with a smaller ion.

Another reason for the small shift observed for the Cu doped samples might be due to segregation of the dopant ions to the surface upon increasing the dopant loading. Several research groups have reported surface enrichment by Cu^{2+} ions occurring for Cu doped CeO_2 [126,127]. Either no change or a decrease in the lattice parameter was observed, even for CeO_2 systems doped with the same Cu loading [128–130]. These observations once again lead to the conclusion that the synthesis method applied strongly affects the extent to which surface enrichment of the dopant ions occurs. Finally, copper might also occupy interstitial sites in the lattice, causing lattice expansion which can partially neutralize lattice contraction. Interstitial site occupation is particularly important for small dopants like Cu^{2+} and Fe^{3+}. Indeed, several research groups observed only a limited shift for Fe doped CeO_2, and this was explained by the interstitial site occupation by some of the Fe ions in CeO_2 [131,132].

Similar to Fe-doped CZ, peak broadening was observed for all other transition metals upon increasing the loading. For some transition metals (Fe, Cr, Ni) the broadening was more pronounced than for others (Cu, Co), and this could be related to the amount of defects created in the system depending on the metal used for doping. Table 2.2 clearly shows the decrease in the particle size for higher Cr dopant concentrations. In contrast to the Fe-doped samples, larger BET surface areas were now measured for smaller particle sizes for xCrCZ, as is generally expected.

Table 2.2: Surface area and particle size determined by N_2 physisorption and the Scherrer equation for pure ceria-zirconia and Cr-doped ceria-zirconia.

Sample	BET surface area (m^2/g)	Particle size Scherrer (nm)
CeZrO4	67	8.0
2CrCZ	62	7.8
5CrCZ	85	6.2
11CrCZ	87	5.9
2CrCZ-800C	12	12.9
5CrCZ-800C	9	10.3
11CrCZ-800C	16	8.5

For the samples calcined at 800 °C, the BET surface area did not increase uniformly with decreasing particle size, as shown in Table 2.2. In general, the error of a BET surface area measurement can be as high as 5%, and therefore the small surface areas measured for the samples calcined at 800 °C should be interpreted with caution. The same also applies for the particle sizes determined by the Scherrer equation. More specifically, as the peak broadening

in the XRD pattern is also affected by lattice strain and dislocations, it might be that smaller particle sizes are measured than what would be expected.

Of all transition metals used for doping in this study, Cr formed the most thermally stable solid solution with ceria-zirconia. No Cr oxide species were detected by XRD for a dopant concentration of 11.11 mol% and for a calcination temperature as high as 800 °C. This result implies that most Cr is still incorporated in the crystal lattice, as is strongly suggested by the significant shift of the main reflection peak of 11CrCZ-800C to higher diffraction angles. However, it cannot be excluded that Cr oxide clusters are also present and which are too small to be detected by XRD. Conversely, Co formed the least stable solid solution with ceria-zirconia, as CeO_2-ZrO_2 phase separation already started to occur for the 11CoCZ sample calcined at 500 °C. However, still no segregated Co_3O_4 phase was formed after calcining 2CoCZ at 800 °C despite the high oxophilic nature of Co. Other studies have reported on the formation of Co_3O_4 and the difficulty of synthesizing catalysts containing cobalt mainly in the Co^{2+} state [127,133]. For example, Wen et al. reported for Co a solubility limit of only 7.5 mol% in CeO_2 [133]. TEM analysis confirmed that no Co_3O_4 phase was formed in our case after doping the ceria-zirconia support with 11.11 mol% Co, as evidenced by Figure 2.4 (left).
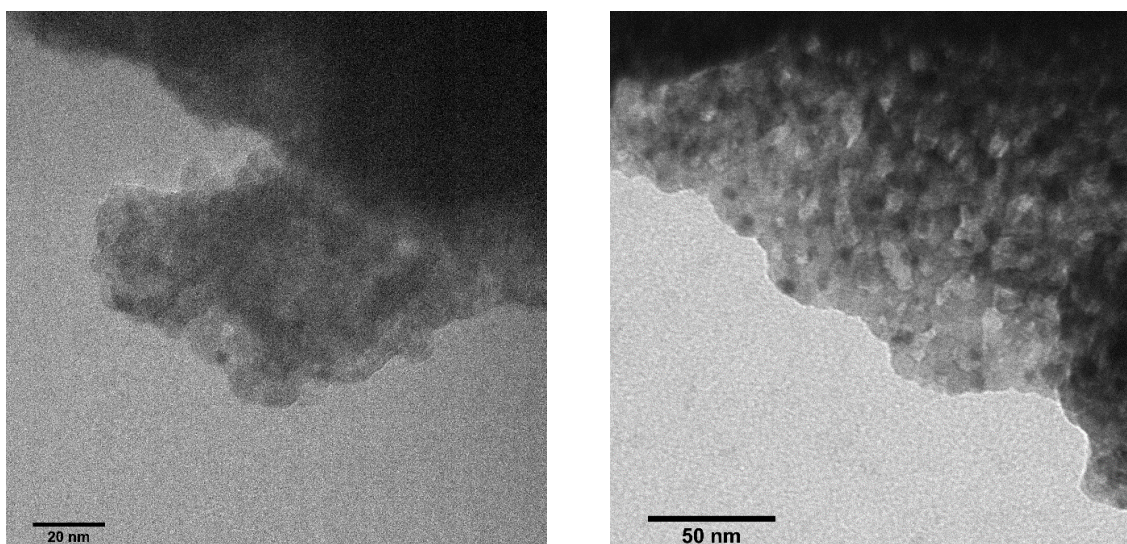
Figure 2.4: TEM pictures of 11CoCZ (left) and 11CuCZ (right).

Further, it was found that Cu formed solid solutions with ceria-zirconia with the second lowest thermal stability, after Co. This low stability can be expected due to the strong tendency for surface segregation of the Cu ions, which was already mentioned above. However, despite this segregation, still no bulk CuO nanoparticles were detected by XRD for 2CuCZ-800C. For 11CuCZ calcined at 500 °C, no CuO_x species or clusters were observed by TEM, shown in Figure 2.4 (right), indicating that these clusters are absent or very finely dispersed.

Additionally, it could be concluded from the XRD patterns that both Fe- and Ni-doped samples exhibit high thermal stabilities up to a metal loading of at least 5.55 mol% for calcination temperatures as high as 800 °C. Calcining 11FeCZ and 11NiCZ at 800 °C, on the other hand, resulted in the formation of segregated hematite and bulk NiO phases, respectively.

26

Nevertheless, XRD analysis on its own could already verify that the sol-gel method used in this study can lead to the formation of transition metal-doped ceria-zirconia solid solution systems of an exceptional high thermal stability, as was previously also suggested in the introduction of this chapter.

We further explored the sol-gel synthesis of Pd-doped ceria-zirconia because of indications from literature that one-step synthesized noble metal-based catalysts can show favorable activities towards several applications [134]. The XRD patterns of these systems are shown in Figure 2.5.
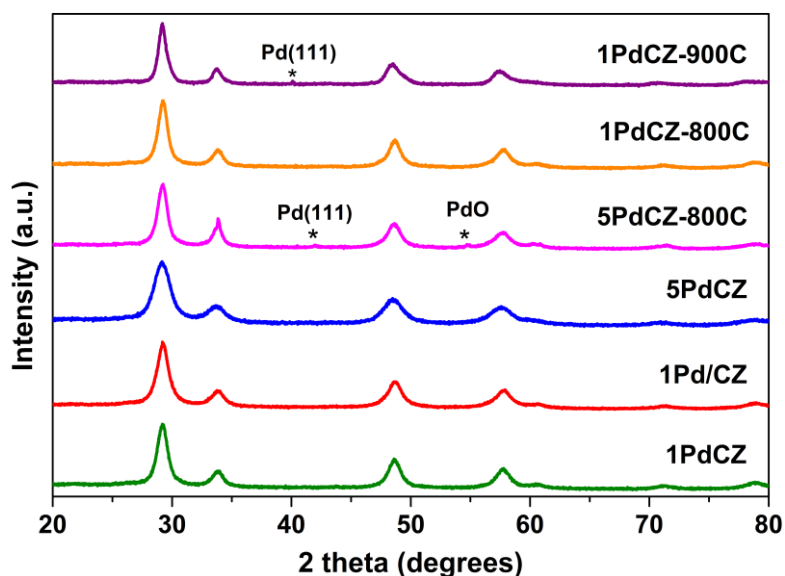
Figure 2.5: XRD patterns of Pd-based catalysts. Calcining 1PdCZ at 800 °C did not result in the formation of metallic Pd or a segregated bulk Pd oxide phase.

The XRD pattern of 1PdCZ shows that the reflection peaks are slightly shifted to lower diffraction angles (29.18°) compared with those of pure CeZrO$_4$ (29.22°). This shift indicates that lattice expansion is induced after doping CeZrO$_4$ with Pd^{2+}, despite its smaller ionic radius (0.64-0.86 Å depending the coordination) compared to that of Ce^{4+}(0.97 Å) [135]. This observation is in contrast with the previous results, where doping of CeZrO$_4$ with a smaller transition metal ion always resulted in a contraction of the CeO$_2$ fluorite lattice. The argument that the substitution of Ce^{4+} by smaller Pd^{2+} might not be occurring, or only to a limited extent, can be partially countered by the observation that the reflection peaks of 5PdCZ are shifted to even lower diffraction angles (29.15°). In addition, significant peak broadening for 5PdCZ compared to 1PdCZ was also observed, suggesting a smaller crystallite size for 5PdCZ. The decreased crystallite size might be the result of more defects formed after doping with a larger amount of Pd^{2+}, indicating the substitution of Ce^{4+} ions by Pd^{2+}. Furthermore, lattice expansion for Pd-doped CeO$_2$ was also reported by Scanlon et al. [136]. It was demonstrated by DFT analysis that Pd^{2+} is not in the same lattice position of the substituted Ce^{4+}, but shifted in one direction by ¼ of a unit cell to adopt a square-planar coordination in the cubic fluorite lattice of CeO$_2$. The Pd offset from the Ce sites to adopt a more favorable coordination geometry was further confirmed by EXAFS studies by Hiley et al., who also observed a shift of the reflection

peaks to lower diffraction angles upon increasing the Pd dopant concentration [137]. Therefore, it can be assumed that the Pd^{2+} ions in our case are adopting the same square-planar coordination as shown in these studies. The lattice expansion was explained by the fact that the Pd-O bond in an unexpanded CeO_2 lattice would be too short (~ 1.91 Å) to be physically reasonable, as the Pd-O bond in other square-planar Pd oxides was found to be significantly longer (2.01-2.07 Å).

The thermal stability of 1PdCZ and 5PdCZ was studied by calcining the samples at 800 °C in air. According to the XRD patterns, 1PdCZ appears to be stable at this temperature, as no secondary peaks corresponding to Pd metal or bulk PdO were observed in the pattern of 1PdCZ-800C. Furthermore, no PdO nanoparticles or PdO_x clusters could be found by TEM, as shown in Figure 2.6 (right).
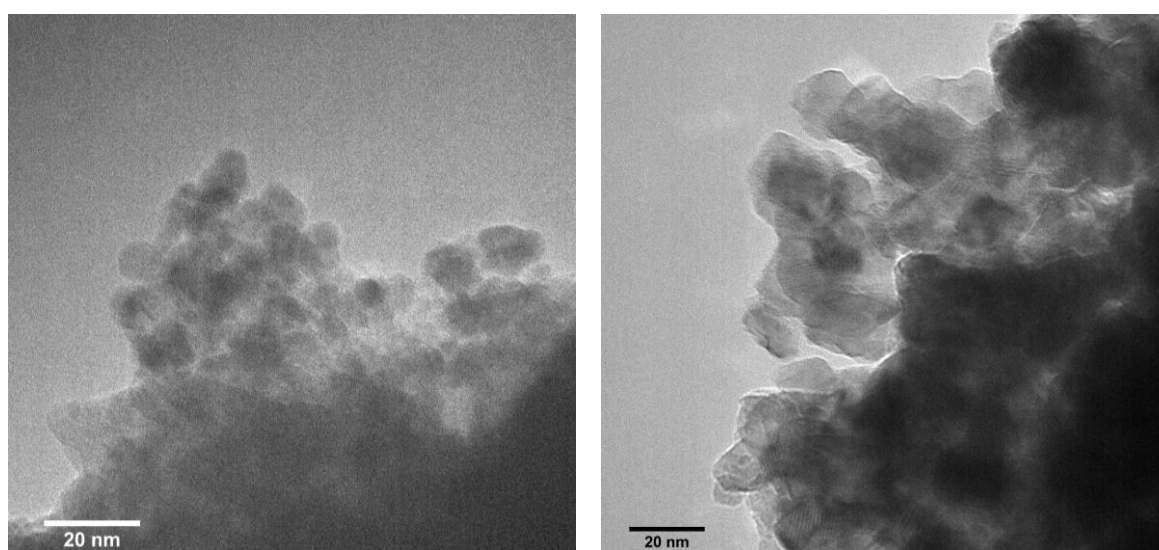
Figure 2.6: TEM pictures of 1PdCZ (left) and 1PdCZ-800C (right).

Unlike 1PdCZ, 5PdCZ was not found to be stable at 800 °C due to the presence of a small peak at approximately 42° corresponding to the (111) reflection of Pd metal, and the presence of a PdO reflection peak at approximately 54.8°. The same Pd metal reflection peak can also be seen in the XRD pattern of 1PdCZ-900C, indicating that 1PdCZ is not stable at such high temperatures. This result is consistent with the reported PdO decomposition temperature (> 800 °C in air) in the literature [138]. However, some studies reported the formation of Pd metal already at a temperature of 800 °C [78,79]. Conclusively, sol-gel synthesized 1PdCZ appears to exhibit an exceptionally high thermal stability compared to Pd-based samples synthesized with other methods.

The XRD pattern of 1Pd/CZ was also measured for comparison with pure $CeZrO_4$ and 1PdCZ. From the pattern can be seen that the main reflection peak of 1Pd/CZ is located at around the same value of the main peak of pure $CeZrO_4$ (29.22°). Therefore, it can be concluded that the support's lattice is almost unaffected by the Pd for 1Pd/CZ due to the fact that a major part of the noble metal now resides on the surface after the impregnation of the CZ support. The particle

sizes determined by the Scherrer equation and the BET surface areas of the Pd-based samples are summarized in Table 2.3.

Table 2.3: Surface area and particle size determined by N_2 physisorption and the Scherrer equation for pure ceria-zirconia and Pd-based ceria-zirconia.

Sample	BET surface area (m^2/g)	Particle size Scherrer (nm)
CeZrO$_4$	67	8.0
1PdCZ	71	8.0
1PdCZ-800C	12	10.3
5PdCZ	58	5.1
1Pd/CZ	61	8.3

The larger particle size measured for 1Pd/CZ (8.3 nm) compared to 1PdCZ (8.0 nm) suggests that doping the support might result in structural defects that can limit the growth of the crystallites during the calcination process. This reasoning is further confirmed by the broad reflection peaks observed for 5PdCZ and the corresponding small particle size (5.1 nm) as determined by the Scherrer equation. Despite the smaller particle size measured for 5PdCZ, the BET surface area was found to be significantly smaller than for 1PdCZ and even 1Pd/CZ. A similar explanation for this discrepancy can be given as was earlier proposed for the Fe- and Cr-doped samples.

3.2 X-ray Photoelectron Spectroscopy (XPS)

The speciation and dispersion of the different metal dopants were characterized by XPS. Analysis of the XPS data revealed that the surface atomic Ce/Zr ratio was 0.7 for pure $CeZrO_4$. This value corresponds to 42% to 58% of Ce to Zr, which is in agreement to the Ce/Zr ratio found for commercial $CeZrO_4$ support. No reliable XPS data for the Fe-doped samples could be obtained.
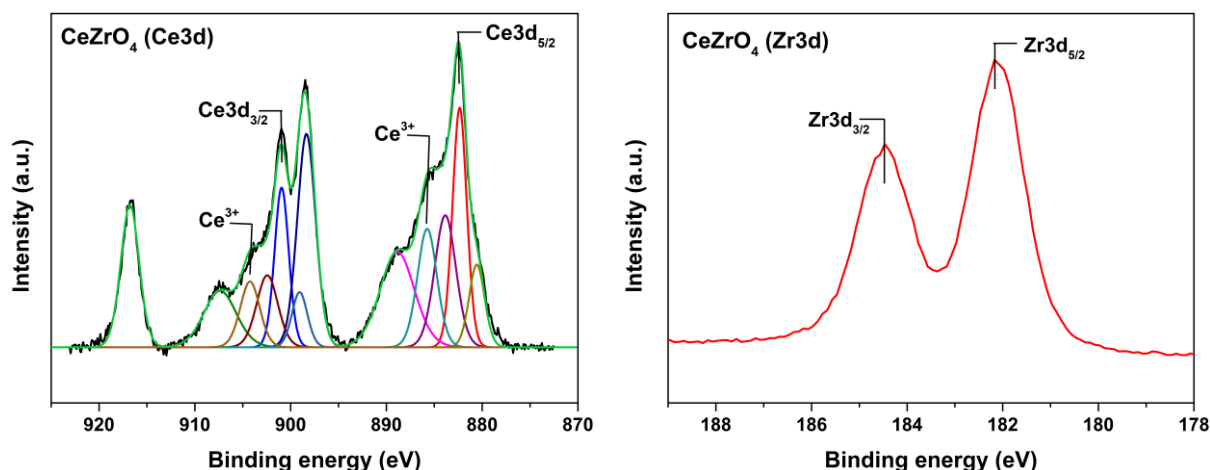

Figure 2.7: Ce3d (left) and Zr3d (right) XPS spectra of pure $CeZrO_4$.

Figure 2.7 (left) shows the XPS spectrum of Ce3d for pure $CeZrO_4$. The Ce3d spectrum is composed of eight peaks, which correspond to four pairs of spin-orbit doublets. The peaks in the high BE region correspond to the Ce $3d_{3/2}$ ionization, with the peak at 900.9 eV representing the primary Ce $3d_{3/2}$ ionization (and the peaks at 904.2 eV, 907.4 eV and 916.7 eV representing satellite features arising from the Ce $3d_{3/2}$ ionization). The Ce $3d_{5/2}$ ionization, on the other hand, is represented by the peaks observed in the lower BE energy region, with the peak at 882.3 eV representing the primary Ce $3d_{5/2}$ ionization (and the peaks at 885.7 eV, 889.0 eV and 898.3 eV representing its satellite features). The two peaks observed at 885.7 and 904.2 eV indicate the presence of Ce^{3+} in $CeZrO_4$, while the other six peaks correspond to Ce^{4+}. As Ce^{3+} is associated to the presence of oxygen vacancies, more insight into the amount of these vacancies can be gained by calculating the Ce^{3+}/Ce^{4+} ratio for each sample. For $CeZrO_4$, this ratio was found to be 0.176, and it is expected that this ratio will further increase when the support is doped with transition metal ions with a lower valence state than Ce^{4+}.

The XPS doublet spectrum of Zr 3d is given in Figure 2.7 (right). The two peaks at 182.0 eV and 184.4 eV correspond to Zr $3d_{5/2}$ and Zr $3d_{3/2}$, respectively. The shift of the spectrum to lower binding energies compared to that of ZrO_2 (0.5 eV difference) is most likely due to the different electronic environment created when ZrO_2 forms a solid solution with CeO_2 [139].

The O 1s spectrum of all measured samples showed two speaks. The main peak, located around 529.5 eV, and a shoulder peak at a slightly higher binding energy were assigned to lattice oxygen and chemisorbed oxygen on the surface, respectively [140]. Several studies

30

demonstrated the high reactivity of these chemisorbed oxygen species, and it was assumed that these oxygen species might play a crucial role in certain oxidation reactions [141].
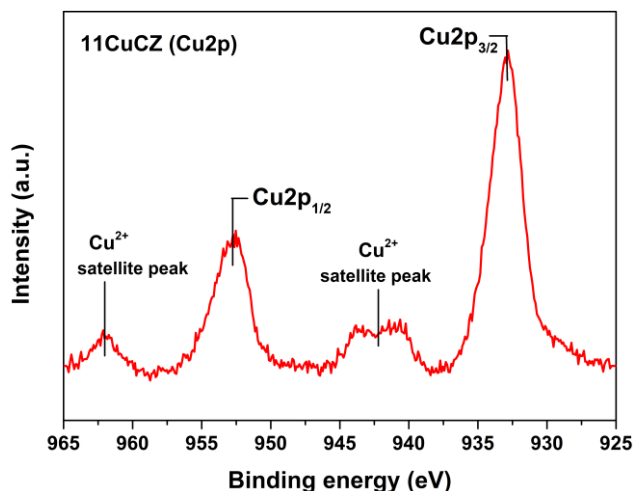
Figure 2.8: Cu2p XPS spectrum of 11CuCZ. The satellite peak (940-945 eV) confirms the presence of Cu^{2+} species in the Cu-doped sample.

The Cu2p spectrum of 11CuCZ is shown in Figure 2.8. Typically, a $Cu2p_{3/2}$ peak located at high binding energy (933.0-933.8 eV) in combination with a satellite peak (940-945 eV) indicates the presence of Cu^{2+} species. Conversely, if the main $Cu2p_{3/2}$ peak is located at a slightly lower binding energy (932.2-933.1 eV), without the observation of a satellite feature, then most likely Cu^+ species are present in the sample. In our case, a satellite peak was observed for all Cu-doped samples, indicating the existence of Cu^{2+} ions. However, as the main $Cu2p_{3/2}$ peaks were located at the relatively low binding energies of 932.5 eV, 932.8 eV and 932.9 eV for 2CuCZ, 5CuCZ and 11CuCZ, respectively, both Cu^{2+} and Cu^+ ions are most likely present in these samples. In addition, the relative intensity of the satellite feature with respect to the main peak was found to be lower than 0.55 for all Cu-doped samples, which also indicates that Cu^+ ions exist along with Cu^{2+} ions [142].

As the binding energy of the main $Cu2p_{3/2}$ peak is almost identical for Cu^+ and Cu^0, it is difficult to distinguish these two copper states from each other. Therefore, the Cu LMM Auger spectrum (not shown) is often used to determine whether Cu^+ or Cu^0 is present on the surface of the support. In the spectra of the Cu-doped samples calcined at 800 °C, the peak observed at 571.4 eV for 2CuCZ-800C was attributed to Cu^+, while the peak at 568.8 eV for 11CuCZ-800C was attributed to Cu^0 [143]. This finding is consistent with the XRD patterns, which showed the presence of Cu^0 for 11CuCZ-800C, but the absence of it for 2CuCZ-800C.
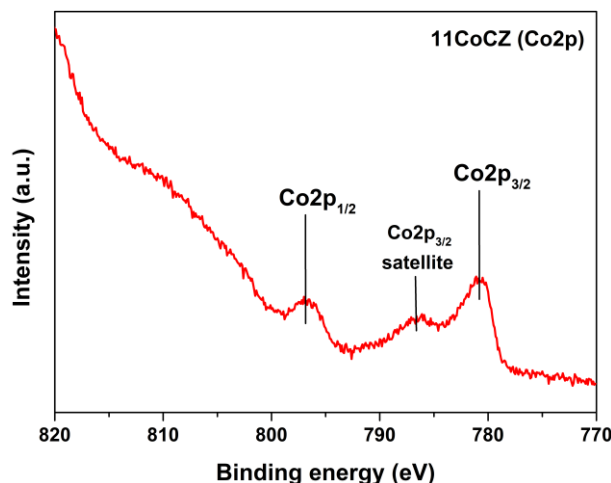
Figure 2.9: Co2p XPS spectrum of 11CoCZ. The satellite peak at 786.3 eV indicates that Co is mainly present in the +2 chemical state.

The Co2p spectrum of 11CoCZ is shown in Figure 2.9. It can be seen from the figure that part of the binding energy region corresponding to Co2p$_{1/2}$ is overlapping with the Ce3d scanning region. Therefore, the interpretation and calculations were carried out based on the Co2p$_{3/2}$ core lines. The Co2p$_{3/2}$ satellite peak at 786.3 eV indicates that CoO, and not Co$_3$O$_4$, is present in the CZ support doped with high Co content. This result is quite remarkable, considering the highly oxophilic nature of cobalt, and as many other studies have demonstrated the presence of Co$_3$O$_4$ when using such high Co dopant concentrations [127,133]. An additional proof of the absence of Co$_3$O$_4$ was found in the color of the sample, being dark brown, while the Co doped samples calcined at 800 °C showed the typical black color of Co$_3$O$_4$.
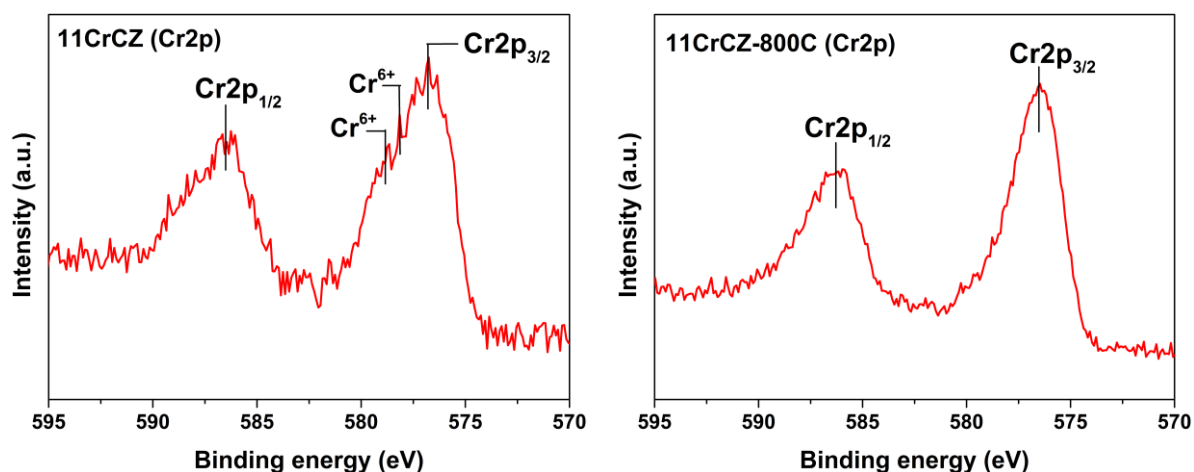
Figure 2.10: Cr2p XPS spectra of 11CrCZ (left) and 11CrCZ-800C (right).

The Cr2p spectrum of 11CrCZ is shown in Figure 2.10 (left). The main 2p$_{3/2}$ peak at 576.7 eV and the main 2p$_{1/2}$ peak 586.4 eV confirms the presence of Cr^{3+} species in 11CrCZ [144]. The 2p$_{3/2}$ peak showed two small shoulders at 578.0 and 579.0 eV, indicating the presence of Cr^{6+} species. These two shoulders were also observed for 2CrCZ and 5CrCZ, although less intense than for 11CrCZ. For 11CrCZ-800C, shown in Figure 2.10 (right), these two shoulders were even less pronounced, suggesting that more Cr^{3+} species (e.g. Cr$_2$O$_3$) might have been formed

on the surface after the calcination at 800 °C. The shift of the main $2p_{3/2}$ peak to a lower binding energy (576.4 eV) also supports this assumption. Conversely, for 2CrCZ-800C the two shoulders were still clearly visible, and the position of the main $2p_{3/2}$ peak at a relative high binding energy of 577.0 eV demonstrates that Cr is still oxidized and most likely in a mixed Cr^{3+}/Cr^{6+} chemical state.
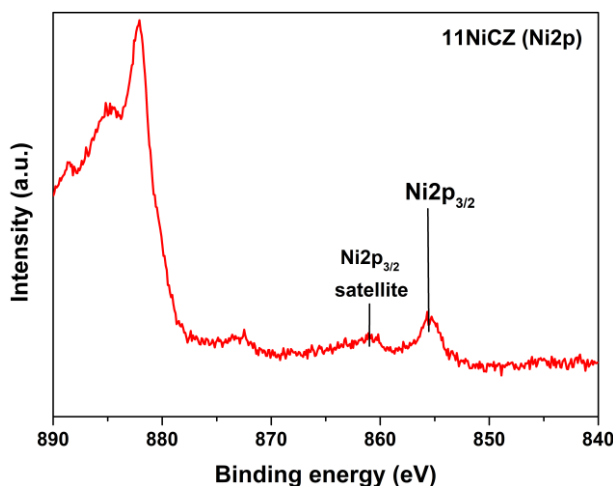
Figure 2.11: Ni2p XPS spectrum of 11NiCZ.

Similar to the case of xCoCZ, the $Ni2p_{1/2}$ binding energy region is strongly overlapping with the Ce3d binding energy region, as shown in Figure **??**. Nevertheless, it can be derived from the high binding energy observed for the main $Ni2p_{3/2}$ peak (855.6 eV) that Ni is in a highly ionic Ni^{2+} oxidation state. [145]. This high binding energy suggests that strong Ni-O-Ce bonds are formed and that Ni^{2+} forms a solid solution with CeO_2-ZrO_2, as the $Ni2p_{3/2}$ peak for Ni^{2+} in bulk NiO is typically located at a much lower binding energy (around 853.7 eV). Further, the fact that no metallic Ni is formed is clear from the $Ni2p_{3/2}$ satellite peak centered at around 861.1 eV, which would be much broader and smaller in intensity for Ni^0.

The molar percentages of the different transition metal dopants, calculated from the XPS peak areas, were compared with the theoretical concentrations. These results are summarized in Figure 2.12. Substantial surface enrichment of Cu ions was observed for the xCuCZ samples, confirming the results earlier reported in the literature on Cu doped CeO_2-based oxides. Surface enrichment of the metal dopant was also observed for xCoCZ, although less pronounced than for the xCuCZ samples. These results might explain why crystal lattice disintegration into a Ce- and Zr-rich phase was more favored for the Cu- and Co-doped supports, as was previously observed from the XRD analysis. Figure 2.12 further shows that Cr ions segregate only to a limited extent to the surface of the support, while after the calcination at 800 °C this segregation was more significant. In contrast to all other transition metals, Ni seems to form an almost perfect homogeneous solid solution with ceria-zirconia.
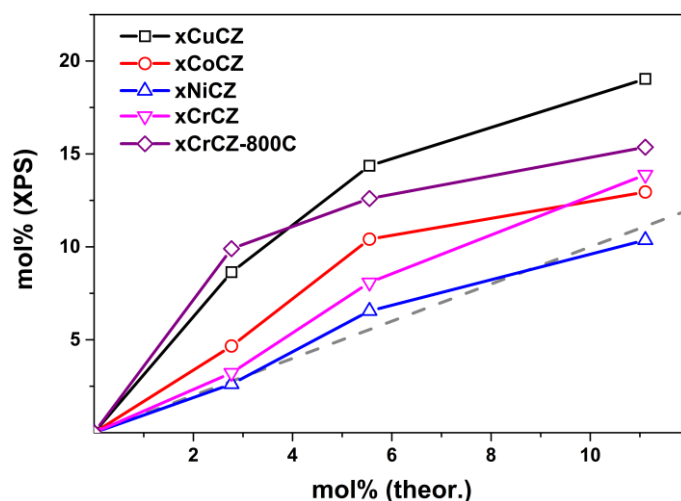
Figure 2.12: Mole percentages of the metal dopants determined by XPS versus theoretical mole percentages. XPS mole percentages close to the dashed line suggest the formation of a perfectly homogeneous solid solution system, while values below or above this line indicate that, respectively, surface segregation and sintering occurred.

Finally, it was concluded that surface enrichment of the metal dopants could be beneficial in terms of the catalytic activity. Because heterogeneous catalytic reactions occur on the surface of the catalyst, the presence of these metal dopants in the surface and subsurface region of the support could positively influence the conversion efficiencies of the reactants.
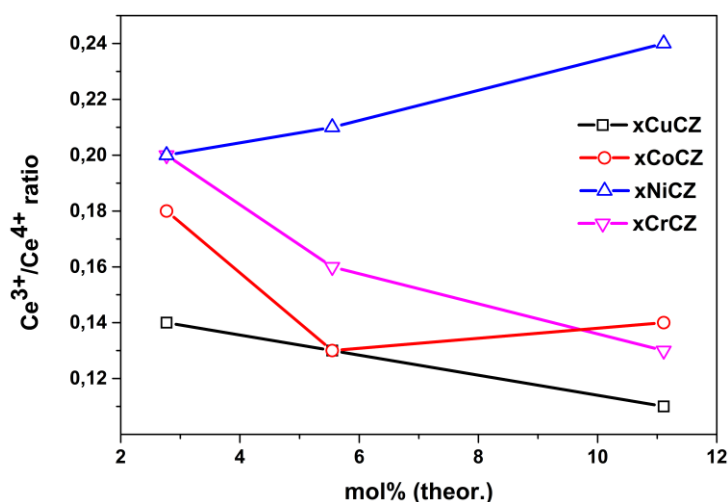
Figure 2.13: Ce^{3+}/Ce^{4+} ratios calculated from the fitted Ce3d XPS spectra of the different transition metal-doped ceria-zirconia samples.

XPS was further used to gain more insight into the amount of oxygen vacancies created after the doping of the ceria-zirconia support. The Ce^{3+}/Ce^{4+} ratios were calculated from the XPS spectra of the Ce3d core lines, and it is typically expected that for a higher dopant concentration the ratio increases due to the formation of more oxygen vacancies. Furthermore, these vacancies are believed to play an important role in the CO + NO and CO + O_2 reactions [28,146]. The ratios obtained for the different transition metal dopants are shown in Figure 2.13.

It can be seen from the figure that the Ce^{3+}/Ce^{4+} ratio decreases uniformly for higher Cr and Cu dopant concentrations. At first sight, this might seem contradicting with the abovementioned expectation. However, a decrease of the Ce^{3+}/Ce^{4+} ratio typically signifies that the metal dopants are starting to segregate, and therefore these results seem to be strongly in line with the results shown in Figure 2.12. The strong surface enrichment of the Cu ions demonstrated by Figure 2.12 could explain why the lowest Ce^{3+}/Ce^{4+} ratios were found for the xCuCZ samples. Furthermore, there was less surface enrichment of the dopant ions observed for 2CrCZ and 5CrCZ compared to 2CoCZ and 5CoCZ, explaining why the former show higher Ce^{3+}/Ce^{4+} ratios in Figure 2.13. Conversely, more surface enrichment was observed for 11CrCZ than for 11CoCZ, which in turn could explain why the Co-doped sample shows a higher Ce^{3+}/Ce^{4+} ratio than the Cr-doped sample for a dopant concentration of 11.11 mol%. Finally, in the case of the Ni-doped samples, a near perfectly homogeneous solid solution system was formed as demonstrated by Figure 2.12. If there would be no segregation of the dopant ions occurring, it can be expected that the Ce^{3+}/Ce^{4+} ratio will increase for a higher dopant concentration. Indeed, this reasoning was confirmed by Figure 2.13, showing that the highest Ce^{3+}/Ce^{4+} ratio was obtained for 11NiCZ.

Table 2.4: XPS results for the Pd-based samples.

Sample	Pd binding energy (eV)	Pd mol% (XPS)	Pd mol% (theor.)	Ce^{3+}/Ce^{4+}
1PdCZ	337.7	1.80	1.44	0.20
1PdCZ-800C	337.7	4.51	1.44	0.18
1PdCZ-900C	337.0	1.27	1.44	0.12
5PdCZ	337.7/336.2	10.42	7.29	0.21
5PdCZ-800C	336.7	9.42	7.29	0.16
1Pd/CZ	337.4	3.53	1.44	0.25

The XPS data of the Pd-based samples are summarized in Table 2.4. The high binding energy observed for Pd in 1PdCZ (337.7 eV) indicates that Pd is in a highly ionic and dispersed Pd^{2+} state [147]. This observation suggests a strong metal-support interaction in the Pd-doped ceria-zirconia, which is confirmed by the high binding energy that is maintained for Pd (337.7 eV) after calcining the sample at 800 °C. The increase in the molar percentage of Pd from 1.80 to 4.51 after the calcination points at the segregation of the noble metal to the surface of the support at elevated temperatures. This can also visually be derived from the Pd3d spectra shown in Figure 2.14, where it can be seen that the intensity of the $Pd3d_{5/2}$ peak in the Pd3d spectrum of 1PdCZ-800C is significantly higher than for the same peak in the Pd3d spectrum of 1PdCZ. In addition, Figure 2.14 also shows that the Pd3d core lines are strongly overlapping with the Zr3p core lines. Hence, the XPS results for the Pd-based samples should be interpreted with caution. Nevertheless, the presence of a higher amount of surface Pd in a highly dispersed state for 1PdCZ-800C may finally result in an improved catalytic activity for this sample compared to the uncalcined 1PdCZ, if no sintering would take place. Furthermore, doping the ceria-zirconia support with 1 wt.% Pd resulted in an increase in the Ce^{3+}/Ce^{4+} ratio from 0.17 to 0.20, indicating the formation of oxygen vacancies when the lower valent Pd^{2+} ion is incorporated in the fluorite crystal lattice. The slightly lower Ce^{3+}/Ce^{4+} ratio for 1PdCZ-800C (0.18) could

indicate that some sintering of the Pd occurred. Still, these results are quite remarkable, as it is known that bulk PdO oxide species are decomposing around 800 ºC [78,79]. This result is also consistent with XRD, where it was shown that no metallic Pd was formed at 800 °C for 1PdCZ.
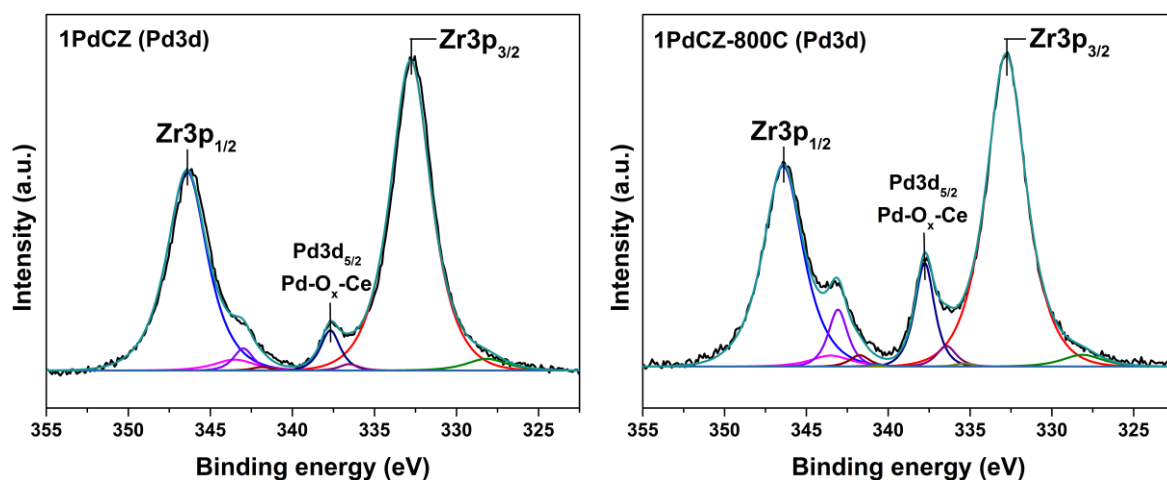
Figure 2.14: Pd3d XPS spectra of 1PdCZ (left) and 1PdCZ-800C (right).

It was previously observed from the XRD patterns that calcining 1PdCZ at 900 °C results in the formation of Pd metal, which is further confirmed by the decrease in the Pd binding energy for 1PdCZ-900C. Furthermore, the small amount of surface Pd (1.27 mol%) detected for 1PdCZ-900C indicates that sintering of the noble metal phase occurred. Finally, the decrease in the Ce^{3+}/Ce^{4+} ratio also suggests that the noble metal is no longer incorporated in the fluorite type lattice of the ceria-zirconia support. Figure 2.15 gives a more visual representation of the amount of surface Pd present for each sample.
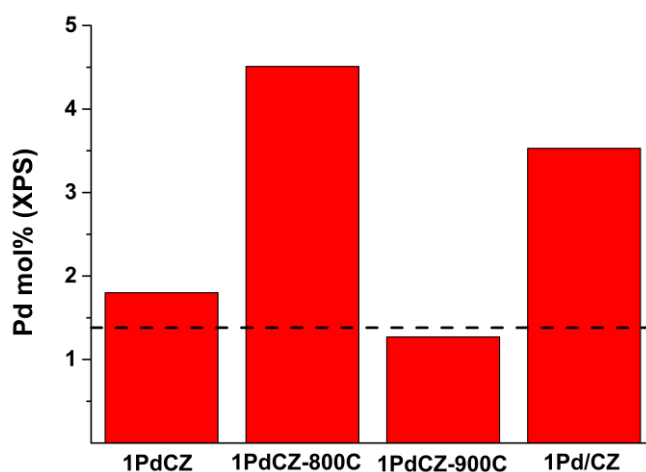
Figure 2.15: Graphic representation of the Pd loadings determined by XPS.

XPS measurements were also performed for the ceria-zirconia support doped with 5 wt.% Pd. In the Pd3d spectrum of 5PdCZ (Figure 2.16 (left)) the Pd peak shows a small shoulder at a binding energy of 336.2 eV. Hence, it was concluded that besides highly ionic Pd^{2+} (337.7 eV) a small fraction of PdO_x clusters are also present in 5PdCZ, and which have escaped XRD

detection. The high Pd loading recorded by XPS (10.42 mol%), as well as the minor increase in the Ce^{3+}/Ce^{4+} ratio compared to 1PdCZ, further confirms that Pd has segregated to the surface of the support. It should be noted that these results are not completely unexpected, as the fluorite lattice of CeO_2 has already been doped with a large amount of Zr^{4+} ions. Thus, further doping the support with a high amount of Pd^{2+} ions (5 wt%) might not be favorable and might distort the crystal lattice significantly, leading to increased migration of palladium to the surface of the support. The fact that a lower amount of surface Pd was recorded after the calcination at 800 °C suggests that sintering might have taken place, which is further confirmed by the decreased binding energy of Pd and the lower Ce^{3+}/Ce^{4+} ratio measured for 5PdCZ-800C. This observation is also consistent with the XRD result, which indicated the presence of both Pd metal and bulk Pd oxide for 5PdCZ-800C. The binding energy for Pd in 5PdCZ-800C, however, was 336.7 eV, indicating that Pd is in the form of PdO_x clusters. Thus, it was assumed that more than one Pd species is present in 5PdCZ-800C. This can also be derived from the Pd3d$_{5/2}$ peak in Figure 2.16 (right), for which a small shoulder can be seen at 337.4 eV.
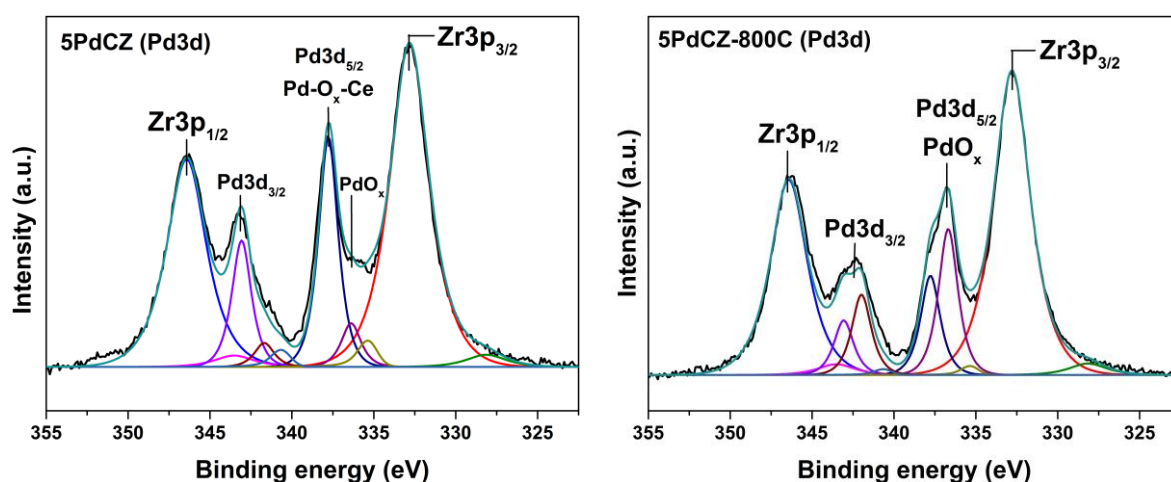
Figure 2.16: Pd3d XPS spectra of 5PdCZ (left) and 5PdCZ-800C (right).

For the Pd-impregnated ceria-zirconia support, a relatively high binding energy for Pd (337.4 eV) could still be observed. Therefore, strong metal-support interactions can generally be expected for CeO_2-ZrO_2 mixed oxides synthesized with the highly advanced sol-gel method used in this study. Since XPS is a surface sensitive technique, the enrichment of the surface by Pd after impregnation of the support explains why virtually more Pd is observed (3.53 mol%) compared to the intended loading (1.44 mol%). Surprisingly, the Ce^{3+}/Ce^{4+} ratio for 1Pd/CZ (0.25) was found to be significantly larger than for 1PdCZ (0.20), while in reality a higher ratio and thus more oxygen vacancies are expected for the Pd-doped sample compared to the impregnated sample. This is further supported by a study of Boronin et al., where it was reported that impregnating CeO_2 with Pd resulted in a decrease of the Ce^{3+}/Ce^{4+} ratio from 0.25 to 0.20 [147]. Hence, no satisfying explanation could be found in the end for this observation.

3.3 UV-Vis spectroscopy

UV-Vis spectroscopy was used to gain more insight into the oxide speciation of the different metal dopants. Furthermore, this technique is also often used to determine the coordination environment of metal ions.

The UV-Vis spectrum of pure ceria-zirconia is shown in Figure 2.17 together with the spectra of the Fe-doped samples. The number of absorption bands observed for pure ceria-zirconia in the low-wavelength region depends strongly on the Ce/Zr ratio and the synthesis method applied. In our case, only two absorption bands were observed at 252 and 340 nm, while Nandi et al. observed at least four absorption bands in the region from 200 to 400 nm [148]. In the literature, the absorption band located around 250 nm is typically assigned to the ligand-to-metal charge transfer (LMCT) transition from O^{2-} to Ce^{3+} [149]. The absorption band centered at around 340 nm, on the other hand, is often attributed to interband transitions of CeO_2 and the LMCT transition from O^{2-} to Zr^{4+} [148,150]. An absorption band is also often observed around 290 nm, which corresponds to the LMCT transition from O^{2-} to Ce^{4+} [149,150]. In our case, however, this band seems to be absent, despite the fact that there are more Ce^{4+} ions than Ce^{3+} ions in $CeZrO_4$. Hence, it was concluded that several absorption bands might be overlapping. Further, the pronounced absorption band at 252 nm might also indicate that a significant amount of Ce^{3+} ions are present, and which are strongly associated with oxygen vacancies in the support.
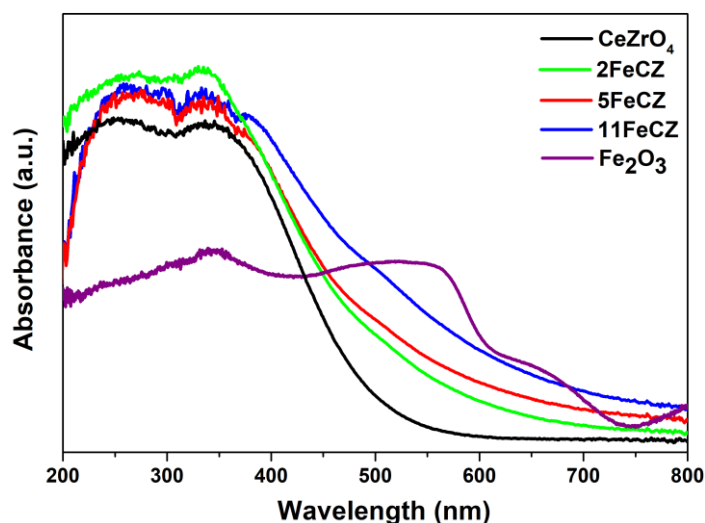
Figure 2.17: UV-Vis spectra of pure ceria-zirconia and Fe-doped ceria-zirconia samples.

No absorption bands were observed in the visible wavelength region for $CeZrO_4$. This is consistent with the d^0 electronic configuration of the Ce^{4+} and Zr^{4+} ions, as d-d crystal field transitions are often responsible for the absorption in the visible wavelength range. Doping the ceria-zirconia support with transition metal ions, however, increased the absorption in this region significantly. Furthermore, after doping the support the strong absorption bands in the low-wavelength region became slightly red-shifted. This result suggest that the band gap energy of ceria-zirconia decreased and/or that additional energy levels were introduced in the interband

gap region, indicating that the dopant ions were incorporated into the crystal lattice and that a solid solution was formed with ceria-zirconia.

The UV-Vis spectra of the Fe-doped samples are also shown in Figure 2.17. Hematite (Fe_2O_3) was measured as a reference sample to determine whether Fe oxide clusters or agglomerates are present in xFeCZ. The band at 350 nm can be assigned to oligomeric clusters of α-Fe_2O_3, while the sub-bands above 400 nm correspond to d-d electronic transitions in larger Fe_2O_3 particles [151]. 2FeCZ and 5FeCZ display a similar absorption behavior, with only weak absorption in the visible wavelength range. 11FeCZ, on the contrary, showed a higher absorption in this range, suggesting that the nature of the iron species in 11FeCZ is different than these in 2FeCZ and 5FeCZ. Since no distinct absorption bands were observed in the visible wavelength range for 11FeCZ, the Fe is most likely not in the form of bulky Fe oxide agglomerates [152]. Alternatively, it can be concluded that some Fe oxide clusters might be present on the surface of 11FeCZ. However, as no separate Fe_2O_3 phase was derived from TEM analysis and XRD for 11FeCZ, the iron oxide clusters must be small and/or highly dispersed on the surface of the support.

Figure 2.18: UV-Vis spectra of pure ceria-zirconia and Cu-doped ceria-zirconia samples.

Figure 2.18 shows the UV-Vis spectra of the Cu-doped samples as well as a CuO reference. The reference sample shows high absorption in the visible wavelength range which decreases gradually in intensity at shorter wavelengths. After doping ceria-zirconia with Cu, a new band appears in the range of 650-800 nm, indicative of the d-d transition of Cu^{2+} ions located in an octahedral environment [153]. As it has been shown by Kappis et al. via EPR studies that Cu^{2+} can adopt an octahedral coordination in CeO_2 with a tetragonal distortion, it can be assumed that these bands are not originating from Cu^{2+} ions in bulk crystalline CuO [154]. The fact that no bulk CuO was detected by XRD for 2CuCZ after calcining the sample at 800 °C further confirms this reasoning. In other words, the formation of a solid solution between Cu and ceria-zirconia can be concluded.

Figure 2.19: UV-Vis spectra of pure ceria-zirconia and Co-doped ceria-zirconia samples.

The UV-Vis spectra of the xCoCZ samples were compared with a Co_3O_4 reference spectrum in Figure 2.19. Three absorption bands were identified in the reference spectrum of Co_3O_4. The absorption band at 254 nm corresponds to the bonding-antibonding electronic transition between cobalt and oxygen, while the absorption bands at 465 and 750 nm are associated with the LMCT transitions from O^{2-} to Co^{2+} and from O^{2-} to Co^{3+}, respectively [155,156]. The Co^{2+} and Co^{3+} ions in Co_3O_4 typically adopt a tetrahedral and octahedral geometry, respectively. None of the xCoCZ samples showed absorption bands that could point to the presence of a segregated Co_3O_4 phase, and this result is in agreement with XRD, XPS and TEM analysis. No explanation could be given for the higher absorption shown by the 5CoCZ sample compared to the 11CoCZ sample.

Figure 2.20: UV-Vis spectra of Cr-doped ceria-zirconia samples.

In Figure 2.20, three absorption bands are visible for the Cr_2O_3 reference sample. The first band, located at 375 nm, can be ascribed to the band gap transition of Cr^{4+} ions, while the other two peaks located at 470 an 605 nm correspond to d^3 electronic transitions of the Cr^{3+} ions in six-

40

coordinate geometry and octahedral symmetry, respectively [157,158]. No distinct absorption bands are visible in the UV-Vis spectra of the xCrCZ samples that could indicate the presence of a segregated Cr_2O_3 phase, which is in line with XRD, XPS and TEM analyses. For the xCrCZ-800C samples, however, the absorption in the visible wavelength range increased significantly. A broad band was visible for 2CrCZ-800C located between the two absorption bands of Cr_2O_3 at 470 and 605 nm, thereby indicating that small Cr_2O_3 clusters might have been formed. For 5CrCZ-800C, a second absorption band started to appear at slightly lower wavelengths, while for 11CrCZ-800C two broad and distinct absorption bands were observed around 497 and 589 nm. These results are in line with the XPS measurements which showed significant surface enrichment of Cr ions after the calcination at 800 °C. However, due to the fact that no segregated Cr_2O_3 phase was detected by XRD, it can be assumed that only small Cr_2O_3 clusters might have been formed after the calcination process.
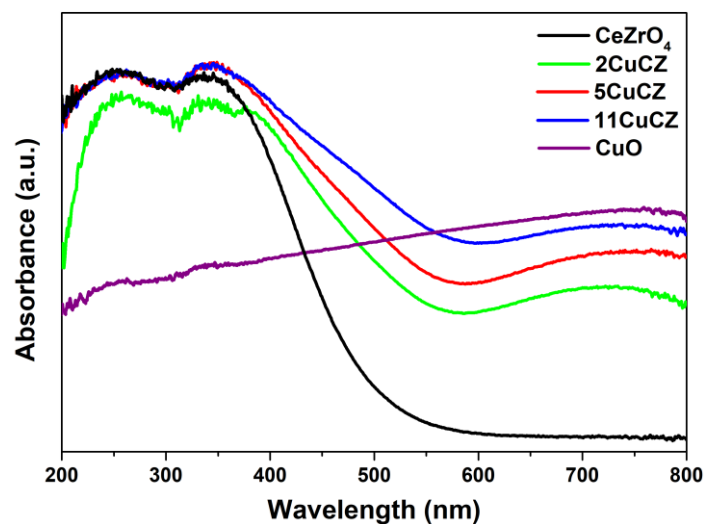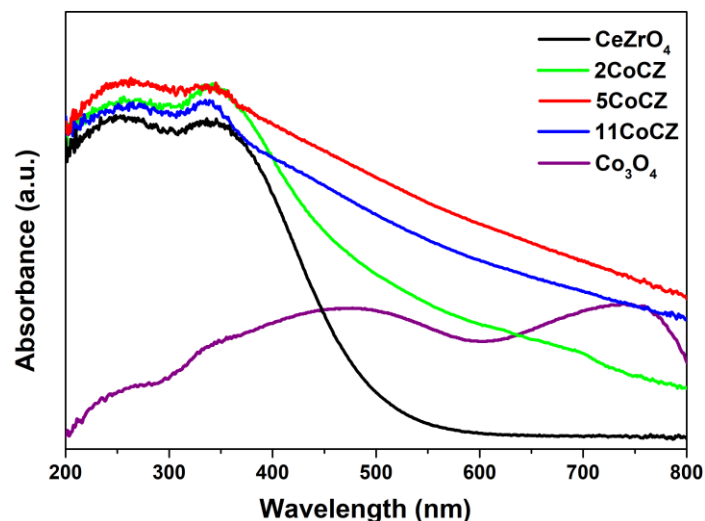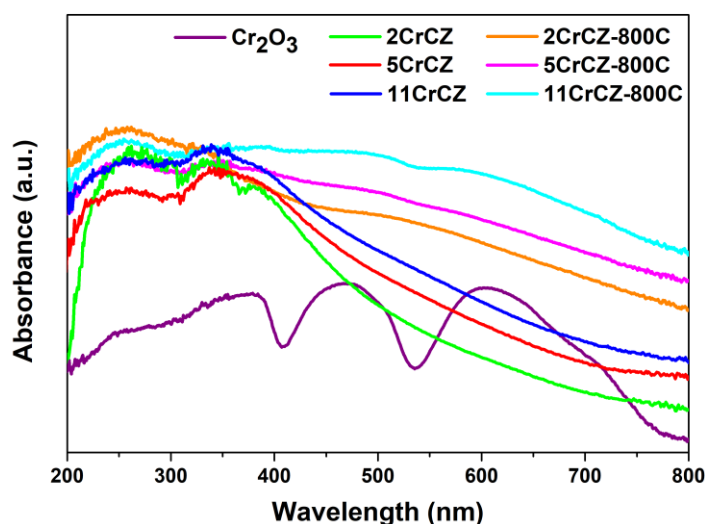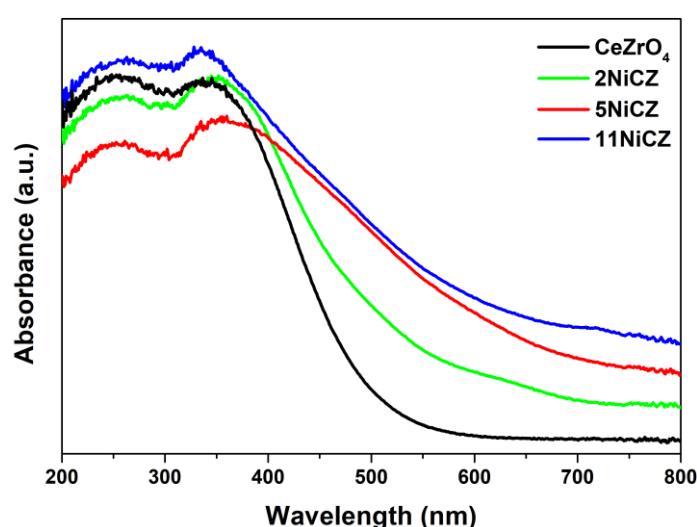

Figure 2.21: UV-Vis spectra of pure ceria-zirconia and Ni-doped ceria-zirconia samples.

The UV-Vis spectra of the Ni-doped samples in Figure 2.21 were compared with the UV-Vis spectrum of pure NiO found in the literature. NiO shows a strong absorption in the UV region, which can be ascribed to its band gap absorption [159,160]. Since no new absorption bands were observed in the UV region after doping ceria-zirconia with Ni, it can be concluded that no free NiO was formed, which is in agreement with XRD measurements for these samples. The small bump centered at 750 nm can be assigned to the d-d bands of Ni^{2+} in octahedral coordination, pointing to the formation of a solid solution between Ni and ceria-zirconia. [161,162].

The UV-Vis spectra of the Pd-doped samples are shown in Figure 2.22. The two absorption bands at 338 and 438 nm in the UV-Vis reference spectrum of bulk PdO were assigned to the LCMT charge transfer transition from O^{2-} to Pd^{2+} and d-d electron transitions in the Pd^{2+} ion, respectively [163]. The similar absorption spectra of 1PdCZ and 1PdCZ-800C indicate that Pd^{2+} remains in a highly ionic and dispersed state after the calcination at 800 °C, and that no PdO nanoparticles or Pd^0 were formed. Conversely, the UV-Vis spectrum of 1PdCZ-900C suggests that Pd^{2+} has been converted to metallic Pd, as can be derived from the low absorption intensity

in the visible wavelength range for this sample. This low intensity confirms that Pd^{2+} no longer contributes to the absorption in 1PdCZ-900C. In contrast, the opposite seems to be true for the 5PdCZ, which strongly absorb in the visible wavelength range from 400 to 800 nm. The significant shift of the absorption edge of pure $CeZrO_4$ to longer wavelength values indicates the incorporation of a high amount of Pd^{2+} ions in the fluorite type crystal lattice of the support. However, derived from the broad absorption band observed for 5PdCZ centered at around 450 nm, the presence of small PdO clusters cannot be excluded. For 5PdCZ-800C, a small but distinct absorption band appeared around 500 nm, which was attributed to bulk PdO nanoparticles [163]. The presence of this phase was previously also confirmed by XRD.
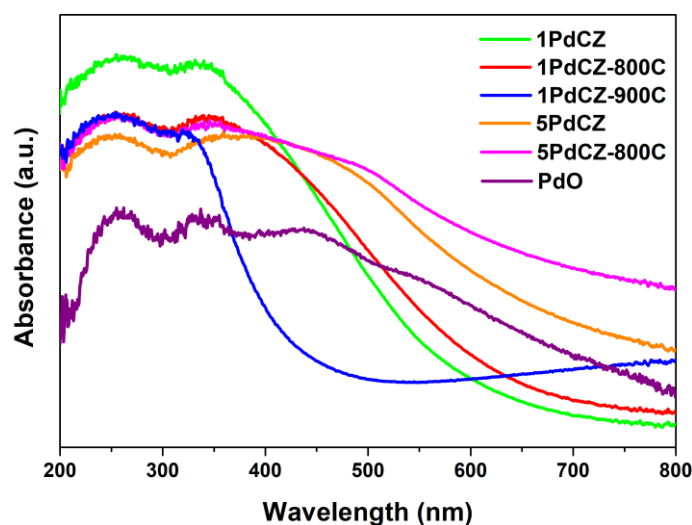
Figure 2.22: UV-Vis spectra of Pd-doped ceria-zirconia samples.

3.4 Hydrogen-Temperature Programmed Reduction (H₂-TPR)

Temperature-programmed reduction (TPR) has been widely used for studying the reduction/oxygen-storage properties of CeO_2-based mixed oxides. In addition, TPR is a valuable technique that can provide more insight into the interactions between the doped or impregnated transition metal and the support. Since doping $Ce_{0.5}Zr_{0.5}O_2$ with a small transition metal ion induces strain and creates defects in the support's lattice, the oxygen mobility in the support is expected to increase, and this can significantly contribute to the catalytic redox properties of the solid solution system. Finally, it has been shown that solid solution systems with high homogeneity display a favorable reduction behavior and increased OSC [164].

The H₂-TPR profiles of the xCuCZ, xFeCZ, xCoCZ, xCrCZ and xNiCZ samples were measured and compared to the reduction profile of pure $CeZrO_4$. Since Zr^{4+} is a non-reducible cation, the small reduction peak at 565 °C observed for pure $CeZrO_4$ can only arise from the reduction of surface Ce^{4+} to Ce^{3+} [165,166]. The reduction of bulk Ce^{4+} is expected to occur at temperatures higher than the measured temperature range.
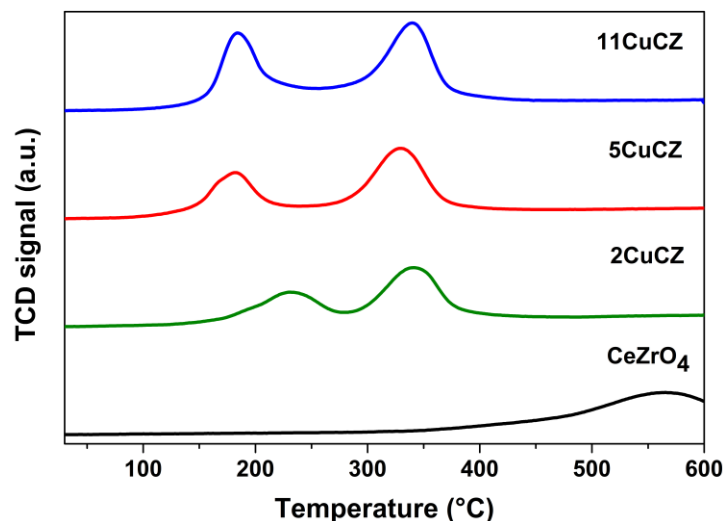
Figure 2.23: H$_2$-TPR profiles of ceria-zirconia and Cu-doped ceria-zirconia samples.

The reduction profiles of the Cu-doped samples are shown in Figure 2.23. The two peaks observed between 150 and 350 °C correspond to the reduction of two different Cu species in the solid solution system. The first peak may be attributed to the reduction of highly dispersed Cu^{2+} and Cu$^+$ ions strongly interacting with the reducible support. This follows from the work of Zhang et al. who showed that copper species with a smaller particle size interacted more strongly with CeO$_2$, leading to a higher reducibility due to the promoting effect of the reducible support [167]. Consequently, reduction peaks at slightly higher temperatures should correspond to copper species with a larger particle size, as they interact less strongly with CeO$_2$ and resemble more bulk CuO that is reduced at much higher temperatures. Indeed, several research groups attributed the second peak to the reduction of large copper oxide nanoparticles or clusters, which is in agreement with their observation of a secondary CuO phase in the XRD patterns [167,168]. In our case, however, no segregated bulk CuO phase was observed from XRD, and therefore the second reduction peak might be attributed to the reduction of finely dispersed copper oxide clusters, which escaped XRD detection and which were tentatively explained with UV-Vis spectroscopy to be present on the surface of the catalyst.

It might be the case, however, that the finely dispersed copper oxide clusters are reduced simultaneously with the Cu^{2+} and Cu$^+$ ions in close contact with the support. The second reduction peak can then alternatively be explained by the reduction of Cu^{2+} and Cu$^+$ ions which are located more deeply in the solid solution system. If this would be the case, then the absorption band observed in the UV-Vis spectra at high wavelengths might indeed be coming from the absorption of light by Cu^{2+} ions with an octahedral coordination inside the fluorite lattice of the support. This reasoning is further confirmed by previous work of Luo et al., who found that after acid treating their catalyst the first reduction peak disappeared, while the second peak could still be observed [169]. It was reasoned that the Cu^{2+} inside the solid solution could survive the acid treatment, while the finely dispersed copper oxide species on the surface could be easily removed. In addition, an associated decrease in catalytic activity was observed for the acid treated samples. This result further suggests that highly dispersed copper oxide species on the surface represent the active phase in these systems for CO oxidation.

The above reasoning is further supported by the intensity ratios of the two reduction peaks. Derived from the low intensity of the first reduction peak and the higher intensity of the second reduction peak, it appears that for a low Cu content most of the Cu mainly exists as Cu^{2+} inside the bulk of the support. When the Cu content is increased, however, the intensity of the first reduction peak also increases, meaning that more finely dispersed Cu species are then present on the surface of the support, which was previously also shown by XPS.

When the Cu dopant concentration was increased from 2.77 mol% to 5.55 mol%, a notable shift of the reduction peaks to lower temperatures was observed. A similar observation was also reported in other studies on copper doped CeO_2-based mixed oxides [168,170,171]. This observation can be explained by the induced lattice strain and the creation of more defects in the fluorite lattice for a higher dopant concentration, leading to an enhanced oxygen mobility in the support. In addition, the formation of elongated metal-oxygen bonds upon the doping also provides more labile oxygen species, thereby allowing the reduction of the support to occur at much lower temperatures along with the reduction of Cu^{2+} and Cu^+ ions. The simultaneous reduction of the support and the Cu ions is confirmed by the H_2/Cu ratios, which are summarized in Table 2.5. In a TPR experiment for bulk CuO, this ratio would be equal to 1. However, as we observed H_2/Cu ratios being larger than the stoichiometric value of 1, part of the support must also be reduced at the same time due to a synergistic effect taking place between the transition metal and CeO_2 [168].

Table 2.5: H_2 consumption values and H_2/Cu ratios for the Cu-doped ceria-zirconia samples.

Sample	H_2 consumption (mmol g^{-1})	H_2/Cu ratio
CeZrO$_4$	0.92	/
2CuCZ	0.95	4.97
5CuCZ	1.12	2.90
11CuCZ	1.27	1.60

The fact that the H_2/Cu ratios decrease when the Cu content increases indicates that the interaction between CeO_2 and Cu becomes less effective. Zhu et al. found H_2/Cu ratios smaller than 1 for CeO_2 doped with 20 and 30 mol% Cu, and they concluded that large CuO crystallites were most likely formed that might hinder the reduction of the support's surface [168]. The H_2/Cu ratio for 11CuCZ was still larger than 1 in our case, suggesting that no bulk CuO phase was formed and that Cu is still strongly interacting with the support. However, no shift of the reduction peaks to lower temperatures was observed for 11CuCZ. This might indicate that maximum oxygen mobility in the support was reached for a Cu dopant concentration of 5.55 mol%. Furthermore, the shift of the reduction peaks to slightly higher temperatures when the Cu content is increased from 5.55 mol% to 11.11 mol% also indicates that the Cu is now less strongly interacting with the support. This result is consistent with the previous XPS data, which showed that more Cu ions segregated to the surface for 11CuCZ than for 2CuCZ and 5CuCZ.

Compared to other studies, the Cu reduction peaks in our case seem to be substantially more separated from each other. This could be another indication that strongly stabilized metal ions can be obtained with the sol-gel method used in this study. Finally, it was reasoned that the

reduction now occurring over a higher temperature range could be a beneficial feature of these systems for certain catalytic applications.
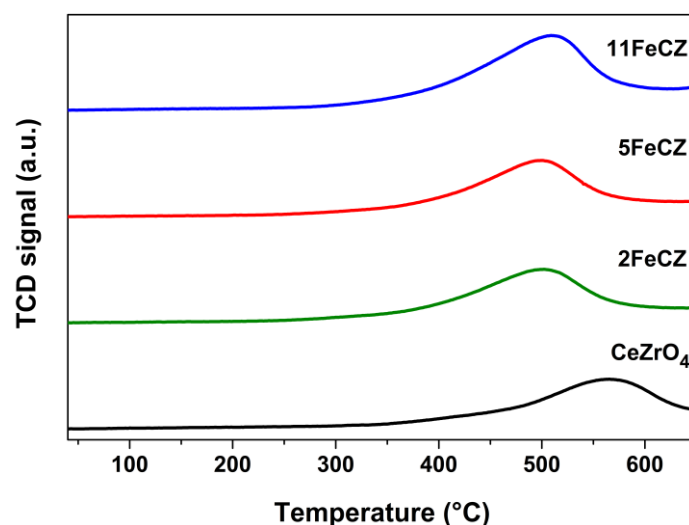
Figure 2.23: H_2-TPR profiles of ceria-zirconia and Fe-doped ceria-zirconia samples.

In contrast to the Cu-doped samples, only a small shift of the reduction peak of pure $CeZrO_4$ (565 °C) to a lower temperature (~ 500°C) was observed for the Fe-doped samples in Figure 2.23. Furthermore, increasing the Fe content did not promoted the reducibility of the catalyst. In general, a stepwise reduction profile is observed for pure Fe_2O_3, with a first reduction peak at lower temperatures ascribed to the reduction of Fe_2O_3 to Fe_3O_4, and a second reduction peak at higher temperatures typically assigned to the reduction of Fe_3O_4 to Fe^0 [172]. However, since no free FeO_x species are present in 2FeCZ, 5FeCZ and 11FeCZ, as evidenced by XRD and UV-Vis spectroscopy, the reduction peaks observed at around 500 °C most likely correspond to the reduction of surface Ce^{4+} to Ce^{3+}. Indeed, it was previously reported that Fe^{3+} incorporated in the CeO_2 lattice activates the surface oxygens and leads to a much easier reduction of the support's surface [173]. Some reduction of highly dispersed Fe^{3+} surface species to Fe^{2+} species might also occur simultaneously with the reduction of the surface oxygen species of the support, which was also proposed in a previous study by Nedyalkova et al. [174]. No clear conclusions could be drawn from the calculated H_2/Fe ratios, shown in Table 2.6.

Table 2.6: H_2 consumption values and H_2/Fe ratios for the Fe-doped ceria-zirconia samples.

Sample	H_2 consumption (mmol g^{-1})	H_2/Fe ratio for Fe in +3 state
CeZrO₄	0.92	/
2FeCZ	0.94	4.92
5FeCZ	0.93	2.40
11FeCZ	1.12	1.42

No satisfying explanation could be found for this poor reduction behavior of the xFeCZ samples, but it could be that doping of the ceria-zirconia support with Fe leads to a highly stable

solid solution system for which the lattice is not saturated yet for the dopant concentrations used in this study. In line with this, the absence of a second reduction peak indicates that no segregated Fe oxide phase is formed when the Fe dopant concentration is increased. Moreover, it could be that Fe is trapped too deeply in the bulk of the support. This assumption could explain why the xFeCZ samples exhibit excellent thermal stability as derived from the XRD measurements.
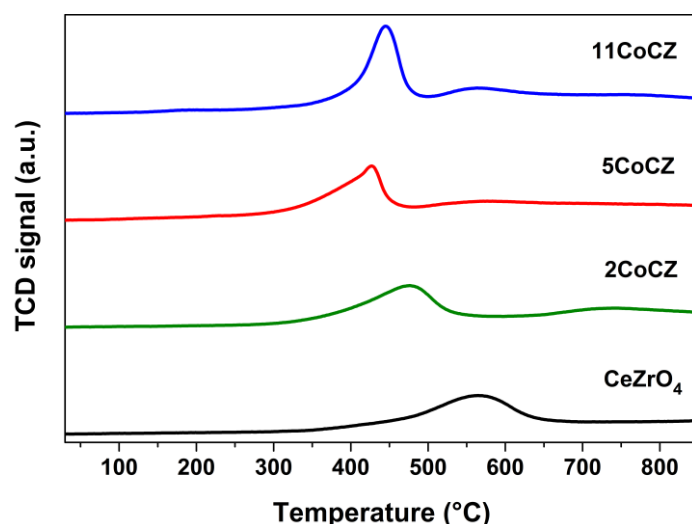
Figure 2.24: H_2-TPR profiles of ceria-zirconia and Co-doped ceria-zirconia samples.

For the Co-doped samples, the reduction peaks at 477 °C, 427 °C and 446 °C for 2CoCZ, 5CoCZ and 11CoCZ, respectively, were attributed to the reduction of Co^{2+} ions and surface oxygen species of the support. The fact that not only Co^{2+} is reduced can be derived from the high H_2/Co ratios in Table 2.7. No shift of the reduction peaks to lower temperatures was observed when the Co content was increased from 5.55 to 11.11 mol%, suggesting that maximum oxygen mobility was reached for 5CoCZ. Consequently, doping the support with additional Co^{2+} ions now no longer promotes the reduction of the catalyst, but it can only further increase the H_2 consumption due to the reduction of more CoO species. This is also confirmed by the H_2 consumption values shown in Table 2.7. The decrease in the H_2/Co ratio might indicate that less of the support is reduced for a higher Co dopant concentration.

Table 2.7: H_2 consumption values and H_2/Co ratios for the Co-doped ceria-zirconia samples.

Sample	H_2 consumption (mmol g^{-1})	H_2/Co ratio
CeZrO4	0.92	/
2CoCZ	1.45	7.59
5CoCZ	1.71	3.56
11CoCZ	1.90	1.86

In Figure 2.24, a second reduction peak of low intensity was also observed at slightly higher temperatures than the first reduction peak. Based on the high H_2 consumption values associated with these peaks, this reduction step cannot be solely related to the reduction of CoO_x species,

but most likely also to a partial reduction of the support. A similar reduction profile was also reported by Wang et al. for Co doped ceria-zirconia, and they also explained the low intensity peak by the reduction of the CZ support [175].

In contrast to our results, other studies have shown the presence of two sharp reduction peaks for similar Co-based systems [127,176]. They ascribed the first peak to the reduction of Co^{3+} to Co^{2+}, as there was clear evidence of Co_3O_4 nanoparticles and clusters being present on the support's surface. Since these species are clearly absent in our case, it can be concluded that a two-step reduction of Co_3O_4 to Co^0, involving CoO as an intermediate, does not apply here for the xCoCZ samples. Furthermore, the satellite feature in the XPS Co2p spectra indicated that Co is mainly present in the Co^{2+} chemical state. Furthermore, no segregated Co_3O_4 phases were detected by XRD and TEM analysis, confirming that the first reduction peak most likely corresponds to reduction of Co^{2+}, and not Co^{3+}.
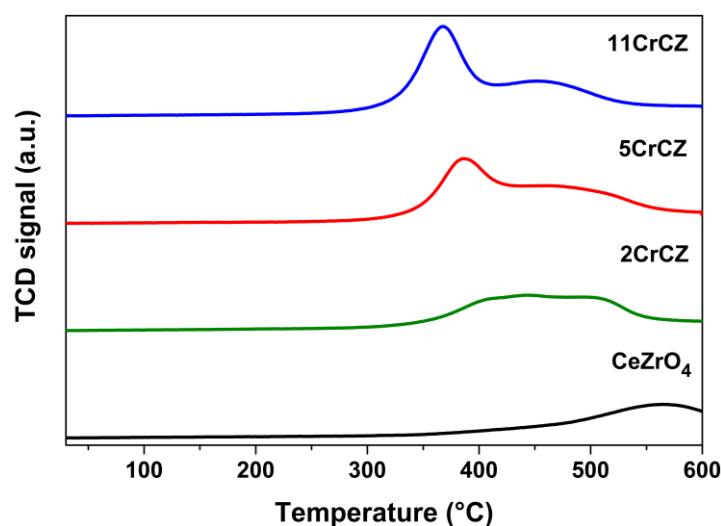
Figure 2.25: H_2-TPR profiles of ceria-zirconia and Cr-doped ceria-zirconia samples.

Just as in the case of the xCuCZ and xCoCZ samples, two reductions peaks could be observed for the xCrCZ samples, as shown in Figure 2.25 These peaks are also located at much lower temperatures compared to the single reduction peak of $CeZrO_4$. The decrease in the reduction onset indicates the formation of defects and more labile oxygen ions after doping of the ceria-zirconia support with Cr. Furthermore, a synergistic interaction between the dopant and the reducible support may promote the reduction of the homogeneously distributed dopant species at much lower temperatures compared to the reduction of the parent oxide.

Table 2.8: H_2 consumption values and H_2/Cr ratios for the Cr-doped ceria-zirconia samples.

Sample	H_2 consumption (mmol g^{-1})	H_2/Cr ratio for Cr in +3 state
CeZrO$_4$	0.92	/
2CrCZ	0.98	5.21
5CrCZ	1.26	3.35
11CrCZ	1.56	2.08

For higher Cr dopant concentrations, the intensity of the first reduction peak increases and the peak shifts to lower temperatures (from 430 °C for 2CrCZ to 366 °C for 11CrCZ). This peak may be attributed to the reduction of Cr^{6+} species to Cr^{3+} species along with the reduction of surface oxygen species of the support, as can also be derived from the H_2/Cr ratios shown in Table 2.8 [177–179]. The presence of Cr^{6+} species was previously demonstrated by XPS. The broad peak at a slightly higher temperature correspond to the reduction of highly dispersed Cr^{3+} species and surface oxygen species of the reducible support [177,179].
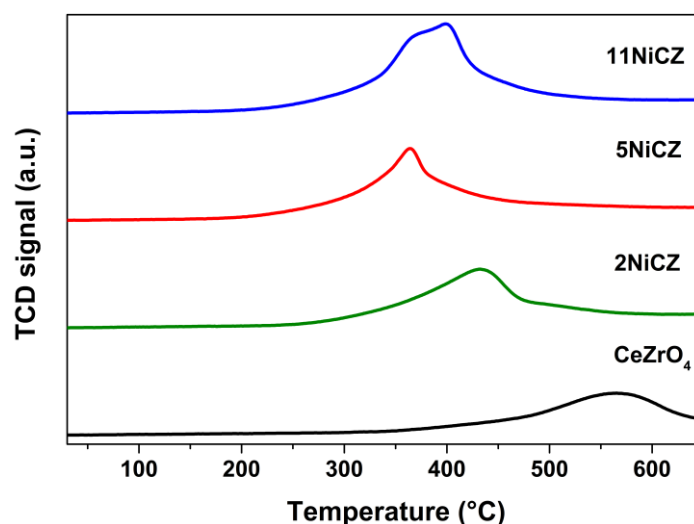
Figure 2.26: H_2-TPR profiles of ceria-zirconia and Ni-doped ceria-zirconia samples.

The reduction profiles of the Ni-doped samples are shown in Figure 2.26. A similar change in the reduction behavior as for the Cu- and Co-doped samples was observed when CeZrO$_4$ was doped with a higher Ni^{2+} concentration. In particular, increasing the dopant concentration from 2.77 mol% to 5.55 mol% caused a significant shift of the reduction peak to lower temperatures, but no such shift was observed when the dopant concentration was further increased to 11.11 mol%. This observation indicates that maximum oxygen mobility in the solid solution system was reached for 5NiCZ. Furthermore, the TPR-profiles of 2NiCZ and 5NiCZ rule out that a segregated NiO phase has been formed because of the presence of a single reduction peak in the profiles. Usually, at least two reduction peaks are observed for CeO$_2$-based oxides impregnated with Ni due to the formation of a bulk NiO phase at higher Ni loadings [162]. The single reduction peak observed in this study indicates that a strong metal-support interaction might be present between Ni and ceria-zirconia. The formation of a nearly perfect homogeneous

solid solution, as evidenced by XPS analysis, further confirms this assumption. This is also in line with XRD and UV-Vis measurements, which also excluded the formation of a free NiO phase for the Ni-doped samples calcined at 500 °C.

Table 2.9: H_2 consumption values and H_2/Ni ratios for the Ni-doped ceria-zirconia samples.

Sample	H_2 consumption (mmol g^{-1})	H_2/Ni ratio
CeZrO$_4$	0.92	/
2NiCZ	1.07	5.64
5NiCZ	0.90	2.37
11NiCZ	1.53	1.93

It should be noted, however, that a shoulder is visible for the reduction peak of 11NiCZ, pointing to the reduction of Ni^{2+} species that are interacting less strongly with the reducible support. The single peak in the TPR-profiles of 2NiCZ and 5NiCZ can be assigned to the simultaneous reduction of the support's surface and Ni^{2+} ions to metallic Ni^0. This can be derived from H_2/Ni ratios which were found to be larger than the stoichiometric value of 1, as shown in Table 2.9. No explanation could be found for the lower H_2 consumption value recorded for 5NiCZ compared to 2NiCZ.
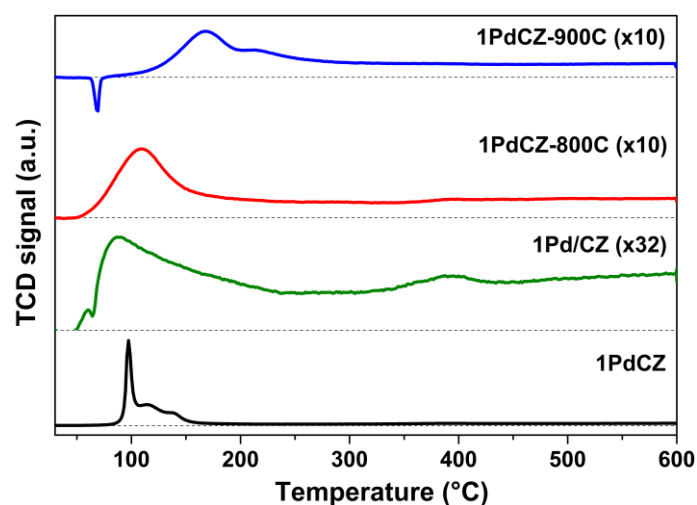
Figure 2.27: H_2-TPR profiles of Pd-based ceria-zirconia samples.

Figure 2.27 shows the H_2-TPR profiles of one-step synthesized 1PdCZ and impregnated 1Pd/CZ catalysts up to 600 °C. It has been reported in literature that the low-temperature reducibility can be significantly enhanced when noble metals such as Pt, Rh or Pd are added to the catalyst formulation [49,165,180]. As shown in Figure 2.27, the shift of the reduction peak of pure CeZrO$_4$ from 565 °C to temperatures as low as 100 °C after doping or impregnating the support with Pd is in line with these studies. The lattice distortion and the formation of oxide defects induced after doping with Pd enhances the migration of oxide ions through the lattice, therefore facilitating the reduction of Ce^{4+}. Furthermore, the reduction of the support could also be facilitated in the presence of a noble metal due to the induced hydrogen spillover effect. This

effect involves the activation of hydrogen by the noble metal and the consequent migration to the support, leading to more facile reduction of the support at lower temperatures.

Table 2.10: H_2 consumption values and H_2/Pd ratios for the Pd-based ceria-zirconia samples.

Sample	H_2 consumption (mmol g^{-1})	H_2/Pd ratio
CeZrO$_4$	0.92	/
1PdCZ	0.67	7.11
1PdCZ-800C	0.38	4.01
1Pd/CZ	0.14	1.52

Table 2.10 shows that a significantly higher H_2/Pd ratio was found for 1PdCZ (7.11) than for 1Pd/CZ (1.52). This result indicates the enhanced reduction properties of Pd-doped samples compared to Pd-impregnated samples. In 2009, Baidya et al. also reported an exceptionally high H_2/Pd ratio for Pd-doped $Ce_{1-x}Ti_xO_2$ (7.5) [181]. This result is not only related to the creation of more defects and labile oxygen ions when Pd is incorporated in the CeO_2 lattice, but also due to the more intimate Pd-Ce contact that can be achieved after doping the support. In combination with the well-known hydrogen spillover effect that is typically observed for noble metals, this could lead to a more efficient reduction of the support material at low temperatures. The less efficient reduction of the support for Pd-impregnated samples is also clear from the broad reduction peak centered at 400 °C, which indicates that the surface of the support could not be fully reduced at temperatures below 100 °C. The observation of two reduction peaks for 1Pd/CZ below 100 °C could also suggest that more than one type of surface Pd species are present, which is typically the case for Pd-impregnated samples.

Calcination of 1PdCZ at 800 °C shifted the low-temperature reduction peak to a slightly higher temperature (107 °C) and lowered the amount of H_2 consumed, which could be attributed to the sintering of the support and less homogeneously distributed Pd^{2+} in the fluorite lattice and on the surface of ceria-zirconia. The lower specific surface area measured for 1PdCZ-800C (12 m^2/g) compared to that of 1PdCZ (71 m^2/g) confirms that sintering of the support has occurred. Nevertheless, the H_2/Pd ratio for 1PdCZ-800C was still found to be higher than for 1Pd/CZ. This is consistent with the high binding energy of Pd in 1PdCZ-800C measured by XPS, indicating that Pd is still strongly associated with the support after the calcination at elevated temperatures.

The negative reduction peak observed for 1PdCZ-900C indicates that Pd metal is formed after calcination at 900 °C, which is in agreement with the observation of the (111) reflection of Pd metal in the XRD pattern of this catalyst. More specifically, the negative reduction peak means that hydrogen is released rather than consumed, which is only possible due to the presence of Pd metal that is able to absorb and store hydrogen in its lattice, forming palladium hydride (PdH_x), before decomposing and releasing hydrogen back into the atmosphere at higher temperatures [182]. Furthermore, the shift of the positive reduction peak to an even higher temperature (167 °C) compared to 1PdCZ and 1PdCZ-800C suggests severe sintering of the support and the noble metal phase, hence further deteriorating the reduction properties of the catalyst.

3.5 Extended X-ray Absorption Fine Structure (EXAFS) spectroscopy

EXAFS studies were performed to reveal the local structure around the transition metal ions in some of the Fe-, Cu-, Co- and Pd-based ceria-zirconia samples. The results of these measurements are shown in Figure 2.28.
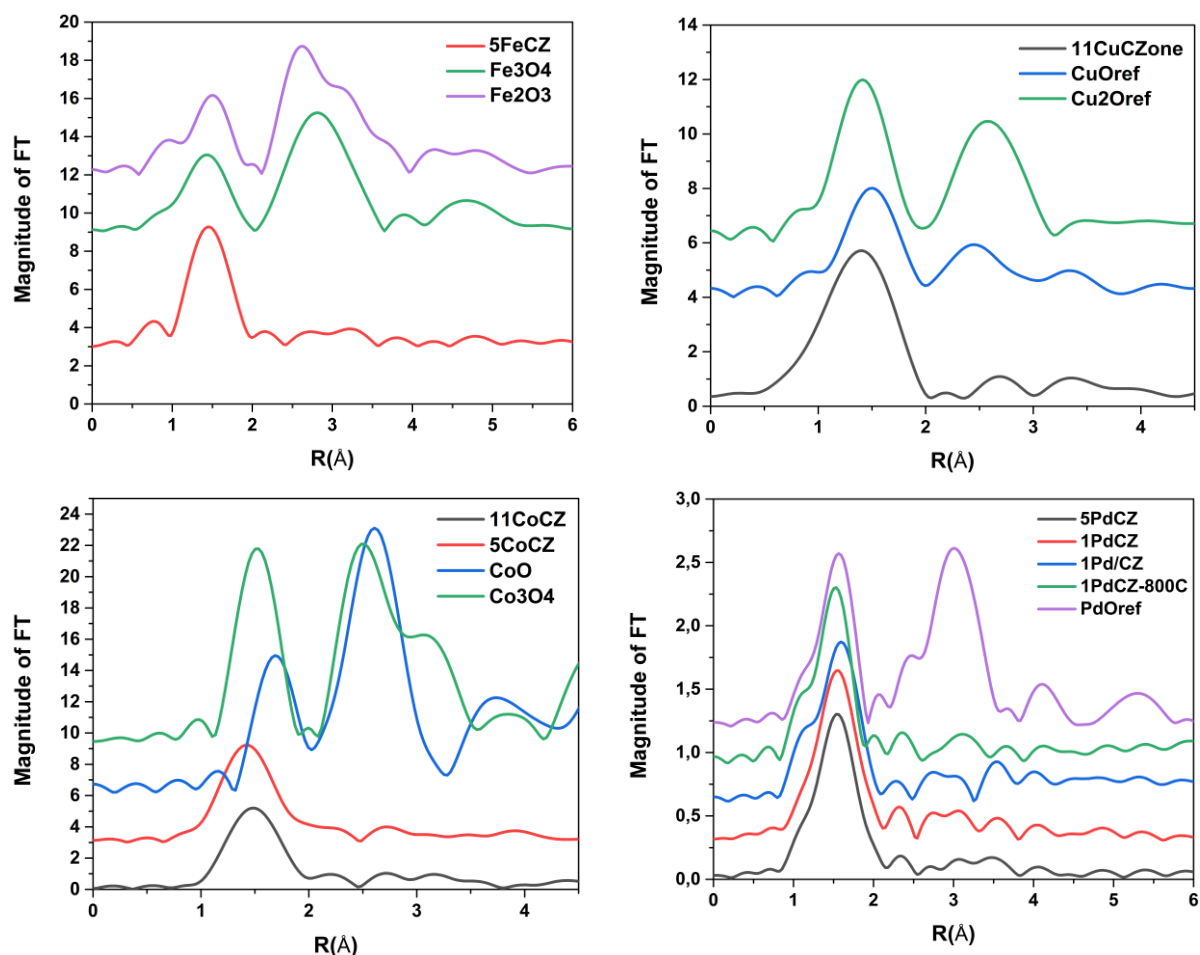
Figure 2.28: EXAFS spectra of Fe-, Cu-, Co- and Pd-doped ceria-zirconia samples prepared by the sol-gel method. The EXAFS spectrum of Pd-impregnated ceria-zirconia (1Pd/CZ) was also measured for comparison with one-step synthesized 1PdCZ.

The EXAFS spectra of the sol-gel synthesized samples showed only one significant peak around 1.5 Å, corresponding to the M-O (M = transition metal) interatomic distance. The peaks visible in the reference samples at larger bond distances were largely absent in the transition metal-doped ceria-zirconia samples. The absence of these higher coordination shells indicates that isolated species were obtained for the sol-gel prepared ceria-zirconia samples. Since the EXAFS data represents only the average structure around the absorbing ions, it is not clear whether single-atomic species are also present on the surface of the ceria-zirconia supports. Nevertheless, these data strongly suggest that solid solution type systems can be obtained via the polymer-assisted sol-gel method used in this study. This is also confirmed by the absence

of a higher coordination shell for 1PdCZ-800C, while typically Pd metal or bulk Pd oxide is formed at such high calcination temperatures [78,79].

The results shown in Figure 2.28 were found to be consistent with the previous XRD, UV-Vis and TEM analyses, where it was shown that segregated bulk transition metal oxide phases are absent in our samples. Hence, it can be concluded that the transition metal ions in the substituted Ce^{4+} sites are effectively stabilized by the support due to the formation of strong covalent M-O bonds after the doping of the ceria-zirconia oxide. The extent of the metal-support interaction largely depends on the support material that was selected and the synthesis method applied. For example, the EXAFS spectra reported by Priolkar et al. clearly show more pronounced Pd metal and Pd bulk oxide peaks for Pd-doped ceria prepared via a combustion technique [183]. Furthermore, the formation of such undesirable species is also more favored for transition metal-impregnated ceria-based supports. The EXAFS spectrum of 1Pd/CZ in our case, however, only shows relatively low-intensity peaks at the higher interatomic distances, indicating that the sol-gel synthesized ceria-zirconia support is also efficient in dispersing the Pd on its surface and forming a strong metal-support interaction.

4. Conclusions

A series of nanostructured ceria-zirconia solid solutions with multiple transition metal dopants (Fe, Cu, Co, Ni, Cr and Pd) were synthesized using a one-step polymer-assisted sol-gel method. XRD analysis showed that the solid solutions exhibited remarkably high thermal stability (at least 800 °C). In particular, Cr-doped ceria-zirconia displayed the highest thermal stability, as no segregated bulk Cr oxide phases could be detected by XRD for a dopant concentration of 11.11 mol% and a calcination temperature as high as 800 °C. UV-Vis measurements indicated the presence of a segregated Cr_2O_3 phase, which most likely exists in the form of small clusters finely dispersed on the surface of the support. This was in line with XPS measurements, which showed that the transition metal dopants can easily segregate to the surface of the support.

XRD, UV-Vis and XPS measurements further showed that no segregated bulk PdO or Pd^0 was present in 1PdCZ, while previous studies have demonstrated that PdO in ceria-based materials decomposes at this temperature into reduced Pd, which negatively affects the catalytic activity. This result further proves that exceptionally stable ceria-zirconia solid solution systems can be synthesized with the sol-gel method used in this study. Furthermore, the dopants were found to be in the form of isolated species, as evidenced by EXAFS. The presence of only the first Pd-O shell in the r-space EXAFS spectrum of 1PdCZ-800C rules out the presence of bulk PdO or Pd^0 phases. This in turn suggests that Pd is highly dispersed and has an isolated nature, which exhibits a remarkable stability of the active phase even after harsh 800 °C calcination relevant for automotive gas exhaust clean-up conditions.

Finally, the reducibility of the solid solutions was investigated by H_2-TPR analysis. It was found that using a dopant concentration of more than 5.55 mol% often did not result in an improved intrinsic reducibility of the support. Taking into account that CeO_2 was already doped with a high amount of Zr^{4+} ions, it is plausible that maximum oxygen mobility in the crystal lattice

can be reached for a dopant concentration around 5.55 mol%. The Pd-based samples displayed the lowest reduction onset temperature (below 100 °C), while Pd-doped ceria-zirconia showed enhanced reduction properties compared to Pd-impregnated ceria-zirconia. This was explained by the presence of more defects in the crystal lattice of the doped sample that could increase the oxygen mobility significantly. It is assumed that a more intimate contact between Pd and the support for 1PdCZ could also play a role in the abovementioned redox properties. In combination with the hydrogen spillover effect that is typically observed for noble metal-based catalysts, the intimate Pd-Ce contact could then lead to a much more efficient reduction of the support at low temperatures. This is of a great importance not only for the automotive exhaust catalysis, but also for the wide range of chemical processes catalyzed by the reducible oxides supported systems.

Chapter 3

Catalytic performance of sol-gel prepared ceria-zirconia mixed oxides for the CO + NO and CO + O2 reactions

1. Introduction

Nitrogen oxides (NO_x) and carbon monoxide (CO) are two main pollutants emitted from gasoline-fueled vehicles, and their emission into the atmosphere may cause significant adverse effects on human health and the environment. According to the World Health Organization, NO_x air pollution has contributed to the premature death of around 2.6 million people in 2012 [184]. Furthermore, studies have shown that nitric oxide (NO) and nitrogen dioxide (NO_2) pose a significant threat to the environment, as they are both major sources of acid rain [185]. Since around 40% of the total NO_x emissions originates from road transport according to the European Environment Agency, new three-way catalytic converters (TWCs) that are highly active for the reduction of NO_x need to be developed [186]. The need for improved catalytic converters is also clear from the fact that the NO_x emission from vehicles is at least six times higher than the actual emission limit for these toxic compounds [187]. Consequently, the European Commission decided to introduce a real driving emission (RDE) test which is more stringent than the traditional laboratory test, starting from September 2017 [188]. The new RDE test allows NO_x emission amounts that are 2.1 times higher than the current Euro 6 NO_x emission standard (0.08 g/km) [188]. In order to meet this standard, control of the CO + NO reaction is crucial, since both toxic NO and CO can be removed simultaneously from the exhaust gas after the reduction of NO by CO (or the oxidation of CO by NO):

$$CO + NO \rightarrow CO_2 + \tfrac{1}{2} N_2$$
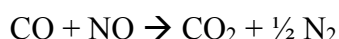
Since a considerable portion of the total NO_x amount is emitted during the cold-start of the engine, the catalytic converter should not only show high activity, but also high selectivity to harmless N_2. In particular, the high selectivity is needed in order to prevent the emission of N_2O, which is prevalently formed at low temperatures during the cold-start conditions [24,189]:

$$CO + 2\,NO \rightarrow CO_2 + N_2O$$
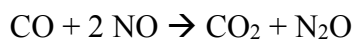
Due to the fact that N_2O has a global warming potential of approximately 310 times higher than CO_2 , and as studies have shown that it is partly responsible for stratospheric ozone layer depletion, its emission into the atmosphere should be limited to the extent possible [25,26].

In 2001, Granger et al. showed that the activity for the CO + NO reaction could be significantly increased when promoting the CeO_2 support with ZrO_2 due to the enhanced OSC or redox properties obtained after forming a solid solution [190]. The oxygen vacancies in the support

were assumed to play an important role in the dissociation of NO and N_2O to N_2. Furthermore, other studies have demonstrated the importance of noble metals for the CO + NO reaction, as it was shown that N_2 is preferentially formed on noble metal active sites [191–193]. The structure sensitivity of the CO + NO reaction has been shown multiple times in literature, and therefore a significant effect of the particle size of the support and Pd on the catalytic activity can be expected [194]. However, some contradictory results on this effect have been reported by several research groups. For example, Pisanu et al. observed an increased catalytic activity for the NO dissociation reaction on small Pd particles supported on Al_2O_3 [195], while Rainer et al. demonstrated that NO dissociation was favored on Pd/Al_2O_3 with large Pd particles [196]. Furthermore, contradictory results also exist for the effect of the oxidation state of the noble metal on the activity. In 2005, Granger et al. showed that reduced noble metal sites are responsible for the N_2 formation [192]. In line with this, other studies found that undesired N_2O formation mainly involves oxidized noble metal sites [197,198]. Conversely, it was also shown in the literature that the reaction rate of the CO + NO reaction increased for catalysts that were pretreated in an oxidizing environment, while the reaction rate was significantly lower for the same catalysts pretreated in a reducing environment [199].

In recent years, single Pd-based catalysts have attracted much attention due to the lower cost and higher availability of Pd compared to Pt and Rh [200]. The combination of Pd with a CeO_2-based oxide was found to be highly active for the oxidation of CO and HCs [20,201]. The Pd-Ce interface also seems to be a key requisite for the facilitated N-O bond dissociation in these systems. Rao et al. explained this observation by the formation of an oxygen vacancy at the Pd-Ce contact that can assist in the decomposition of N_2O to N_2 [202]. The presence of an oxygen vacancy in close proximity to Pd was also further confirmed by EXAFS studies [183]. Although an intimate Pd-Ce contact seems to favor the reduction of NO_x species in these systems, the overall NO_x conversion is still lower compared to Rh-based systems [203]. Consequently, transitions metals are often introduced in the TWC formulation to promote specific reactions occurring over the catalytic converter. However, despite many attempts to replace Pd, Pt and Rh by a cheaper transition metal, the noble metal remains an essential component in the TWC formulation to obtain high conversion efficiencies for all the main pollutants (CO, NO and HC) emitted by gasoline vehicles. Therefore, many research groups have been combining Pd with various transition metals and with different loadings to optimize the conversion efficiencies for CO, NO and HCs. The result is often the formation of an alloy between Pd and the transition metal which shows an improved catalytic activity compared to Pd-only catalysts. In literature, alloy formation of Pd with Cr [204,205], Cu [206–208], Mo [209] and Mn [210] has been observed. In the case of Cu, EXAFS studies have shown that a Pd-Cu alloy was indeed formed in bimetallic catalysts [211,212]. Theoretical studies have been trying to explain the promoted CO activation and NO dissociation after alloying, and this was attributed to a perturbation in the valence electron density of Pd that is produced by a charge injection from the transition metal into one of the Pd sub-bands [213]. A more recent theoretical study also concluded that the reaction barrier for NO dissociation can be substantially lowered after alloying Pd with a transition metal [214].

In this chapter, the NO reduction and CO oxidation activity of various sol-gel synthesized ceria-zirconia based catalysts was examined. Non-noble metal and Pd-based catalysts were

56

synthesized using different transition metal dopants, and the loadings were optimized in order to achieve high NO and CO conversion efficiencies. Further, the influence of the Pd chemical state on the reduction of NO and oxidation of CO was investigated by either doping or impregnating the ceria-zirconia supports with the noble metal. Finally, multiple characterization techniques (XPS, H_2-TPR and DRIFTS) were employed to identify the active phases in the CO + NO and CO + O_2 catalytic reactions. These results are analyzed first, followed by a detailed discussion of the observed catalytic activity trends. XRD and TEM analysis of some of the Pd-based catalyst are included in the Supporting Information.

2. Experimental

2.1 Materials and synthesis

Ceria-zirconia support catalysts ($Ce_{0.5}Zr_{0.5}O_2$ or $CeZrO_4$) were synthesized via a polymer-assisted sol-gel method. $Ce(NO_3)_3.6H_2O$ (Alfa Aesar, 99.99%) and $ZrOCl_2.8H_2O$ (Alfa Aesar, 99.9% and Sigma Aldrich, 98%) were used as starting materials, while absolute ethanol (Biosolve, Extra dry, min. 99.9%) was used as the solvent. Poly(ethylene glycol)-block-poly(propylene glycol)-block-poly(ethylene glycol) with an average molecular weight of ~5800 (PEG-PPG-PEG 5800, Sigma-Aldrich) was used as a chelating agent. Ethanol solution (15 ml) of $Ce(NO_3)_3.6H_2O$ (1.736 g), $ZrOCl_2.8H_2O$ (1.288 g) and PEG-PPG-PEG 4400 (0.8 g) was prepared and stirred for approximately 2 h at room temperature until a transparent precursor sol was obtained. Next, the sol was aged at 40 °C for approximately 3 days in an oven with a beaker of water placed inside in order to keep sufficient partial pressure of water vapors. Once the rubber-like texture of gel has been employed, subsequent drying overnight at 110 °C in air was performed. After drying, the precipitate was crushed into a fine powder and calcined in air at 500 °C with a heating rate of 1 °C/min and a dwelling time of 4 hours. A schematic overview of the synthesis procedure is shown in Figure 3.1.

Figure 3.1: Flowchart for the preparation of $CeZrO_4$ via a polymer-assisted sol-gel method.

Doped ceria-zirconia catalysts were also prepared using different transition metals with various metal loadings. The same synthesis procedure as for the bare $Ce_{0.5}Zr_{0.5}O_2$ was adopted, simply adding transition metal precursors in the first step of the synthesis procedure. The aging time varied from 3 to 5 days, depending on the dopant and the loading chosen. All of the samples were calcined at 500 and 800 °C to investigate their thermal stability, while a temperature of 900 °C was also once used. Transition metals such as Cu, Fe, Co, Cr, Ni and Pd were chosen as dopants. Following precursors of abovementioned metals were used: $Cu(NO_3)_2.3H_2O$

(Sigma Aldrich, 99-104%), $Fe(NO_3)_3.9H_2O$ (Sigma Aldrich, $\geq$ 98%), $Co(NO_3)_2.6H_2O$ (Emsure, $\geq$ 99%), $Cr(NO_3)_3.9H_2O$ (Alfa Aesar, 98.5%), $Ni(NO_3)_2.6H_2O$ (Sigma Aldrich, $\geq$ 97%) and $Pd(acac)_2$ (acac = acetylacetonate, Sigma Aldrich, 99%). The metal loadings were kept as 2.77, 5.55 and 11.11 mol%, while for palladium 1 and 5 wt.% were used. The obtained catalysts were labeled as xMCZ, with x taking values of 1, 2, 5 and 11, standing for metal loadings of respectively 1 wt.%, 2.77 mol%, 5.55 mol% or 5 wt.% (in case of Pd) and 11.11 mol%., M reflecting the dopant used, and CZ referring to ceria-zirconia. For example, a sample doped with 2.77 mol% Cr and 1 wt.% Pd is denoted as 1Pd2CrCZ.

Palladium (1 wt%) was deposited on both bare and doped ceria-zirconia supports via a conventional wet impregnation method. $Pd(NO_3)_2.2H_2O$ (Sigma Aldrich, 40% Pd basis) was dissolved with demineralized water in a small snap cap vial and the solution was subsequently poured onto the support. After vigorously stirring the dispersion for approximately 30 min, the mixture was heated to 80 °C to slowly evaporate the water while stirring. The resulting solid was dried at 110 °C and crushed to a fine powder, which was finally calcined in air at 300 °C with a heating rate of 5 °C/min and a dwelling time of 3 h. The same procedure was used for depositing chromium (2.77 mol% and 5.55 mol%) on the support. The ceria-zirconia supports impregnated with Pd were denoted as 1Pd/xMCZ (M = transition metal dopant, x = mol% used for doping), while 1PdCZ supports impregnated with Cr were denoted as 2Cr/1PdCZ and 5Cr/1PdCZ.

2.2 Catalyst characterization

X-ray diffraction (XRD)

In this work, X-ray diffraction (XRD) was used to analyze the crystal structure and thermal stability of the ceria-zirconia mixed oxides. A Bruker D2 Phaser powder diffraction system equipped with a copper anode and a thin nickel foil filter was used. The latter removes the Kβ radiation of the copper X-ray source, allowing the Cu Kα radiation (λ = 1.5406 Å) to pass. The XRD patterns were recorded in a 2θ range of 20° to 80° with a step size of 0.02° and a time per step of 0.5s. Samples calcined at 800 °C and 900 °C were recorded with 1s per step. A 0.6 mm divergence slit was used to limit the beam divergence of the source, while an anti-scatter screen with a sample-screen distance of 0.5 mm was used to block scattered radiation at low angles. The samples were rotated with a constant speed of 30 rot/min during the XRD measurements.

Transmission electron microscopy (TEM)

TEM measurements were performed on a FEI Tecnai 20 transmission electron microscope with an electron acceleration voltage of 200 kV and a LaB_6 filament. A few milligrams of each sample were sonicated in pure ethanol (Biosolve, Extra dry, 99.9%), and a few drops of the resulting dispersion were dripped over a 200 mesh Cu TEM grid with a holey carbon support film. Prior to imaging, the supported samples were left in an oven at 40 °C overnight to remove residual ethanol.

X-ray photoelectron spectroscopy (XPS)

XPS measurements were carried out with a Thermo Scientific K-Alpha, equipped with a monochromatic small-spot X-ray source and a 180° double focusing hemispherical analyzer with a 128-channel detector. Spectra were obtained using an aluminium anode (Al Kα = 1486.6 eV) operating at 72W and a spot size of 400 m. Survey scans were measured at a constant pass energy of 200 eV and region scans at 50 eV. The background pressure was 2×10^{-8} mbar and during measurement 4×10^{-7} mbar Argon because of charge compensation by the dual-beam low energy electron / Arion source. Data analysis was performed using CasaXPS software. The binding energy was corrected for surface charging by taking the Ce3d$_{3/2}$ peak as a reference at 916.7 eV.

Hydrogen-Temperature Programmed Reduction (H$_2$-TPR)

The reducibility of the catalysts was determined by hydrogen-temperature programmed reduction (H$_2$-TPR) using a Micromeritics AutoChem II 2920 equipped with a computer-controlled oven and a thermal conductivity detector (TCD). Approximately 100 mg of each sample were transferred into a U-shaped quartz reactor tube and fixed between two quartz wool plugs. Before the H$_2$-TPR experiment was carried out, the samples were first pretreated *in situ* to remove moisture and impurities. The pretreatment involved calcining the samples in a 50 ml/min 5% O$_2$/He flow at 300 °C using a heating rate of 10 °C/min, after which they were subsequently cooled to room temperature at a cooling rate of 35 °C/min.

The H$_2$-TPR experiment is carried out by using a H$_2$ flow, and the reduction process of the oxidized species occurs under temperature programmed conditions by increasing the temperature with a constant heating rate. For reduction of the samples, a 50 ml/min flow of 4% H$_2$/N$_2$ was used and the temperature was ramped to 600-800 °C at a rate of 10 °C/min. The TCD signal was normalized by the weight of the sample.

Diffuse reflectance infrared Fourier transform spectroscopy (DRIFTS)

DRIFTS analysis was carried out using a home-built in-situ setup employing a Bruker Vertex 70v instrument with a MCT detector for the collection of the FTIR spectra. Approximately 20 mg of each sample were put as a powder in the Harrick-design DRIFTS *in-situ* cell. Next, the samples were pretreated by calcining them *in-situ* at 300 °C in O$_2$ (25 mbar), followed by cooling down to room temperature (also in O$_2$). Finally, CO + O$_2$ was flown with the rate of 2 ml/min (2 mbar overall pressure in the cell), and the series of spectra were recorded (100 scans each). The last spectrum corresponds to the 8 minutes of CO + O$_2$ flow.

N$_2$ physisorption

The surface area of the ceria-zirconia mixed oxides was determined via N$_2$ physisorption measurements at -196 °C on a Micromeritics Tristar II 3020 instrument. Approximately 150 mg of the sample was transferred in a glass sample tube, followed by pretreatment overnight at 150 °C under a continuous N$_2$ flow to remove moisture and impurities. The Brunauer-Emmet-Teller (BET) model was applied for determining the surface area from the adsorption isotherms obtained by computer controlled gravimetric analysis.

Inductive Coupled Plasma- Optical Emission Spectrometry (ICP-OES)

The Pd, Cr and Fe loading was determined using a Spectroblue, AMETEK Inc. ICP-OES instrument. A solution of concentrated H_2SO_4 (95-98%, 30 ml) and $(NH_4)_2SO_4$ (20 g) was prepared for dissolving the ceria-zirconia-based samples. In particular, 5 ml of this solution was used for dissolving 25 mg of each sample. The mixture was stirred and heated at 230 °C until the sample was fully solubilized. The clear, yellow solution was then subsequently cooled down and carefully diluted with demineralized water in a 50 ml volumetric flask. Next, 5 ml of this solution was further diluted (10 times) for the analysis. Calibration solutions with the same matrix as the diluted sample solutions were also prepared, and the ICP-OES analysis was conducted *in duplo* to verify the reproducibility of the results. The wavelengths used for Pd were 340.458, 324.270 and 229.651 nm. The wavelengths used for Cr were 267.716 and 205.618 nm, and for Fe these were 259.941 and 238.204 nm.

2.3 Catalytic activity measurements

The catalytic activity of the samples was measured for the $CO + O_2$ and $CO + NO$ reactions. The measurements were performed in a high-throughput setup equipped with ten parallel flow reactors. The samples were pressed, crushed and sieved to a fraction between 125 and 250 μm. 50 mg of the sieved fractions were then mixed and diluted with 200 mg of inert SiC of the same sieved fraction. Then the mixtures were subsequently placed between two quartz wool plugs inside quartz tube reactors. A reactor containing 250 mg of the inert SiC was also prepared as a reference. Before the reaction, the catalysts were first pretreated by calcining them *in situ* in a 25/75 (v/v) O_2/He flow, with a total flow of 50 ml/min STP (standard temperature and pressure) for each reactor. After calcining the catalysts up to 300 °C with a heating rate of 10 °C/min and a dwelling time of 2 h, the reactors were cooled down to room temperature in the same flow mixture. For the $CO + O_2$ reaction the volumetric composition of the feed mixture was 1% CO and 1% O_2 balanced with He. For the $CO + NO$ reaction the volumetric composition of the feed mixture was 1% CO and 1% NO balanced with He. Typical temperature profiles of the $CO + O_2$ and $CO + NO$ reaction are shown in Figure 3.2. At each temperature interval, the reaction flow was allowed to stabilize for 10 min before starting the measurement. Each reactor was then measured for 90 s, resulting in 15 minutes of measurement time for all ten reactors. After the first cycle, a second cycle was run in which each reactor was measured once again, leading to two data points for each reactor at every temperature step. The reaction effluents were analyzed with an Interscience Compact gas chromatograph equipped with Plot and Molsieve columns and TCD detectors.
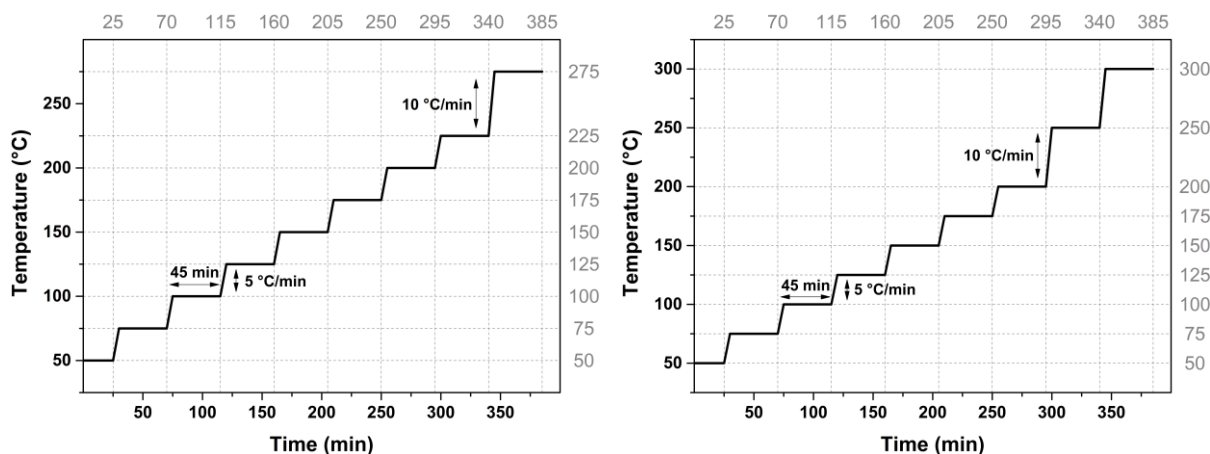
Figure 3.2: Temperature profiles of the CO + NO (left) and CO + O₂ (right) reactions.

Furthermore, the stability of some of the key samples was investigated by probing their CO oxidation and NO reduction activity for three consecutive catalytic activity tests. Before the first and the third run, the samples were pretreated by calcining them *in situ* for 2h at 300 °C in a 25/75 (v/v) O_2/He flow. No pretreatment was used for the second run.

3. Results and discussions

3.1 X-ray Photoelectron Spectroscopy (XPS)

The chemical state of Pd and the composition of the outermost surface layers were investigated by XPS. The XPS results for 1PdCZ and 1Pd/CZ were previously discussed in Chapter 2, as well as the XPS results for the Pd-free catalysts. The XPS results for the Pd-Cr based catalysts are summarized in Table 3.1.

Table 3.1: XPS results for the different Pd-Cr based catalysts.

Sample	Pd binding energy (eV)	mol% Pd (XPS)	mol% Pd (theor.)	mol% Cr (XPS)	mol% Cr (theor.)
1Pd2CrCZ	337.8	2.09	1.44	5.21	2.77
1Pd5CrCZ	337.9	1.75	1.44	8.93	5.55
2Cr/1PdCZ	337.8	1.75	1.44	6.08	2.77
5Cr/1PdCZ	337.6	3.06	1.44	9.97	5.55
1Pd/2CrCZ	337.7	3.12	1.44	3.75	2.77
1Pd/5CrCZ	336.7	11.04	1.44	8.25	5.55
1Pd/11CrCZ	337.2	7.59	1.44	14.13	11.11

Table 3.1 shows that doped Pd displays a higher binding energy than impregnated Pd. The high binding energies ($\geq$ 337.8 eV) for Pd in 1Pd2CrCZ and 1Pd5CrCZ indicate that Pd is atomically dispersed in the form of a highly ionic Pd^{2+} state strongly interacting with the support [147,215]. The molar percentages of Pd detected by XPS were found to be close to the theoretical

concentrations, indicating that Pd is homogeneously distributed in the solid solution system. The high amount of surface Pd detected for 5Cr/1PdCZ (3.06 mol%) could indicate that Cr somehow is able to pull the Pd to the surface.

The higher binding energies recorded for Pd in 1Pd2CrCZ and 1Pd5CrCZ than for Pd in 1PdCZ (337.8 eV) suggest that Cr might affect the Pd charge state through the electronic interaction with Cr within the lattice of the support. This is consistent with the slightly lower binding energies observed for the Pd in 2Cr/1PdCZ and 5Cr/1PdCZ, which are close to typical values for Pd^{2+} highly interacting with the undoped support. Thus, when Cr is deposited onto the surface while part of the Pd is presumably located in the bulk of the support, the synergistic interaction between Cr and Pd becomes less pronounced, leading to similar binding energies for Pd as in 1PdCZ.

Higher Pd mole percentages according to XPS were found for the Pd-impregnated samples. Since Pd resides mostly on the surface after impregnation of the support and due to the fact that XPS is a surface sensitive technique, this appears to be logical. One would expect that for higher Cr doping concentrations the migration of surface Pd to the bulk of the support might become more limited, resulting in a higher amount of the noble metal on the surface of the support. In agreement with our expectations, more surface Pd was found for 1Pd/11CrCZ than for 1Pd/2CrCZ. The binding energy of 337.7 eV indicates that Pd^{2+} is atomically dispersed in 1Pd/2CrCZ, thereby demonstrating the ability of ceria-zirconia to disperse noble metals on its surface with high efficiency. This feature of ceria-zirconia becomes less pronounced when the lattice becomes more distorted, i.e. for higher Cr dopant concentrations. Indeed, the binding energy of 336.7 eV for Pd in 1Pd/5CrCZ suggests the presence of PdO_x 2D clusters in close contact with the CZ support, while the binding energy of 337.2 eV indicates that Pd is in the form of bulk Pd oxide in 1Pd/11CrCZ [147,216]. The presence of sub-nm PdO_x clusters on the surface of 1Pd/5CrCZ might explain why a considerably higher amount of Pd was detected by XPS for this sample compared to 1Pd/2CrCZ, where most of it is atomically dispersed on/in the surface.

For all Pd-Cr based catalysts, higher Cr dopant concentrations compared to the loading were measured by XPS. For the Pd-impregnated catalysts, these concentrations are in line with the values found for the bare xCrCZ supports reported in the previous chapter. For the one-step synthesized 1PdxCrCZ samples, however, the Cr concentrations were found to be slightly higher than for the Pd-impregnated samples. This might be due to an easier segregation of the Cr dopant ions to the surface when the support's lattice is more distorted by the incorporation of additional Pd^{2+} ions. In other words, the presence of one dopant might limit the solubility of another one in the fluorite type lattice of the support.

XPS measurements were also performed for some of the spent catalysts to determine if any changes in the chemical state or surface composition occurred after the activity tests. These results are summarized in Table 3.2.

Table 3.2: XPS results for Pd-Cr based catalysts tested after the CO + O$_2$ reaction (3x).

Sample	Pd binding energy (eV)	mol% Pd (XPS)	mol% Pd (theor.)	mol% Cr (XPS)	mol% Cr (theor.)
1Pd/2CrCZ-AR	336.8	4.97	1.44	6.08	2.77
1Pd/5CrCZ-AR	336.7	8.09	1.44	9.97	5.55
2Cr/1PdCZ-AR	337.7	2.39	1.44	12.55	2.77
5Cr/1PdCZ-AR	337.4	2.07	1.44	21.27	5.55

After testing of 1Pd/2CrCZ three consecutive times for the CO + O$_2$ reaction, it seems that the Pd chemical state has changed from atomically dispersed Pd^{2+} to PdO$_x$ clusters. The chemical state of Pd in 1Pd/5CrCZ remained the same, as the binding energy of 336.7 eV suggests that Pd is still in the form of sub-nm clusters. For 5Cr/1PdCZ, the binding energy of Pd slightly decreased from 337.6 eV to 337.4 eV after the reaction. The value 337.4 eV is slightly larger than the typical value found for Pd in bulk PdO (337.2 eV), and it was speculated that it might correspond to the interaction phase of a Pd-Cr mixed oxide that was formed in the reaction process [205].

The high loading of Pd earlier detected by XPS for 1Pd/5CrCZ was explained due to the presence of sub-nm PdO$_x$ clusters on the surface of the support. However, despite the fact that these clusters now also seem to be present for 1Pd/2CrCZ-AR and 1Pd/5CrCZ-AR, the Pd loadings were this time found to be notably smaller than the previously found value of 11.04 mol% for 1Pd/5CrCZ before the reaction. Intuitively it can be explained by a slight sintering of PdOx clusters during the reaction. It should be noted that the results of XPS should be interpreted with caution. Since the Zr3p core lines are strongly overlapping with the Pd3d core lines, there might be some deviations in the outcomes of the calculations due to the complicated line fitting and background subtraction. Therefore, looking at the general trends observed for the different samples rather than to focus on the absolute values measured by XPS appears to be a more reasonable strategy for understanding of the surface changes.

Table 3.3: XPS results for Pd-doped and Pd-impregnated Fe-based catalysts.

Sample	Pd binding energy (eV)	mol% Pd (XPS)	mol% Pd (theor.)
1Pd2FeCZ	337.7	2.68	1.44
1Pd5FeCZ	337.7	2.98	1.44
1Pd11FeCZ	337.7	2.68	1.44
1Pd/2FeCZ	337.7	3.77	1.44
1Pd/5FeCZ	337.7	3.34	1.44
1Pd/11FeCZ	337.7	5.61	1.44

Table 3.3 summarizes the XPS results for the Pd-Fe based catalysts. For both doped and impregnated samples, the binding energies for Pd were found to be close to the binding energy of Pd in 1PdCZ (337.8 eV). Fe-doped CZ seems to be effective in dispersing the noble metal phase in the form of single atoms, even for high Fe dopant concentrations that could distort the lattice of the support significantly. The molar percentage of Pd was found to be approximately two times higher than the intended loading for the Pd-doped samples. This result might indicate that Fe prefers to be located in the bulk of the support, forcing Pd to occupy sites closer to the surface. This assumption is consistent with the high thermal stability found for the Fe-doped samples in the previous chapter, as was clearly evidenced by XRD. In addition, the reduction of the Fe-doped samples occurring only at relatively high temperatures, as shown by H_2-TPR analysis, also suggests that Fe is situated relatively deep in the bulk of the support. This is further confirmed by the difference in the Pd molar percentages obtained by XPS for the doped and impregnated supports, which is now less significant compared to the ones of Pd-Cr based catalysts. We hypothesize that when Fe is located in the bulk, it allows the impregnated Pd to migrate deeper to the inside of the support. This in turn could explain the lower Pd loadings observed for the 1Pd/xFeCZ catalysts compared to the 1Pd/xCrCZ catalysts.

Table 3.4: XPS results for different Pd-Fe based catalysts.

Sample	Pd binding energy (eV)	mol% Pd (XPS)	mol% Pd (theor.)
1Pd/11CrCZ	337.2	7.59	1.44
1Pd/11FeCZ	337.7	5.61	1.44
1Pd/11CuCZ	337.2	11.57	1.44
1Pd/11CoCZ	337.7	5.06	1.44

Besides Cr- and Fe-doped ceria-zirconia, Cu- and Co-doped supports were also prepared with the polymer-assisted sol-gel method. As oxygen vacancies seem to play an important role in the CO + NO reaction mechanism according to the literature, only the Cu and Co supports with the highest dopant concentration (11.11 mol%) were impregnated with Pd. The XPS results for these catalysts are compared with those of the previously discussed 1Pd/11CrCZ and 1Pd/11FeCZ catalysts in Table 3.4.

One important observation that can be made from Table 3.4 are the similar Pd binding energies found for 1Pd/11CrCZ and 1Pd/11CuCZ (337.2 eV) on one hand, and the similar binding energies for 1Pd/11FeCZ and 1Pd/11CoCZ on the other hand. The binding energy of 337.2 eV indicates that Pd is in the form of bulk Pd oxide for 1Pd/11CuCZ. This observation is consistent with the results from the previous chapter, where it was reported that Cu easily segregates to the surface of the support. Thus, the high amount of Cu on the surface does not allow Pd to be stabilized by ceria-zirconia in the form of single atoms, leading to the formation of bulk Pd oxide that is weakly interacting with the support. Conversely, the Pd binding energy for 1Pd/11CoCZ indicates that segregation of Co to the support's surface might be limited. This is also further confirmed by XPS measurements for 11CoCZ in the previous chapter. The reported

value of 12.95 mol% for Co in 11CoCZ suggests that Co is more homogeneously distributed in the solid solution system, explaining why Pd can be more easily atomically dispersed on the surface. Finally, the relative low amount of surface Pd (5.06 mol%) that is recorded for 1Pd/11CoCZ also supports this reasoning.

3.2 Hydrogen-Temperature Programmed Reduction (H_2-TPR)

Hydrogen temperature-programmed reduction (H_2-TPR) measurements were performed to gain more insight into the active species and oxygen storage/release properties of the doped and impregnated Pd-Cr catalysts. The TPR results for 1PdCZ and 1Pd/CZ were already discussed in Chapter 2.
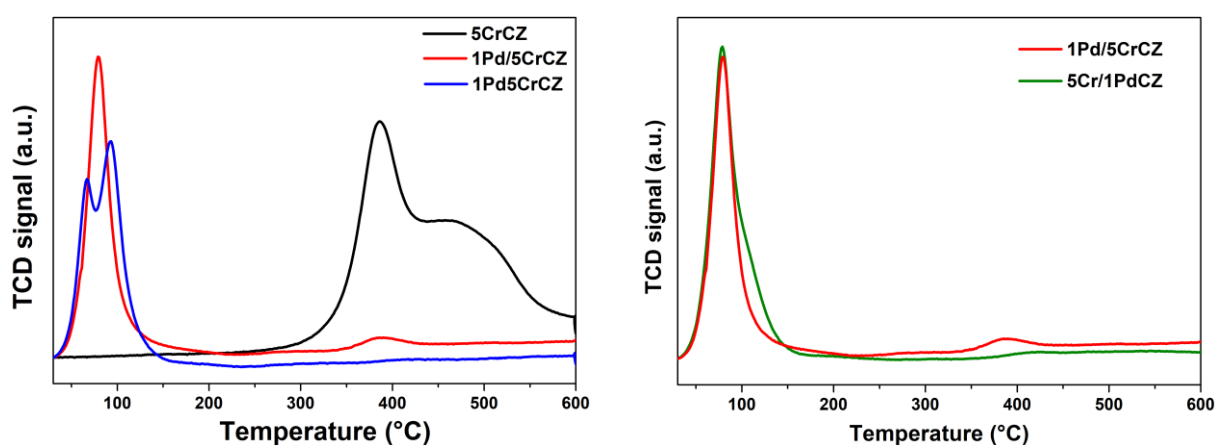
Figure 3.3: Comparison of the H_2-TPR profiles of the catalysts with and without Pd (left) and with Pd-doped and Pd-impregnated (right).

Figure 3.3 (left) shows that the reduction properties of the catalyst can be significantly improved when Pd is added to the catalyst formulation. After Pd was added to the 5CrCZ support via doping or impregnation, the reduction of the catalyst can already occur at temperatures below 100 °C. Conversely, for the catalyst without Pd, the first reduction peak appears at a much higher temperature (386 °C). Further, it can be seen that the Pd-doped and Pd-impregnated catalyst display a different reduction behavior. More specifically, two reduction peaks can be distinguished for 1Pd5CrCZ below 100 °C, while only one reduction peak was observed for 1Pd/5CrCZ at low temperatures. For 1Pd5CrCZ, the first reduction peak at 66 °C can be attributed to the reduction of PdO species, while the second peak at 92 °C may correspond to the reduction of Pd^{2+}-O-Ce^{4+} linkage structures at the surface and sub-surface region of the support [217–219]. Contrariwise, for 1Pd/5CrCZ a single peak was observed at 79 °C due to the reduction of PdO species on the surface of the support. However, it should be noted that the reduction peaks below 100 °C most likely also represent partial reduction of the support due to the hydrogen spillover effect typically observed for noble metal-based oxides [220,221]. This is further confirmed by the H_2/Pd ratios, which were larger than the stoichiometric value of 1 for both 1Pd5CrCZ (4.9) and 1Pd/5CrCZ (4.7).

It was concluded from Figure 3.3 (left) that the Pd-doped sample exhibits improved reducibility compared to the Pd-impregnated sample. This conclusion is reflected in the lower reduction onset temperature for 1Pd5CrCZ (65.7 °C) than for 1Pd/5CrCZ (79.2 °C). Secondly, the total amount of H_2 consumed below 100 °C is also slightly larger for 1Pd5CrCZ (0.462 mmol/g) than for 1Pd/5CrCZ (0.441 mmol/g). Finally, a second reduction peak was also observed at 387.8 °C for 1Pd/5CrCZ, and was attributed to the reduction of surface oxygen species of the support and possibly also CrO_x species [218]. For 1Pd5CrCZ, on the other hand, no such reduction peaks could be observed in the high temperature region, suggesting that the Pd-doped sample is more efficient in reducing the support at lower temperatures. This likely originates from the higher intimate contact between Pd and the support when the noble metal is incorporated in the crystal lattice, thereby facilitating the migration of the activated hydrogen from the metal to the support.

To further confirm that Pd-doped samples exhibit better reducibility than Pd-impregnated samples, the TPR-profiles of 1Pd/5CrCZ and 5Cr/1PdCZ were compared with each other in Figure 3.3 (right). Again, in contrast to the Pd-impregnated sample, the small reduction peak at 388 °C was clearly absent for the Pd-doped sample. Furthermore, a higher H_2 consumption was found for 5Cr/1PdCZ (0.611 mmol/g) at 78.6 °C than for 1Pd/5CrCZ (0.441 mmol/g) at 79.2 °C. Conclusively, these results demonstrate once more the enhanced reduction properties displayed by Pd-doped samples compared to Pd-impregnated samples.
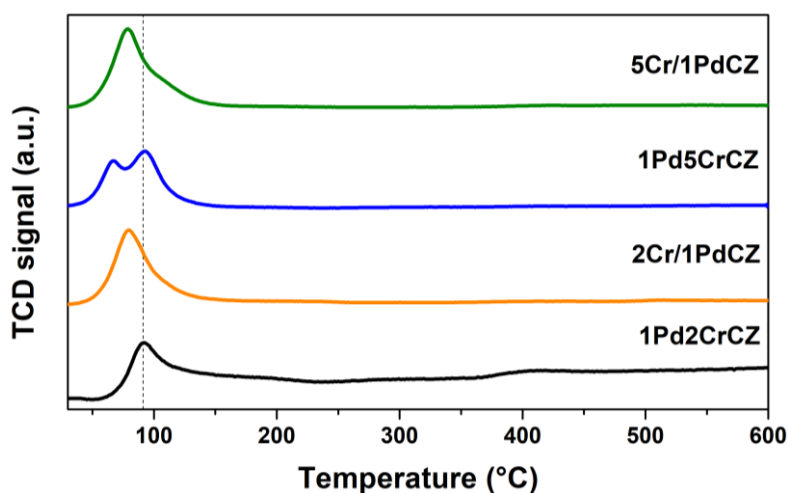
Figure 3.4: H_2-TPR profiles of Pd-Cr based catalysts.

The effect of the transition metal concentration on the reduction properties was investigated by comparing the TPR-profiles of the catalysts containing 2.77 and 5.55 mol% Cr. These results are shown in Figure 3.4. From this figure, it can be seen that that the reduction onset occurs at a lower temperature for 1Pd5CrCZ (66 °C) than for 1Pd2CrCZ (91 °C). Since lattice strain and defect formation both depend on the concentration of the dopant, the higher Cr concentration in 1Pd5CrCZ might explain the improved reducibility of this sample compared to 1Pd2CrCZ. This could also be derived from the higher amount of H_2 consumed by 1Pd5CrCZ (0.462

mmol/g) than by 1Pd2CrCZ (0.331 mmol/g). The lower H_2 consumption measured for 1Pd2CrCZ compared to the Pd-impregnated samples could not be clearly explained.

The improved oxygen storage/release properties for a higher Cr concentration is also clear from the TPR-profiles of 2Cr/1PdCZ and 5Cr/1PdCZ. The higher H_2 consumption recorded for 5Cr/1PdCZ (0.611 mmol/g) than for 2Cr/1PdCZ (0.513 mmol/g) could be simply explained by the reduction of more Cr oxide species on the surface of the former catalyst.

It was concluded from the TPR-profiles of 1Pd2CrCZ and 1Pd5CrCZ that for a higher dopant concentration the onset of reduction shifts to a lower temperature due to the enhanced oxygen mobility for a more distorted and defective crystal lattice. However, when these reduction profiles are compared with those of 2Cr/1PdCZ and 5Cr/1PdCZ, it appears that the single Pd-doped samples exhibit better reduction properties than the samples doped with both Pd and Cr. This is derived from the higher H_2 consumption values recorded for 2Cr/1PdCZ (0.513 mmol/g) and 5Cr/1PdCZ (0.611 mmol/g) compared to those for 1Pd2CrCZ (0.331 mmol/g) and 1Pd5CrCZ (0.462 mmol/g). Even more surprisingly, it was shown in the previous chapter that the amount of H_2 consumed for simple 1PdCZ was 0.669 mmol/g, which is more than the amount of H_2 consumed by the Pd-Cr based samples reported here. We hypothesize that without Cr the interaction between Pd and the support is intrinsically higher. Consequently, when homogeneously distributed Pd^{2+}-O-Ce linkages are formed throughout the whole crystal lattice of the support, the support might be reduced more efficiently. In other words, the intimate contact between Pd and Ce might facilitate the spillover of hydrogen from the noble metal to the support, especially when the Pd is homogeneously distributed in the solid solution. However, this hydrogen transfer might be partially suppressed when Cr is also incorporated in the crystal lattice alongside with Pd due to a potential decrease in the synergistic interaction between Pd and Ce and less homogeneously distributed Pd^{2+}-O-Ce linkages.

3.3 In situ DRIFTS

DRIFTS measurements were performed to characterize the Pd phase in the 1PdCZ, 1PdCZ-800C, 1Pd/5CrCZ, 5Cr/1PdCZ(-AR) and 1Pd11FeCZ samples. CO was used as a probe molecule. The samples were first calcined at 300 °C and then cooled to room temperature in the presence of 2 mbar O_2. The bands observed between 2300 and 2400 cm^{-1} correspond to gaseous CO_2, hence indicating that CO is being oxidized by the samples.
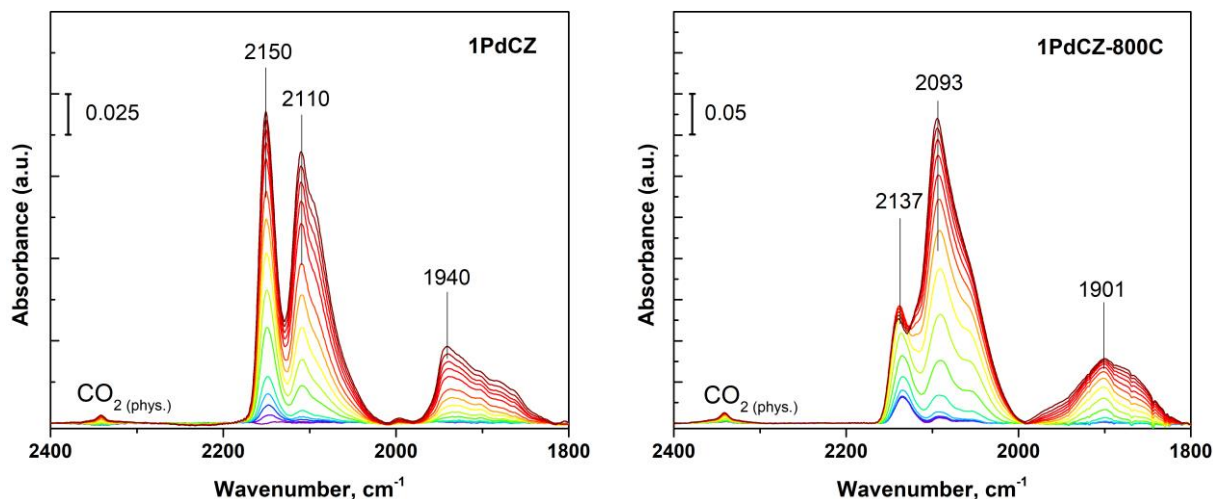
Figure 3.5: IR spectra of 1PdCZ (left) and 1PdCZ-800C (right)

Three bands were observed in the IR spectra of 1PdCZ, as shown in Figure 3.5 (left). The high frequency band at 2150 cm^{-1} was attributed to single-atomic or highly oxidized Pd species, which is consistent with the high binding energy of Pd (337.7 eV) measured by XPS [147]. The second band at 2110 cm^{-1} was assigned to CO adsorbed on Pd twin-doped sites [222], while the low-frequency band at 1940 cm^{-1} corresponds to CO adsorbed on metallic Pd clusters and/or nanoparticles [223]. The IR spectra of 1PdCZ-800C, shown in Figure 3.5 (right), also displayed three bands, which were slightly shifted to lower frequencies compared to the bands observed for 1PdCZ. This result indicates that more reduced Pd clusters or species are present for 1PdCZ-800C than for 1PdCZ. In addition, the lower intensity of the high-frequency band for 1PdCZ-800C suggests that there are also less single-atomic species than for 1PdCZ. The higher intensity of the lower-frequency band suggests that there are more reduced Pd clusters formed when the sample is calcined at temperatures as high as 800 °C. Still it should be noted that the highly dispersed nature of Pd is at least partially preserved even after 800 ºC. Our EXAFS data showed only the first Pd-O shell, meaning that the majority of the Pd species are of isolated nature. This result is of significant importance since it is known that bulk PdO oxide species are decomposing around 800 ºC [78,79]. Herein we synthesized the catalysts which can withstand such high temperatures without sintering/decomposition of the active phase.
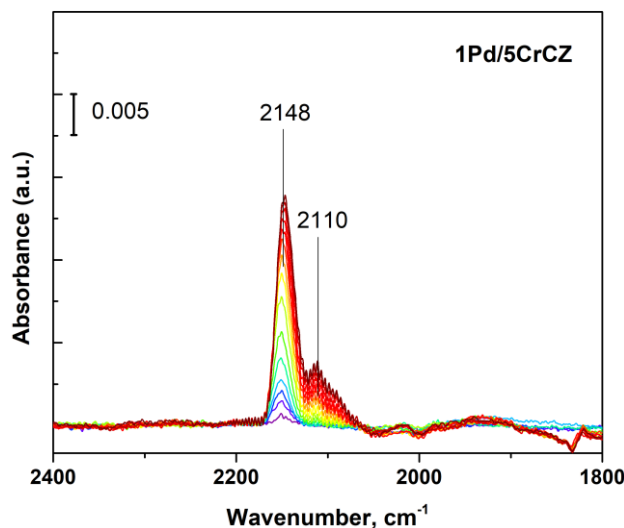
Figure 3.6: IR spectra of 1Pd/5CrCZ

The IR spectra of the 1Pd/5CrCZ sample are shown in Figure 3.6. The spectra display one high-frequency band at 2148 cm^{-1}, which could be attributed to CO adsorbed on single-atomic or highly oxidized Pd species [147]. A low-intensity band was also observed at 2110 cm^{-1}, which was assigned to CO adsorbed on Pd twin-doped sites [222]. Apparently, a small fraction of the impregnated Pd is able to substitute some of the Ce^{4+} ions at the surface and subsurface region of the support [224].

The result shown in Figure 3.6 is quite remarkable, as it was previously demonstrated for 1PdCZ by DRIFTS that there are at least three different Pd species, including reduced metal species. As no frequency bands corresponding to metallic Pd clusters could be observed in the IR spectra of 1Pd/5CrCZ, it can be concluded that Cr might be able to stabilize the Pd and prevent the formation of Pd clusters. This is consistent with the XPS results which showed that the binding energy of Pd increased for 1Pd2CrCZ and 1Pd5CrCZ, pointing to the formation of highly dispersed and oxidized Pd species. However, lower binding energies were observed for Pd in 1Pd/5CrCZ and 1Pd/11CrCZ from XPS, and no clear explanation could be given for this discrepancy. Nevertheless, it was previously mentioned that XPS measurements are considerably less informative for Pd-based ceria-zirconia systems due to a strong overlapping of the Zr3p core-lines with the Pd3d core-lines. Therefore, the DRIFTS measurements were considered to be more reliable, which also follows from its intrinsically higher sensitivity for structural and electronic effects.
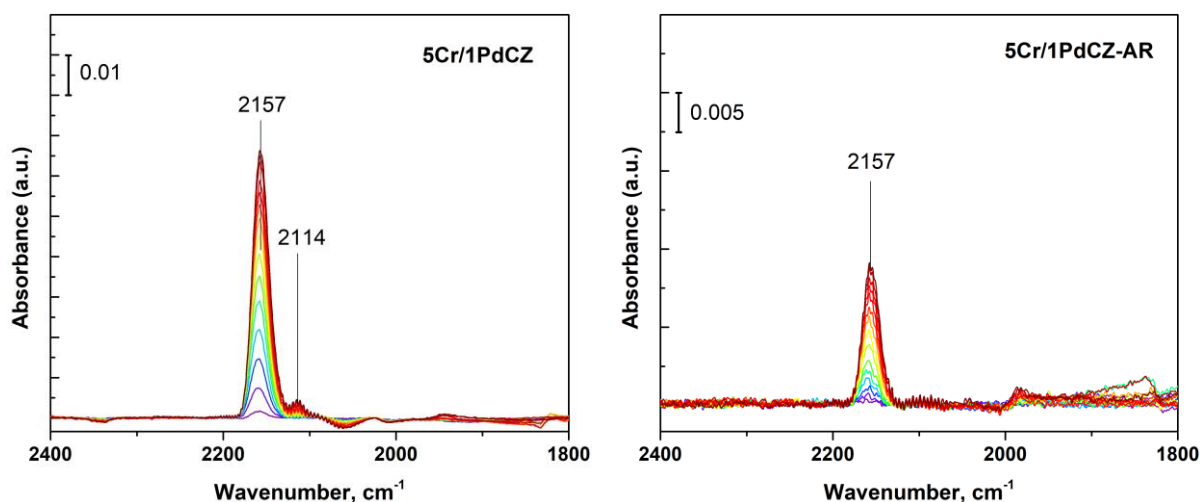
Figure 3.7: IR spectra of 5CrCZ/1PdCZ (left) and 5CrCZ/1Pd tested after CO + O$_2$ (3x) (right)

The assumption that Cr might be able to stabilize the Pd in the CZ support was further confirmed by the IR spectra of 5Cr/1PdCZ, shown in Figure 3.7 (left). The absence of a low-frequency band indicates that no metallic Pd species were formed. Moreover, Figure 3.7 (right) shows that no reduced Pd metal species were formed even after testing the sample three consecutive times in the CO + O$_2$ reaction. Frequency bands corresponding to CO adsorbed on Cr oxide species were not observed, as these bands are typically located between 2165 and 2178 cm^{-1} [225]. Consequently, the high-intensity band at 2157 cm^{-1} could be attributed to CO adsorbed on single-atomic and highly oxidized Pd^{2+} sites [205]. However, it was also speculated that this band might correspond to dispersed Pd decorated by Cr, as it was previously suggested by XPS data that Pd and Cr might form a mixed oxide phase. Finally, the low-intensity band at 2114 cm^{-1} was assigned to CO adsorbed on the Pd twin-doped sites [222]. These results clearly demonstrate that the formation of a highly oxidized Pd state is favored when Cr is added to the catalyst formation, most likely due to a synergistic interaction occurring between the noble metal and the base metal. It has already been shown in the literature that in some cases such an interaction can exist between Pd and Cr [205].
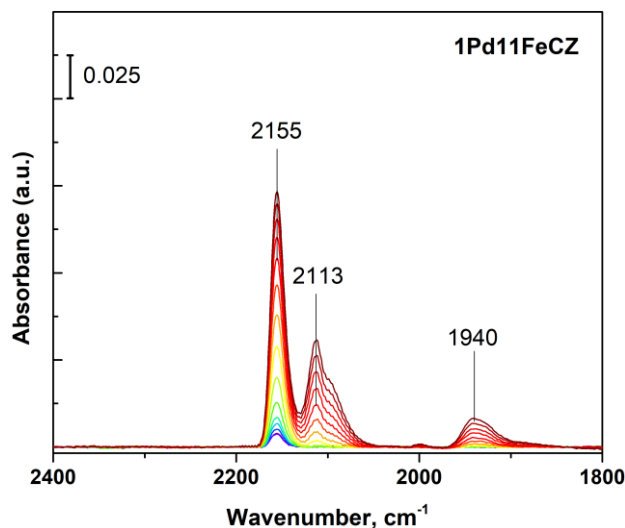
Figure 3.8: IR spectra of 1Pd11FeCZ

Further, the IR-spectra of 1Pd11FeCZ were also measured under the same conditions as for the previous samples. These results are shown in Figure 3.8. In contrast to the Pd-Cr based samples, metallic Pd clusters seem to be present for the Pd-Fe based sample, as derived from the frequency band at 1940 cm^{-1}. However, compared to the same frequency band observed for 1PdCZ, the intensity of the band is much lower now when Fe is also incorporated into the crystal lattice. Therefore, it can be concluded that the presence of Fe also seems to make the Pd more stable in the CZ support. In addition, it was also observed that the frequency bands corresponding to Pd dopant sites and highly oxidized Pd are slightly more shifted to higher frequency values compared to the same frequency bands observed for 1PdCZ. This observation also indicates that the Pd in the presence of Fe is in a more oxidized state compared to the Pd in 1PdCZ. Nevertheless, the stabilization of Pd induced by the Fe was less pronounced than for the Pd-Cr based samples, for which reduced Pd species were completely absent.

3.4 Catalytic activity tests

3.4.1 CO + NO reaction

The activity of various catalysts, either with or without Pd, were tested for the CO + NO reaction. As several studies have reported high activities for Cu- and Co-based catalysts for the reduction of NO to N_2, xCuCZ and xCoCZ catalysts were tested first for this reaction [226–229]. These results are shown in Figure 3.9.
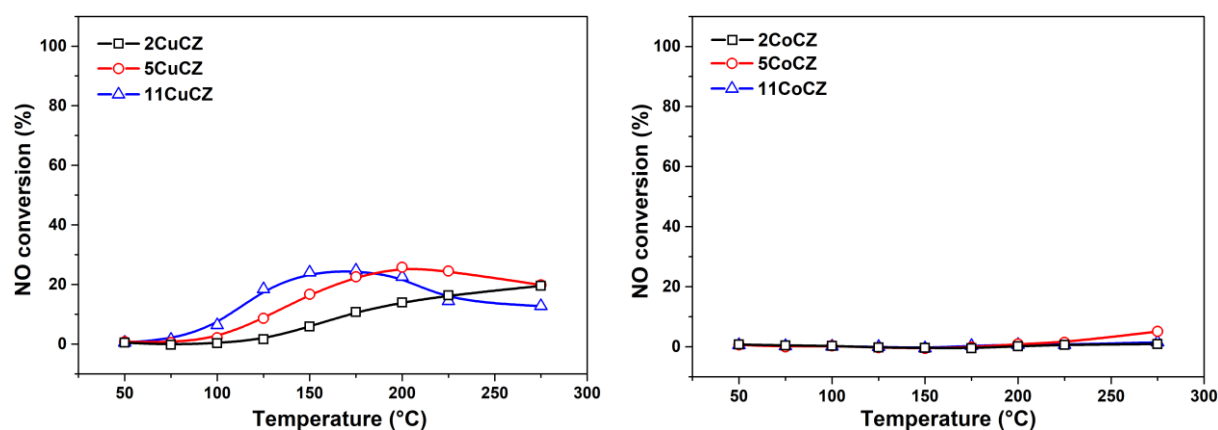
Figure 3.9: NO conversion curves for Cu- and Co-doped ceria-zirconia supports.

Figure 3.9 shows that very low NO conversions are reached for both xCuCZ and xCoCZ catalysts. In particular, it can be seen that xCoCZ even shows negligible activity for the reduction of NO, which is in sharp contrast to the results observed by other research groups for Co-based catalysts [228,229]. It should be noted that in the work of Savereide et al. high NO conversions were reported for CeO_2-based catalysts which likely contain clusters of Co oxides, as it was shown by the Raman and EXAFS. However, by means of in situ XAFS it was concluded that the Co^{2+} oxidation state must be responsible for the highest activity. In our case from the XPS we can also conclude that Co has an oxidation state of +2, but as it was found upon catalytic testing the activity is almost negligible. Thus, it can be concluded that the isolated Co^{2+} species (shown by the EXAFS in the previous chapter) cannot efficiently reduce the NO by CO, while the clusters are able to, relying on the data shown in the abovementioned paper. This is further confirmed by a recent study of Zhang et al., where it was shown that the best NO reduction activity was achieved when small clusters of Co_3O_4 are formed [230]. In addition, it was found by in situ XANES that the activity is governed by Co^{3+}, while Co^{2+} seems to be not active.

For the Cu-doped samples, the activity was also found to be very modest, implying that small clusters and/or single-atom Cu species are not responsible for the NO reduction at low temperatures. This goes in line with the previous studies being performed on leached Cu-Ce catalysts, where the activity dropped once the clusters/nanoparticles were removed [231].

Conclusively, our catalytic results indicate that isolated species of Co and Cu obtained for our sol-gel prepared catalysts do not perform in the NO reduction reaction at low temperatures. The isolated nature of Cu and Co species was confirmed by the EXAFS data shown in the previous

72

chapter. Furthermore, these results demonstrate the structure sensitivity of the CO + NO reaction, which has also been reported by other studies in the literature [194,232].

In order to achieve higher NO conversions, Pd (1 wt.%) was deposited in a next step onto the surface of the doped supports via a conventional wet impregnation technique. For the impregnation step the supports with the highest dopant concentration (11.11 mol%) were selected to have the maximum amount of oxygen vacancies available that can assist in the reduction of NO to N_2 [28]. The catalytic activities of the doped supports impregnated with Pd were compared with those of 1Pd/CZ and one-step synthesized 1PdCZ in Figure 3.10.
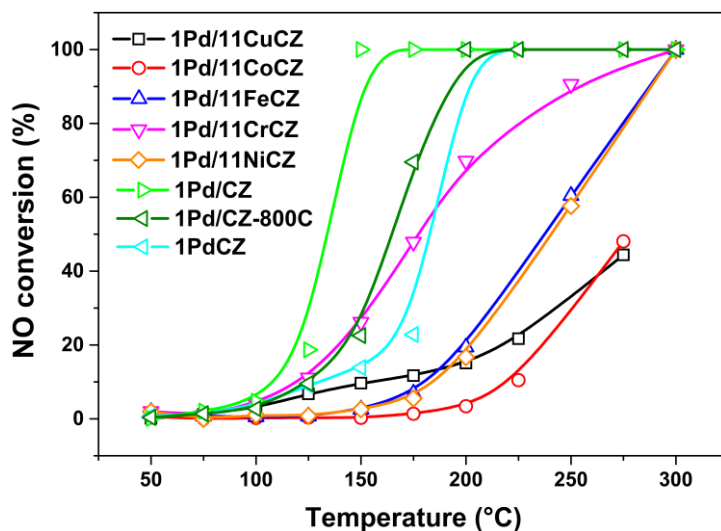
Figure 3.10: NO conversion curves for one-step synthesized 1PdCZ and Pd-impregnated ceria-zirconia supports.

Again, Figure 3.10 shows that low NO conversions are reached for the Co- and Cu-based catalysts, although the addition of Pd improved their activity at temperatures higher than 200 °C. 1Pd/11FeCZ and 1Pd/11NiCZ showed notable activities only at temperatures higher than 200 °C, while 1Pd/11CrCZ exhibited a much higher activity, reaching nearly 50% NO conversion at 175 °C. Surprisingly, the highest catalytic activity was observed for 1Pd/CZ, followed by 1Pd/CZ-800C and 1PdCZ, reaching 100% NO conversions at 150 and 200 °C, respectively.

The results shown in Figure 3.10 seem to be contradictory with what has been previously published. The majority of the studies have shown the beneficial effects of doping the support with transition metals, leading to the creation of oxygen vacancies that can improve the reduction of NO by assisting in the decomposition of the N_2O intermediate [28]. Furthermore, it has been shown that synergistic interactions between the noble metal and the dopant can also significantly improve the NO conversion efficiencies [127]. Doping the ceria-zirconia support in our case, however, only seemed to further reduce the catalytic activity. It should be noted though that an intimate contact between the noble metal and the support may also play a crucial role in the overall catalytic activity, as was previously proposed by Rao et al. [202]. More recent studies have also shown that the Pd-Ce interface may represent the active phase in the CO oxidation and NO reduction reactions [233–235]. Taking into account that CeO_2 in our case has already been doped with a considerable amount of Zr^{4+} ions, introducing a third metal dopant

in the fluorite type lattice may adversely affect the metal-support interaction between Pd and CeO_2. This negative doping effect may become even more important when Pd is impregnated on the surface of the support. Indeed, Fernández-García et al. found lower NO conversion efficiencies when Pd and Cr were co-impregnated on a CZ/Al_2O_3 support [205]. This observation was explained by Cr that might modify the interface between Pd and CZ, resulting in a lower NO reduction activity.

The importance of the Pd-Ce interface in the CO + NO reaction is further confirmed by the high activity observed for one-step synthesized 1PdCZ. In Chapter 2, XPS analysis showed that the Pd in 1PdCZ is highly dispersed, which can contribute to the improved activity for this sample. Furthermore, due to the fact that Pd in 1PdCZ is incorporated into the fluorite type lattice of the support, an intimate contact between Pd and CeO_2 is more easily established. Consequently, the Pd-Ce interface might increase significantly, which could lead to a more efficient use of the oxygen vacancies which are located in close proximity to this interface [202,236]. Further, the intimate Pd-Ce contact might also improve the synergistic interaction between the noble metal and the support. This interaction involves the stabilization of the Pd^{2+} ion by Ce^{4+}. More specifically, when Pd^{2+} would be reduced to Pd^0 in the course of a redox reaction, electrons from Pd^0 are subsequently transferred to Ce^{4+} leading to the regeneration of Pd^{2+} and the formation of Ce^{3+} [237]. In this way, both the noble metal and CeO_2 participate in the catalytic redox reactions due to electron transfer reactions occurring between them. In addition, the presence of noble metal ions on the surface of the support is a key feature of solid solution systems. In particular, Baidya et al. reported that activation energies for CO oxidation decrease when the effective charge on Pd ions increases [238]. In combination with the increased OSC observed for noble metal-doped systems, this might explain why several research groups observed higher catalytic activities for solid solution catalysts in comparison with metal supported catalysts. The H_2-TPR measurements performed for 1PdCZ and 1Pd/CZ in Chapter 2 confirm that noble metal doped systems typically exhibit improved reduction properties compared to noble metal impregnated systems.

Taking into account the above arguments, one would expect to see a higher catalytic activity for 1PdCZ than for 1Pd/CZ. Surprisingly, the opposite was found to be true. Moreover, even the Pd-impregnated sample calcined at 800 °C displayed a higher CO oxidation activity than 1PdCZ, and two reasons can be given to explain this result. First, more noble metal species are present on the surface of the support for impregnated samples than for doped samples that could catalyze the intended reactions. Second, and not less important, is the ability of ceria-zirconia to disperse noble metals on its surface with high efficiency. This is further confirmed by the XPS measurements for 1Pd/CZ shown in the previous chapter. The larger Ce^{3+}/Ce^{4+} ratio observed for 1Pd/CZ (0.25) than for 1PdCZ (0.20) suggests that Pd might be strongly interacting with CeO_2, and that similar synergistic interactions are established between the noble metal and the support as for Pd-doped ceria-zirconia. Even after calcining 1Pd/CZ at 800 °C, it could be that the Pd is still relatively well dispersed on the surface due to a strong metal-support interaction with ceria-zirconia. Its lower CO oxidation activity compared to the uncalcined 1Pd/CZ could then be largely attributed to the lower surface area due to the sintering of the support. Alternatively, it might be that the supported noble metal itself has sintered, and that the formation of active reduced Pd species could compensate for the loss in activity caused

by the decrease in surface area. However, since no XPS or DRIFTS measurements were performed for 1Pd/CZ-800C, it is not fully clear what may cause the higher activity of this sample compared to 1PdCZ.

Even though Figure 3.10 shows that 1Pd/CZ is more efficient in reducing NO than 1PdCZ, the Pd-doped sample is more preferred to use in a real TWC because of its longer lifetime. This can be ascribed to the higher sintering resistance of the active noble metal phase in 1PdCZ when the metal is incorporated into the lattice of the support after doping. As the Cr-doped support showed considerable higher activity compared to the Co-, Cu-, Fe- and Ni-doped supports, it was decided to prepare Cr-doped 1PdCZ (1Pd2CrCZ and 1Pd5CrCZ) in a next step. Their performance in the CO + NO reaction was compared with that of two-step synthesized 1Pd/xCrCZ and xCr/1PdCZ in Figure 3.11.
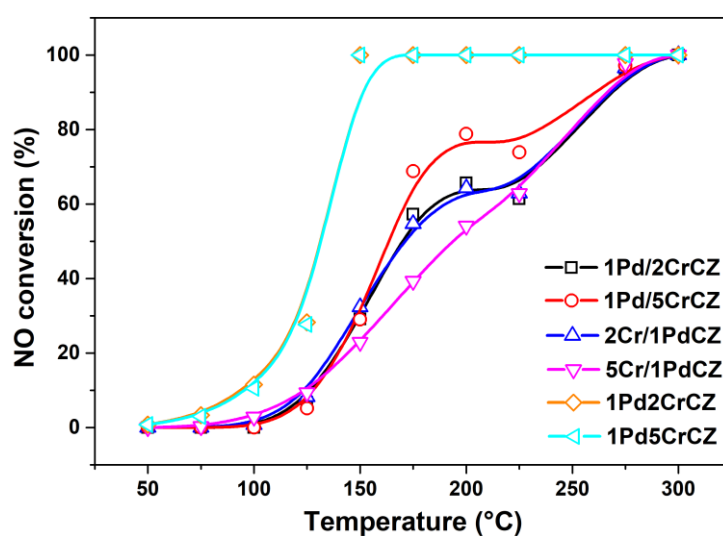
Figure 3.11: NO conversion curves for Pd-doped and Pd-impregnated Cr-based catalysts.

It can be seen from Figure 3.11 that the one-step synthesized 1PdxCrCZ samples perform notably better in the CO + NO reaction than the impregnated 1Pd/xCrCZ and xCr/1PdCZ samples. 1Pd2CrCZ and 1Pd5CrCZ display similar activities, reaching 100% NO conversion at a temperature as low as 150 °C. Thus, co-doping of the CZ support with Pd and Cr can significantly improve the catalytic activity compared to single doped 1PdCZ.

The TPR-profiles in Figure 3.3 (left) already confirmed that one-step synthesized 1Pd5CrCZ exhibits improved redox properties compared to two-step synthesized 1Pd/5CrCZ. Furthermore, one might also expect that 5Cr/1PdCZ would perform better in the CO + NO reaction than 1Pd/5CrCZ due to the fact that more H_2 was consumed by the former catalyst in the TPR experiments. However, despite the enhanced oxygen release properties of 5Cr/1PdCZ, Figure 3.11 clearly shows that 1Pd/5CrCZ exhibits a substantially higher catalytic activity for the reduction of NO. Therefore, it can be concluded that the results from the H_2-TPR experiments on its own cannot explain all the observed catalytic activity trends.

Besides the noble metal dispersion, reduction properties and Pd-Ce intimate contact, the amount of Pd atoms on the support's surface was also previously given as an important requisite to

explain the catalytic activity trends. Taking the latter into account, it might become clear why 5Cr/1PdCZ is performing so poorly in the CO + NO reaction. More specifically, the high amount of Cr species on the support's surface could be covering the Pd atoms significantly in 5Cr/1PdCZ, thereby hindering the N-O bond cleavage by the active noble metal phase.

Figure 3.11 further shows that 1Pd/2CrCZ and 2Cr/1PdCZ display similar catalytic activities, intermediate between those of 1Pd/5CrCZ and 5Cr/1PdCZ. The reason why 1Pd/5CrCZ is performing better than the 2.77 mol% Cr-based impregnated catalysts could be due to a synergistic interaction taking place between the noble metal and Cr. This interaction might become less important for low Cr concentrations (2.77 mol%), especially when either Pd or Cr is deposited onto the support. Conversely, when both Pd and Cr are incorporated into the fluorite type lattice, this interaction could be more pronounced, as both metal components will then might be located closer to each other or interacting through the long range-effects in the lattice. Consequently, it can be concluded that synergistic interaction could between the different metal components can occur more easily for one-step synthesized samples.

The synergistic interaction taking place between Pd and Cr was previously also demonstrated by DRIFTS. The absence of a low-frequency band for 1Pd/5CrCZ and 5Cr/1PdCZ indicated that Cr might stabilize the Pd in a highly oxidized form, even after testing the sample several times in the CO + O_2 reaction. Further proof of such an interaction between Pd and Cr can be found in the literature. Fernández-García et al. observed that Cr entities placed on reduced Pd nanoparticles are forming Pd^{2+} sites on the outer surface of the particle [205]. The formation of these Pd^{2+} ions could then partially explain the improved CO oxidation activity, as these ions could limit the CO inhibition effect that is typically observed for metallic particles. DRIFTS measurements were also performed in this study, and these results also demonstrated that a synergistic interaction is occurring between Pd and Cr. More specifically, after adding Cr to the Pd-impregnated catalyst, a decrease in the intensity of the low-frequency band corresponding to Pd^0 species was observed, while the intensity of the high-frequency band corresponding to highly oxidized Pd species increased.

Attributing the improved catalytic activities of 1Pd2CrCZ and 1Pd5CrCZ solely to synergistic effects between Pd and Cr, however, cannot fully explain the observed activity trends. For example, 1Pd/CZ clearly showed a substantial higher catalytic activity than 1Pd/2CrCZ, despite the fact that XPS analysis showed that a similar amount of Pd is present on the surface of both samples. Moreover, XPS even showed that the Pd in 1Pd/2CrCZ (BE = 337.7 eV) is more dispersed than in 1Pd/CZ (BE = 337.4 – close to bulk PdO), yet the former catalyst is performing worse in the CO + NO reaction. From this, it could then be concluded that less dispersed Pd species are needed in the CO + NO reaction, which is in line with the structure sensitivity of this reaction shown in the literature [194]. Conversely, the binding energies of the Pd in 1Pd2CrCZ and 1P5CrCZ were found to be 337.8 and 337.9 eV, respectively, indicating the presence of highly ionic and dispersed Pd^{2+}. Therefore, it can be concluded that the dispersion and chemical state of Pd might not be the only determining factors for the observed activities. In addition, as most of the Pd is situated in the bulk of the support for 1Pd2CrCZ and 1Pd5CrCZ, the amount of surface Pd species available for catalyzing the NO reduction can also not explain the superior activity of 1Pd2CrCZ and 1Pd5CrCZ. Thus, it was postulated that the

Pd-Ce contact might be the most important contributing factor to the increased catalytic activities of 1Pd2CrCZ and 1Pd5CrCZ. We speculate that when the noble metal is incorporated into the fluorite type lattice of the support, then it will most likely be located more closely to the defects and oxygen vacancies created by the Cr dopant ions, thus the interaction and synergistic effect of co-doping is more pronounced. As both the Pd and the oxygen vacancies play a crucial role in the reduction of NO to N_2, the NO conversion efficiency might be increased due to a more favorable interaction between these two active components.

Pd-Fe based catalysts were prepared in a final step to confirm that one-step synthesized samples perform better in the CO + NO reaction than Pd-impregnated samples. Iron was selected because of several studies in the literature demonstrating that with Fe-based CeO_2 catalytic systems promising results can be achieved for the reduction of NO and the decomposition of N_2O [239,240]. The catalytic activity data of these samples are shown in Figure 3.12.
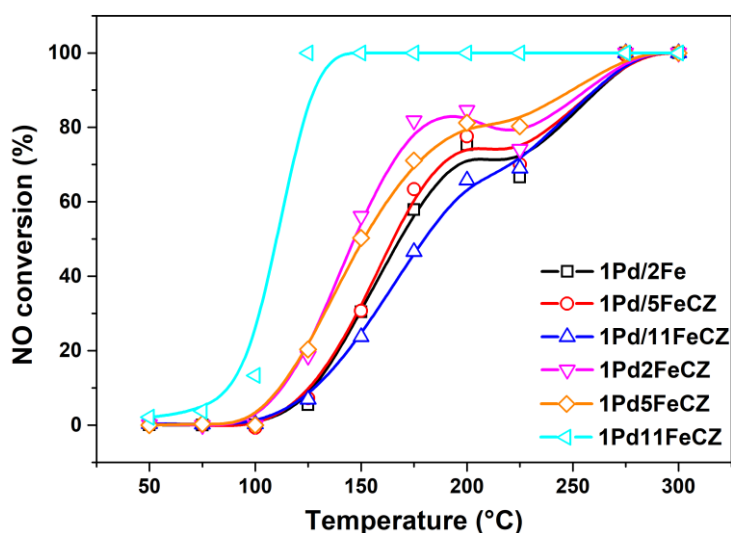
Figure 3.12: NO conversion curves for Pd-doped and Pd-impregnated Cr-based catalysts.

The NO conversion curves in Figure 3.12 demonstrate that one-step synthesized Pd-Fe samples perform significantly better in the CO + NO reaction than Pd-impregnated samples, as was previously also observed for the Pd-Cr based samples. The highest NO conversion efficiency was found for 1Pd11FeCZ, reaching 100% NO conversion at 125 °C and thus performing slightly better than the 1PdxCrCZ samples. 1Pd/11FeCZ, on the other hand, exhibited the lowest catalytic activity of all the Pd-Fe based catalysts tested for the CO + NO reaction.

1Pd/xFeCZ samples displayed catalytic activities similar to the 1Pd/xCrCZ samples for the reduction of NO, hence performing worse than undoped 1Pd/CZ. We infer that interaction taking place between Fe and surface Pd (added by impregnation) could not provide acceptable catalytic activity. However, co-doping the ceria-zirconia support with Pd and 2.77 or 5.55 mol% Fe increased the NO reduction activity. Interestingly, a significant improvement in the catalytic activity was observed when the Fe dopant concentration was increased from 5.55 to 11.11 mol%. It was earlier assumed that Fe might be located relatively deep in the bulk of the ceria-zirconia support, which could then explain the results from XPS and the H_2-TPR experiments. In line with that, it can be assumed that only for high Fe-dopant concentrations defects and

oxygen vacancies are created in close proximity to the Pd in the surface and subsurface of the ceria-zirconia support.

A synergistic interaction occurring between Pd and Fe in 1Pd11FeCZ was also confirmed by DRIFTS measurements (Figure 3.8). Compared with the IR spectra of 1PdCZ, it was observed that the intensity of the low-frequency band decreased significantly, while the high-frequency band shifted to even higher frequencies when 1PdCZ was additionally doped with 11.11 mol% Fe. This result indicated that the presence of Fe in 1Pd11FeCZ makes the Pd more stable towards sintering and clustering, as low-frequency bands were less pronounced. Since 1Pd11FeCZ showed the highest activity of all the samples tested for the CO + NO reaction, it can be assumed that a highly oxidized Pd state might be part of the active phase in this reaction. This is in sharp contrast to many of the results shown in the literature, in which it is generally stated that reduced noble metal species or clusters are needed to achieve a high NO conversion efficiency due to the structure sensitivity of the CO + NO reaction [194,227,230].

At first sight, it might be surprising to see that 1Pd11FeCZ is showing the highest catalytic activity for the CO + NO reaction, while 1Pd/11FeCZ is performing the worst of all the Fe-based samples. However, this result might actually confirm the hypothesis that the Pd-Ce intimate contact next to the oxygen created by the second dopant might be the determining factor for obtaining a high NO conversion efficiency. As it was shown by XPS that Pd is more segregated to the surface for 1Pd/xFeCZ, the Pd-Ce-Fe interface is most likely reduced when Pd and Fe are more spatially separated from each other.

A concave feature in the NO conversion graphs for most Pd-Cr and Pd-Fe based catalysts was observed around temperatures slightly below 200 °C. Several research groups also observed a similar feature in the NO conversion graphs for Pd in combination with a reducible CeO_2 or CeO_2-ZrO_2 support [24,190,241]. As such a feature was not observed for Pd supported on a non-reducible Al_2O_3 support, this observation might be attributed to the promoting effect of the reducible support [190]. More specifically, it has been shown by DRIFTS studies that on the surface of a CeO_2 or CeO_2-ZrO_2 support multiple intermediate compounds can be formed, such as nitrates and carbonates, that can inhibit the adsorption of the reactant molecules [242]. These carbonate species (NCO) are only formed at higher temperatures by the reaction between dissociated nitrogen ($N_{ad)}$ and adsorbed CO (CO_{ad}). N_{ad} can already be formed at lower temperatures by the reaction between CO_{ad} and NO_{ad}, according to reaction (1):

$$CO_{ad} + NO_{ad} \rightarrow CO_2 + N_{ad} \tag{1}$$

Subsequently, NCO might be formed at higher temperatures by the reaction between CO_{ad} and N_{ad}, according to reaction (2):

$$CO_{ad} + N_{ad} \rightarrow NCO_{ad} + * \tag{2}$$

As these adsorbed NCO species inhibit the adsorption of CO and NO on the surface of the support, the NO conversion is expected to decrease. If the temperature is further increased, the NCO_{ads} species can decompose along with N_2O_{ad} to regenerate the surface, and the NO conversion is expected to increase again, explaining why a concave feature is often observed for the CO + NO reaction.

As NCO and NO_x species thermally decompose at temperatures around 200 °C, it is expected that not only the NO conversion will increase, but also the N_2 selectivity. In order to verify this assumption, the N_2 selectivity was calculated for some of the key samples that showed high NO conversion efficiencies. In addition, the N_2 selectivity was also calculated for the poorly performing 1Pd/11FeCZ as a comparison. These results are shown in Figure 3.13, together with the associated NO conversion values of the different samples.
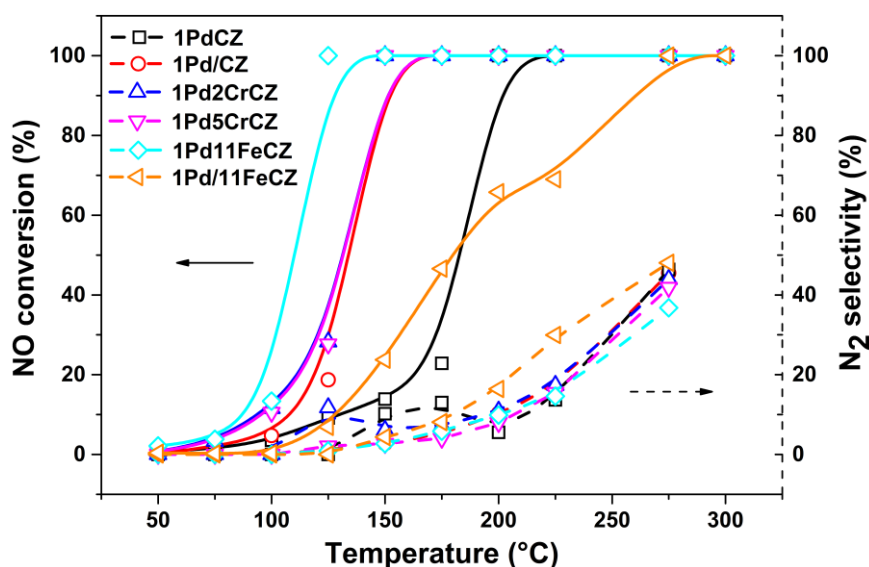

Figure 3.13: N_2 selectivity and NO conversion curves for Pd-doped and Pd-impregnated catalysts.

The highest N_2 selectivity was found for 1Pd/11FeCZ (48.1%), followed by 1PdCZ (46.4%) and 1Pd/CZ (45.5%) at 275 °C. Further, 1Pd2CrCZ and 1Pd5CrCZ showed a similar N_2 selectivity (43.7% and 41.9%, respectively), while the lowest N_2 selectivity was – surprisingly – found for 1Pd11FeCZ (36.82%). Similar values were reported by other studies on the NO reduction by ceria-based catalysts, and hence these results demonstrate that N_2O is the preferred product formed at low temperatures [228].

Although the lowest NO conversion efficiency was found for 1Pd/11FeCZ, its N_2 selectivity was higher than that of all the other samples. In general, it is expected that the catalyst with the highest amount of oxygen vacancies displays the highest N_2 selectivity, as it is extensively reported in the literature that N_2O decomposition takes place on the oxygen vacancies of the support [28]. However, since a high N_2 selectivity was also observed for the Pd-impregnated samples, we assume that there is another pathway that could lead to the selective formation of N_2. More specifically, for the Pd-doped samples, both oxygen vacancies and Pd^{2+} ions can act as the adsorption sites for NO [134]. After the cleavage of the N-O bond on Pd^{2+}, the resulting N moiety could recombine with the adsorbed NO on the oxygen vacancy, leading to the undesired formation of N_2O. Furthermore, as N_2O can easily desorbs from the different surface sites on the support, higher temperatures would be needed to complete the reduction of N_2O to N_2 [24]. Conversely, when more Pd and less oxygen vacancies are present on the surface, as is usually the case for Pd-impregnated samples, more NO molecules can dissociate on Pd, leading to a more selective formation of N_2 by the recombination of the N surface moieties. Hence, this

alternative pathway to the formation of N_2 could explain why a relatively high N_2 selectivity was found for the Pd-impregnated samples compared to the Pd-doped samples.

Table 3.5: TOF data of CO + NO reaction, calculated for the NO conversions at 100 °C and normalized by the amount of Pd determined by ICP-OES for each catalyst.

Sample	TOF (s^{-1})
1PdCZ	0.038
1Pd/CZ	0.048
1Pd2CrCZ	0.119
1Pd11FeCZ	0.147

Finally, turnover frequencies (TOF, s^{-1}) were calculated for the catalysts showing the highest NO conversion efficiencies. This data is summarized in Table 3.5. The values were calculated for the NO conversion at 100 °C, and normalized by the amount of Pd present in the catalyst determined by ICP-OES. The weight percentages of Pd, Cr and Fe found by ICP-OES are provided in the Supporting Information.

3.4.2 CO + O$_2$ reaction

A wide range of noble and transition metal based ceria-zirconia catalysts could be synthesized in a relatively short period of time due to the high simplicity of the one-pot, polymer-assisted sol-gel method that was used in this study. This allowed us to also investigate the CO + O$_2$ reaction, which is a second important reaction occurring in the TWC. The CO oxidation activity was tested for both doped and impregnated CZ supports, either with or without Pd.

In Figure 3.14 the catalytic activities of 1PdCZ and 1PdCZ-800C are compared with those of xCoCZ and xCuCZ of different transition metal loadings (x = 2.77, 5.55 and 11.11 mol%).
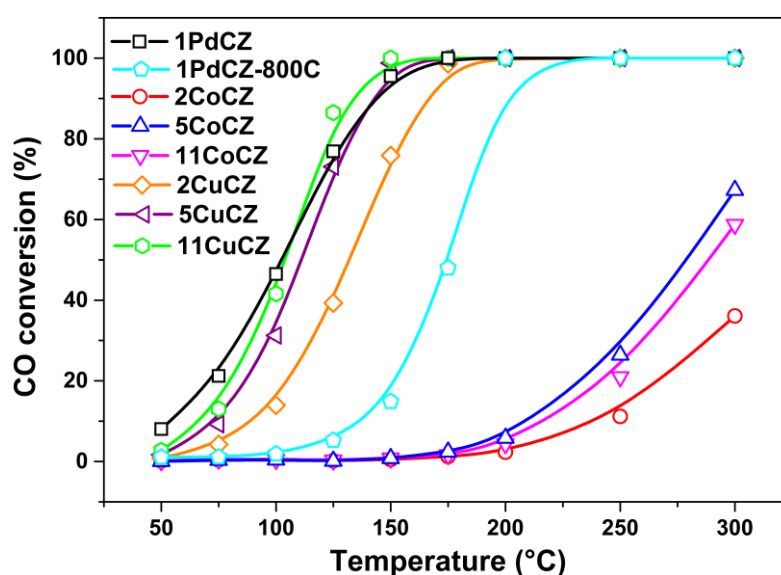

Figure 3.14: CO conversion curves for Pd-doped and Pd-free catalysts.

As with the CO + NO reaction, the Co samples show negligible activity for the CO oxidation reaction. The increase in CO conversion observed for temperatures higher than 150 °C can be mainly attributed to the direct reaction of CO with gas phase O_2. These results differ substantially with those from other research groups that found high CO activities for Co-based catalysts [243–245]. As previously mentioned in the discussion of the CO + NO reaction, the reason for this discrepancy is most likely that Co oxide clusters are the active phase for CO oxidation, as demonstrated by these research groups. Conversely, in our case only Co^{2+} ions are present, as shown by XPS measurements in Chapter 2. This assumption is also confirmed in the previous chapter by EXAFS data showing that isolated Co species could be obtained by our method. Finally, this result indicates the potential benefits that these catalysts can have in other applications where exclusively Co^{2+} ions are needed, since in reality often the mixed valence Co oxides such as typical Co_3O_4 are present.

In contrast to Co, the Cu-based samples perform significantly better in the CO oxidation reaction. It can be seen in Figure 3.14 that the CO conversion increases with the Cu loading, and that noble metal-free 11CuCZ can compete with 1PdCZ in terms of CO oxidation activity. This can be explained by the fact that more Cu^+ ions might be present on the surface when the Cu loading is increased. In particular, Cu^+ ions appear to be highly active in this reaction related to the strong chemisorption of CO [246,247]. In the previous chapter, XPS measurements have confirmed the presence of Cu^+ along with Cu^{2+} ions. It has previously been shown that these Cu^+ ions can easily regenerate by interacting with the Ce^{3+} ions from the support [69]. A second reason could be the higher amount of oxygen vacancies being formed upon doping with a higher amount of Cu. It has been shown earlier that these vacancies can play an important role in redox reactions [146,181].

XPS measurements previously showed that the Pd in 1PdCZ-800C is still highly dispersed and that a significant amount had segregated to the surface of the support. Hence, it was presumed that a higher amount of highly dispersed surface Pd for 1PdCZ-800C compared to 1PdCZ could lead to a higher catalytic activity. However, it can be seen from Figure 3.14 that 1PdCZ-800C performs significantly worse than 1PdCZ in the CO + O_2 reaction. This result can be explained by DRIFTS, where it was shown that more reduced Pd clusters and less single-atomic species are present for 1PdCZ-800C than for 1PdCZ. Conclusively, single-atomic and highly oxidized Pd^{2+} seems to be more effective in oxidizing CO than less dispersed, reduced Pd clusters or species. However, it should be noted that the lower surface area of 1PdCZ-800C (12 m^2/g) compared to 1PdCZ (71 m^2/g) might also play a role in the activity difference.
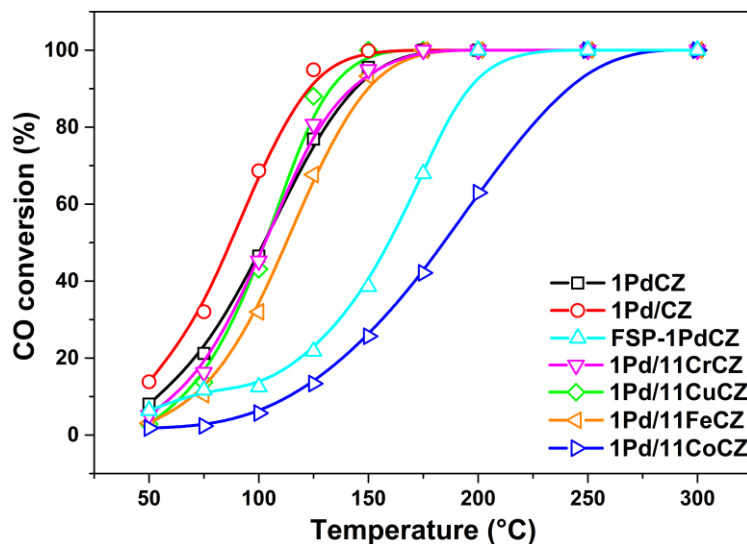
Figure 3.15: CO conversion curves for transition metal-doped ceria-zirconia supports impregnated with Pd. The activity is compared with one-step synthesized 1PdCZ.

As a next step, differently doped ceria-zirconia supports were impregnated with Pd (1 wt.%) and their catalytic activities were tested and compared with that of 1PdCZ. The CO oxidation activity of flame spray pyrolysis (FSP) synthesized 1PdCZ with a Ce:Zr ratio of 0.7:0.3 (FSP-1PdCZ) was also tested for comparison with sol-gel synthesized 1PdCZ. FSP is a well-established aerosol technique for the synthesis of homogenous an high surface area nanoparticles in a single step [248]. Hence, it is expected that FSP-made ceria-zirconia-based catalysts display higher activities than the conventional wet-chemistry synthesized catalysts with lower surface areas. The experimental procedure for synthesizing FSP-1PdCZ is described in detail in the Supporting Information.

Figure 3.15 shows that the Co-based catalysts perform significantly worse than the other transition metal based catalysts, even though the addition of Pd enhanced its activity at both low and high temperatures. Secondly, it was also observed that the activity of 11CuCZ did not increase after impregnation with Pd. Similar activities of 11CuCZ and 1Pd/11CuCZ for the oxidation of CO could be explained by the high Cu loading that might lead to the segregation of a significant amount of Cu species to the surface of the support, which was shown by XPS. Consequently, when Cu is in the very surface of the support, it does not allow Pd to interact efficiently with ceria-zirconia. As there are strong indications that the Pd-CeO_2 interface plays an active role in redox reactions, it may follow that the activity will not change significantly after Pd is deposited on Cu rather than on CeO_2 [249–251]. Moreover, the CO oxidation activity might even decrease when Pd is covering the active Cu^+ species. This reasoning might explain why no change in catalytic activity was observed after adding Pd to 11CuCZ, despite the high activity that is typically observed for Pd-based catalysts in oxidation reactions.

Despite the fact that for 1PdCZ a considerable amount of Pd might be present in the bulk of the support, a relatively high activity could still be observed for this catalyst compared to the Pd-impregnated catalysts. This observation further confirms that a strong interaction between Pd and CeO_2 might promote the CO oxidation. More specifically, a strong metal-support

interaction might facilitate oxygen transfer from the support to the noble metal, leading to a higher reduction and oxidation rate [252]. This assumption is also in line with the H_2-TPR experiments from the previous chapter that showed an exceptionally high H_2/Pd ratio (7.1) for 1PdCZ compared to 1Pd/CZ (1.5).

Surprisingly, it was found that FSP-1PdCZ performed significantly worse than sol-gel synthesized 1PdCZ, despite the former catalyst showing a much higher surface area (150 m^2/g) than the latter (71 m^2/g). However, XRD measurements (see Supporting Information) showed that the phase homogeneity of FSP-1PdCZ was much lower than that of sol-gel synthesized 1PdCZ, which could partially explain the activity difference. This result is further discussed in more detail in the Supporting Information.

The higher CO conversion observed for 1Pd/CZ compared to 1PdCZ can be explained by the former's higher amount of surface palladium atoms available for catalyzing the oxidation of CO. This is confirmed by XPS analysis showing a slightly higher intensity of the Pd^{2+} peak for 1Pd/CZ in Chapter 2. The reason why some research groups observe higher activities for noble metal ionic catalysts than for noble metal impregnated catalysts might be due to the formation of noble metal clusters or particles after the impregnation of the support. Consequently, the Pd atoms inside the bulk of these clusters and particles cannot participate in the catalytic reactions, leading to a corresponding decrease in the catalytic activity. Furthermore, the larger the size of these particles, the weaker the interaction with the reducible support becomes, leading to a loss of the promoting effect of CeO_2 on Pd for the oxidation of CO [97,253]. In our case, XPS showed that the binding energy of Pd in 1Pd/CZ is 337.4 eV, indicating that part of the Pd might also be present in the typical agglomerated PdO. Despite this finding, the CO oxidation activity of 1Pd/CZ was still higher than 1PdCZ, as shown in Figure 3.15. Thus, it was hypothesized that the amount of highly dispersed Pd in 1Pd/CZ is still enough to maintain the reaction, since XPS also showed that most of the Pd is on the surface for 1Pd/CZ.

Finally, it can be seen from Figure 3.15 that 1Pd/CZ performs better in the CO oxidation reaction than 1Pd/11MCZ (M = transition metal), as was previously also observed for the CO + NO reaction. The low-temperature activities of the Pd-impregnated samples are summarized in Table 3.6 and compared with the low-temperature activity of 1PdCZ.

Table 3.6: CO conversions at 50 °C for 1PdCZ and Pd-impregnated samples.

Sample	CO conversion (%) at T = 50°C
1PdCZ	8.0
1Pd/CZ	13.8
1Pd/11CoCZ	1.8
1Pd/11CuCZ	2.8
1Pd/11FeCZ	3.1
1Pd/11CrCZ	5.1

At first sight these results might seem counterintuitive, as it is often speculated in the literature that a higher amount of oxygen vacancies or a higher reducibility leads to a higher activity. However, to the best of our knowledge it seems that there is no simple descriptor for this, as a higher reducibility found by H_2-TPR does not necessarily mean a higher activity towards CO oxidation. CO-TPR, on the other hand, could shed more light on this, as it might imply directly the interaction with CO and thus also the reactivity. Hence, the activity towards CO oxidation cannot be concluded only from the H_2-TPR measurements, and therefore more experiments are needed to gain more insight into the active phase for the CO + O_2 reaction.

It was concluded from the XPS spectra of the Pd3d regions in Chapter 2 that more Pd is on the surface for 1Pd/11MCZ than for 1Pd/CZ, yet the former catalysts exhibit lower activities for the oxidation of CO than 1Pd/CZ. This is in line with the results observed for the CO + NO reaction, where it was assumed that for high dopant concentrations the dopant might modify the interface between Pd and CeO_2. Therefore, it can be concluded that the Pd-Ce interface might also strongly influence the final catalytic activity in the CO + O_2 reaction.
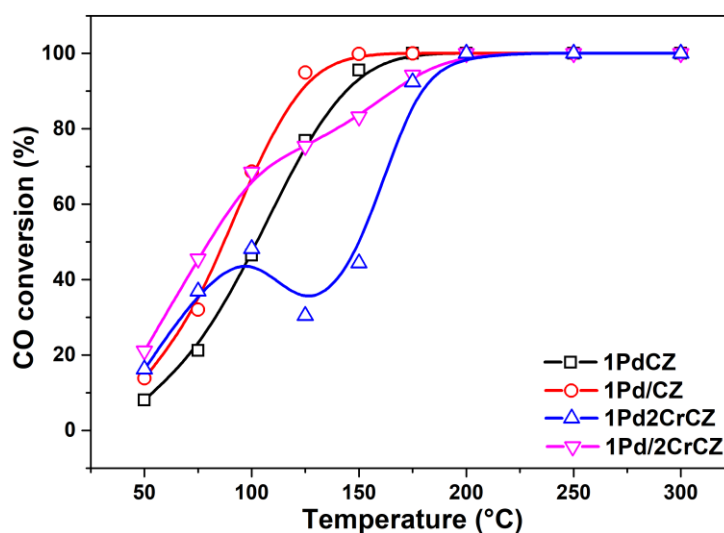
Figure 3.16: CO conversion curves for Pd-only and Pd-Cr based catalysts.

The catalytic activity tests showed that doping the support with a high concentration transition metal does not necessarily increase the low-temperature or overall activity. Therefore, it was decided to prepare 1Pd/xMCZ and 1PdxMCZ with a lower transition metal dopant concentration to investigate the effect of the dopant loading on the activity. As with the CO + NO reaction, the main focus was put on Cr, as 1Pd/11CrCZ showed a slightly higher activity than the other transition metals used for doping. Finally, the CO oxidation activities of 1Pd/2CrCZ and 1Pd2CrCZ were compared with those of 1Pd/CZ and 1PdCZ in Figure 3.16.

At least two important observations can be made from Figure 3.16. Firstly, doping with a lower amount of Cr increased the low-temperature activity significantly. More specifically, CO conversions of 16.2% and 21.1% at 50 °C were achieved for 1Pd2CrCZ and 1Pd/2CrCZ, respectively, while the CO conversion for 1Pd/11CrCZ was only 5.1% at the same temperature. Secondly, higher CO conversions were obtained for the Pd-impregnated samples than for the

one-step synthesized samples, which is the opposite of what has been observed for the CO + NO reaction.

The improved catalytic activity observed for 1Pd/2CrCZ compared to 1Pd/11CrCZ could be explained by the fact that for an excessively high dopant concentration the dopant ions might be located in the surface or subsurface of the support, thereby not allowing the Pd to occupy surface sites where it can actively participate in the oxidation of CO. This is also consistent with the XPS results, which showed that the dopant ions tend to segregate to the surface, except for Fe. Furthermore, XPS also showed that the Pd in 1Pd2CrCZ and 1Pd/2CrCZ is atomically dispersed (BE > 337.7 eV), while the Pd in 1Pd/11CrCZ is in the form of bulk Pd oxide (BE = 337.2 eV). Indeed, it has been shown in literature that single atoms may show improved catalytic activities due to a more favorable interaction with the reducible support and a more efficient use of the noble metal [254]. However, these XPS results should be interpreted with caution. From DRIFTS measurements it was observed that the presence of Cr in 1Pd/5CrCZ makes the Pd more stable towards sintering or clustering. In contrast to this, XPS analysis showed that the Pd in 1Pd/5CrCZ is present in the form of clusters. As DRIFTS measurements are in general more sensitive to structural and electronic effects, the XPS results on its own cannot explain the catalytic activity trends. Thus, the explanation for the observed phenomena is not fully clear, and further studies are needed to gain more insight into the observed activity trends.

The higher CO oxidation activity observed for the Pd-impregnated samples than for the Pd-doped samples was simply attributed to the higher amount of Pd atoms on the surface of the impregnated CZ supports. This reasoning is consistent with the literature, where it has been extensively reported that Pd is particularly active in oxidation reactions. Therefore, it can be concluded that the amount of Pd on the surface of the catalyst plays a more important role in the CO + O_2 reaction than in the CO + NO reaction due to its intrinsically higher activity for oxidation reactions. In other words, for the CO oxidation reaction even Pd alone supported on the ceria-zirconia can provide low-temperature activity. In turn, for the efficient NO reduction the presence of the oxygen vacancies induced by doping as well as the electronic interaction with the dopant itself appears to be needed. However, as previously demonstrated, the importance of the Pd-Ce interface in the CO + O_2 reaction should not be overlooked, although it seems to play an even more important role in the CO + NO reaction.

Table 3.7: CO conversions and turnover frequencies (TOF) at T = 50 °C. TOF values were normalized by the amount of Pd determined by ICP-OES.

Sample	CO conversion (%) at T = 50 °C	TOF (s^{-1}) at T = 50 °C
1PdCZ	8.0	0.05
1Pd/CZ	13.8	0.09
1Pd2CrCZ	16.2	0.10
1Pd/2CrCZ	21.1	0.14

Finally, Figure 3.16 and Table 3.7 show that 1Pd/2CrCZ, and even 1Pd2CrCZ, display a higher CO oxidation activity at low temperatures than 1Pd/CZ. This observation can be attributed to three main factors. The first factor implies the formation of more defects in the proximity of Pd when a small aliovalent cation is incorporated in the lattice of the CZ support. These defects might facilitate the migration of lattice oxygen to Pd, and hence it can be concluded that this mechanism might play an important role in the oxidation of CO at low temperatures. The elongated M-O bonds that are formed after doping could also improve the oxygen release properties of the catalyst. In summary, the higher amount of oxygen vacancies available at low temperatures and the enhanced oxygen mobility after doping might explain why 1Pd/2CrCZ is performing better than 1Pd/CZ in the low temperature region. This could also be the reason why 1Pd2CrCZ displays a higher low-temperature activity than 1Pd/CZ, despite the fact that the former catalyst has less Pd atoms available on its surface for catalyzing the oxidation of CO. However, derived from the H_2-TPR experiments, Pd-only 1PdCZ showed superior oxygen storage/release properties, yet it performs worse than 1Pd2CrCZ and 1Pd/2CrCZ in the low-temperature region. Therefore, there should be another reason for the improved low-temperature activity of 1Pd2CrCZ and 1Pd/2CrCZ. Several studies have demonstrated the high activity of Cr in the oxidation reactions of volatile organic compounds (VOCs) [72,73]. Therefore, it could be that the intrinsic oxidation activity of Cr (or more specifically Cr^{6+}, as demonstrated by these studies) might also partially explain the improved catalytic activities of 1Pd/2CrCZ and 1Pd2CrCZ compared to 1Pd/CZ.

The third and the final factor affecting the CO oxidation activity might be a synergistic interaction taking place between Cr and Pd. The existence of such an interaction was previously demonstrated by DRIFTS, where a higher stability of highly dispersed Pd was observed. Besides, this effect was already explained in more detail in the results and discussion section of the CO + NO reaction.

As it was demonstrated that high CO conversions can be obtained with Pd-Cr based catalysts, additional samples were prepared with varying metal loadings and with either Pd or Cr impregnated on the surface. The idea of impregnating the supports with Cr was inspired by previous works of Harrison et al. and Yoshida et al., who co-impregnated CeO_2 supports with Cu and Cr resulting in significant CO conversions after thermally aging the catalysts at high temperatures [255,256]. The high conversions were explained by the formation of a binary oxide between Cu and Cr after thermally aging in which the Cu was present in the form of the active Cu^+ species. To our knowledge, only one study has explored the effect of combining Pd and Cr on the CO oxidation activity [205]. In this study, Fernández-García et al. reported the formation of a Pd(I)-Cr(III) mixed oxide phase after calcination when Pd and Cr were co-impregnated on Al_2O_3. It was observed that the formation of this phase enhanced the CO oxidation activity considerably, while the NO reduction activity decreased.

Finally, the Pd-Cr based catalysts were subjected to three consecutive $CO + O_2$ catalytic activity tests. The details of each test are described in the experimental section of this chapter. It was expected that after running the reaction several times the Pd chemical state might change, leading to a corresponding change in the CO oxidation activity. Afterwards, more insight into the active phase could then be gained by characterizing the chemical state of Pd in the spent

catalysts by XPS and DRIFTS. The results of the catalytic activity testing are shown in Figure 3.17.
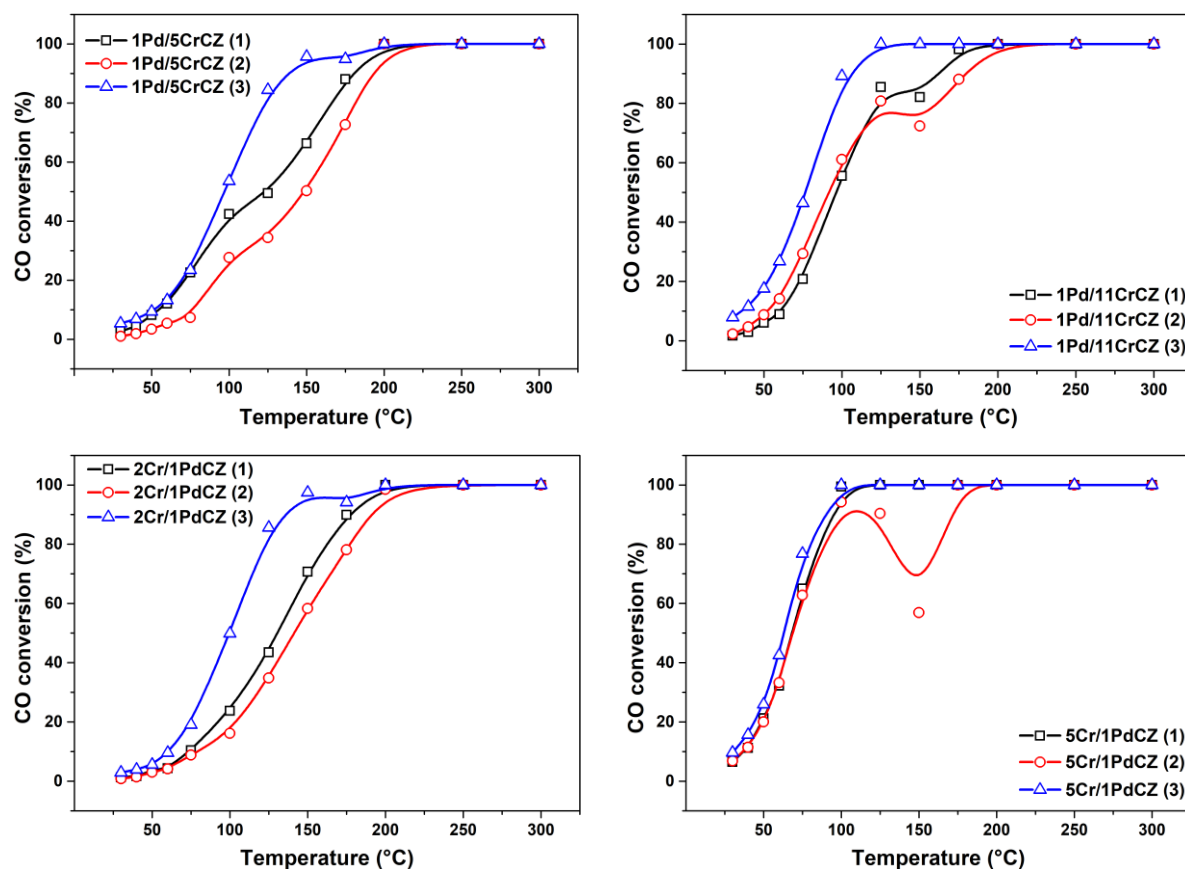

Figure 3.17: CO conversion curves for Pd-Cr based catalysts. The CO oxidation activity increased for all catalysts in the third catalytic activity test.

Figure 3.17 shows that for the second run without reoxidation the CO conversion values decrease for all catalysts, except for 1Pd/11CrCZ in the low-temperature region. For the third run, however, after reoxidizing the catalysts, a notable increase in the CO conversion values can be seen. It might be that in the course of the reaction a Pd-Cr mixed oxide phase was formed that can enhance the CO oxidation reactivity of Pd, as was previously also reported by Fernández-García et al [205]. XPS analysis showed that for the spent catalysts significantly more Cr had segregated to the surface. This could suggest that upon the segregation of Cr to the surface, more of these favorable mixed oxides phases could be formed with Pd, explaining the observed increase in the activity. Additionally, XPS also showed that for 2Cr/1PdCZ-AR and 5Cr/1PdCZ-AR the Pd was still highly dispersed, which is consistent with the DRIFTS results. For the Pd-impregnated samples, on the other hand, the DRIFTS results were not in line with the XPS results. Nevertheless, it was speculated that the Pd-Cr mixed oxide phase can be active in the CO oxidation as well as in keeping the Pd in a highly dispersed form according to DRIFTS.

To further confirm that a Pd-Cr mixed oxide phase was formed, fresh Pd-Cr based catalysts were also subjected to three consecutive CO + NO catalytic activity tests. Fernández-García et

al. showed that the mixed oxide phase could enhance the CO oxidation activity, while it appeared to be detrimental for the reduction of NO [205]. In agreement with their observation, the catalytic activity tests showed that the NO conversion efficiency significantly decreased for the third run (see Supporting Information). Thus, it can finally be concluded that most likely in our case a Pd-Cr mixed oxide phase was also formed during the reaction. The slight increase in the NO conversion observed for 5Cr/1PdCZ, however, could not be explained.

4. Conclusions

To conclude, in this chapter we investigated the catalytic activity of noble metal-free and Pd-based ceria-zirconia samples towards the CO + NO and CO + O$_2$ reactions. It was observed that one-step synthesized samples performed significantly better in the CO + NO reaction than Pd-impregnated samples, while the opposite was found to be true for the CO + O$_2$ reaction. The improved NO reduction activity for the one-step synthesized samples was explained by the more intimate Pd-Ce contact that can be achieved after co-doping of the support with the noble metal. In this way, the noble metal is located in close proximity to the oxygen vacancies created by the transition metal dopant. As both the noble metal and oxygen vacancies play a crucial role in the reduction of NO, the catalytic activity can be significantly increased when these two active phases are in close proximity to each other. In addition, it was shown by DRIFTS that synergistic effects between Pd and the transition metal (Cr and Fe) could also lead to the high activity observed for the 1Pd2CrCZ, 1Pd5CrCZ and 1Pd11FeCZ samples. The single peak at 2157 cm^{-1} observed in the IR spectra of the Cr/Pd-based sample has not yet been reported in the literature to our knowledge, and it indicates that Cr prevents the formation or sintering of Pd clusters. The DRIFTS measurements further suggest that a highly oxidized Pd state, as in the Cr-based samples and in 1Pd11FeCZ, is needed to achieve high NO conversion efficiencies.

The improved CO oxidation activity of the Pd-impregnated samples compared to the Pd-doped samples was explained by the former's higher amount of surface Pd species that can catalyze the oxidation of CO. However, it was concluded that the Pd-Ce interface in these samples might also affect the overall catalytic activity for the CO + O$_2$ reaction. This was evidenced by the similar activities observed for 11CuCZ and 1Pd/11CuCZ. The segregation of the dopant ions to the surface for a higher dopant concentration, as demonstrated by XPS, does not allow Pd to occupy sites on the CZ support where it can actively participate in the CO oxidation reaction. Further, although XPS showed that more surface Pd species were present for 1PdCZ-800C than for 1PdCZ, a lower CO oxidation activity was observed for the former catalyst. This was explained by the lower surface area of the calcined sample and the presence of more reduced Pd species on its surface, as evidenced by DRIFTS. Finally, the increased CO oxidation activity observed for the Pd-Cr samples after subjecting them to three consecutive catalytic activity tests was attributed to the formation of a Pd-Cr mixed oxide phase. Apparently, the formation of this mixed phase is beneficial for the oxidation of CO, while it appears to be detrimental for the reduction of NO. This reasoning is further supported by previously reported studies on the Pd-Cr-based catalyst, where the formation of this mixed phase was evidenced by EPR and XANES experiments.

Acknowledgements

For almost eight months, I've had the honor to work in an enjoyable, supportive and professional research group, and I would like to take the opportunity to thank the people who were involved in my graduation project.

Most importantly I want to thank Valerii, my direct supervisor, for his great support and advice throughout the project. You were always available for helping me out in the lab when needed, and you could always answer my questions quickly and thoroughly. The many papers that you sent me were very helpful for writing my thesis, and you taught me to keep remaining critical about the statements made in the literature. I also want to thank you for taking over the high-throughput experiments when I could not be at the university, and I'm very grateful that you could measure some of the samples I prepared at the synchrotron facilities. Finally, you have helped me to become a better researcher, and working together with you on this project was a great experience that I will never forget.

Further, I want to thank prof. Hensen for giving me the opportunity to work in his research group. Your valuable insights during our meetings helped me with focusing on the most important parts of the project. Of course, I also want to thank prof. Hofmann for the very constructive discussions we had. The suggestions you made during these discussions helped me to improve this work, and you were always available whenever I had questions about the project. Additionally, I want to thank prof. Noël for showing his interest in my graduation project and to join the committee.

I also specifically want to thank Alexander Parastaev for the use of his sol-gel synthesis procedure, and for explaining me how to work with several of the characterization techniques that I used in this project. Additionally, I want to thank Bianca for the effective collaboration, and for the many interesting discussions we had on our closely related projects. I also want to thank all other members of the IMC group for their kindness and great help.

Finally, I would like to thank my parents and brother for continuously supporting me. Their encouragement was endless, and bringing this project to a successful end would not have been possible without their help.

Supporting Information

Chapter 2

1. Thermal stability of Pd-doped ceria-zirconia

Doping of ceria-zirconia with different transition metal dopants resulted in a change of the color of the support. These color changes were often a clear indication whether phase segregation occurred after the calcination at 800 °C. For example, bare $CeZrO_4$ and 1PdCZ powders calcined at 500, 800 and 900 °C are shown in Figure S1.
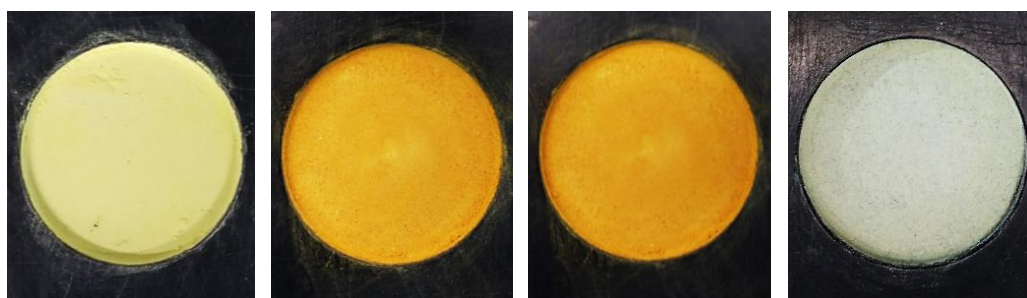

Figure S1: Pictures of sol-gel synthesized $CeZrO_4$, 1PdCZ, 1PdCZ-800C and 1PdCZ-900C.

After doping $CeZrO_4$ with 1 wt.% Pd, the color changed from pale yellow to orange, as can be seen from the first and second picture in Figure S1. Calcining 1PdCZ at 800 °C did not result in the formation of bulk PdO or Pd^0, as evidenced by XRD. This could also be derived from the same color that 1PdCZ-800C (picture 3) displayed compared with 1PdCZ. Calcining the sample at 900 °C, however, resulted in the formation of Pd^0 as was revealed by XRD. Indeed, this result was already predicted beforehand based on the significant color change of the sample from orange to broken white.

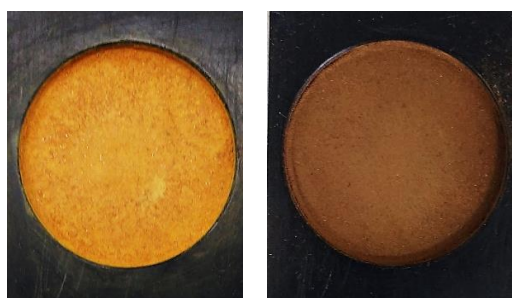**Figure S2**: Pictures of sol-gel synthesized 5PdCZ (left) and 5PdCZ-800C (right).

In contrast to 1PdCZ, a color change was observed for 5PdCZ from orange to dark brown after calcining the sample at 800 °C, as shown in Figure S2. Hence, it was assumed that bulk PdO must have been formed upon the calcination, and this was indeed confirmed by XRD showing a reflection peak around 56° corresponding to (112) PdO.

Chapter 3

1. X-ray Diffraction (XRD)

XRD measurements were performed for some of the Pd-Cr-based catalysts. These results are shown in Figure S3.
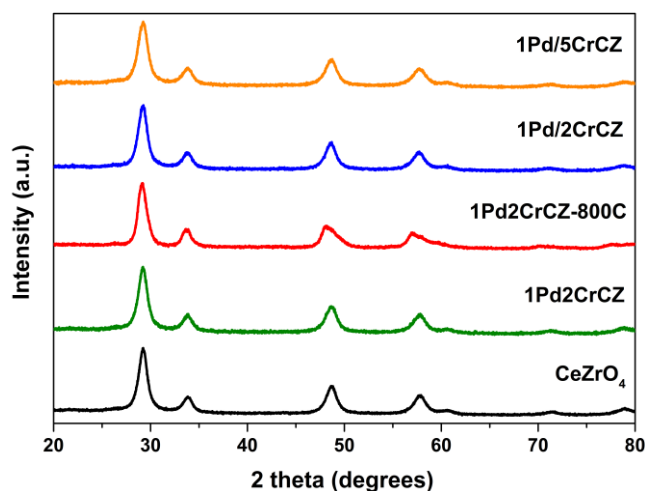
Figure S3: XRD patterns of pure CeZrO$_4$ and Pd-Cr-based catalysts.

No reflection peaks corresponding to a segregated Cr or Pd oxide phase were observed for any of the catalysts. Despite the fact that the crystal lattice of the ceria-zirconia support must be significantly distorted after co-doping with Pd and Cr, no partial peak splitting due to a CeO$_2$-ZrO$_2$ phase separation was observed for 1Pd2CrCZ calcined at 800 °C. However, the asymmetric shape of the reflection peaks at higher diffraction angles indicates that further increasing the temperature will most likely result in the abovementioned phase separation.

Ceria-zirconia supports were also co-doped with Pd and Cu, as it was shown in the literature that promising results can be obtained for the reduction of NO by using Cu-based ceria catalysts. Moreover, Yoshida et al. reported that high NO conversions could be achieved by using a combination of Cu and Cr due to the formation of a favorable mixed phase after calcination at high temperatures [256]. Therefore, Pd, Cu and Cr triple-doped ceria-zirconia (1Pd2Cu2CrCZ) was also prepared, and its thermal stability was tested by XRD after calcining the sample at 800 °C. These results are shown in Figure S4.
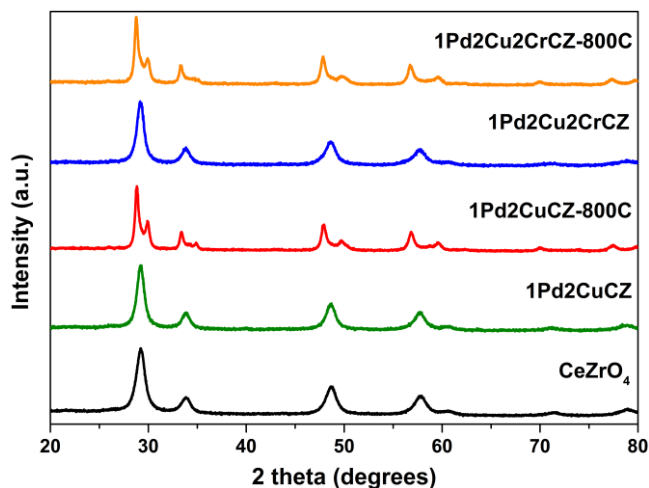
Figure S4: XRD patterns of pure CeZrO$_4$, 1Pd2CuCZ and 1Pd2Cu2CrCZ calcined at different temperatures.

Figure S4 shows that 1Pd2CuCZ and 1Pd2Cu2CrCZ are not stable at 800 °C due to the formation of a CeO$_2$- and ZrO$_2$-rich phase. This is in line with the findings in Chapter 2, where it was shown that a phase separation even occurs for ceria-zirconia single-doped with 2.77 mol% Cu. Nevertheless, no segregated Pd, Cu or Cr oxide phases were observed in the XRD patterns. Furthermore, the XRD pattern of 1Pd2Cu2CrCZ indicates that the fluorite type lattice of the ceria-zirconia support can accommodate a significant amount of aliovalent transition metal dopants with different ionic radii, without leading to disintegration of the crystal lattice at 500 °C. However, since the overall thermal stability is an important factor to prolong the lifetime of the catalyst, we decided to narrow down our focus to the Pd-Cr-based catalysts which showed higher thermal stability compared to the other transition metal-doped catalysts.

2. TEM analysis

TEM images were taken for some of the Pd-Cr-based catalysts, and these results are shown in Figure S5.
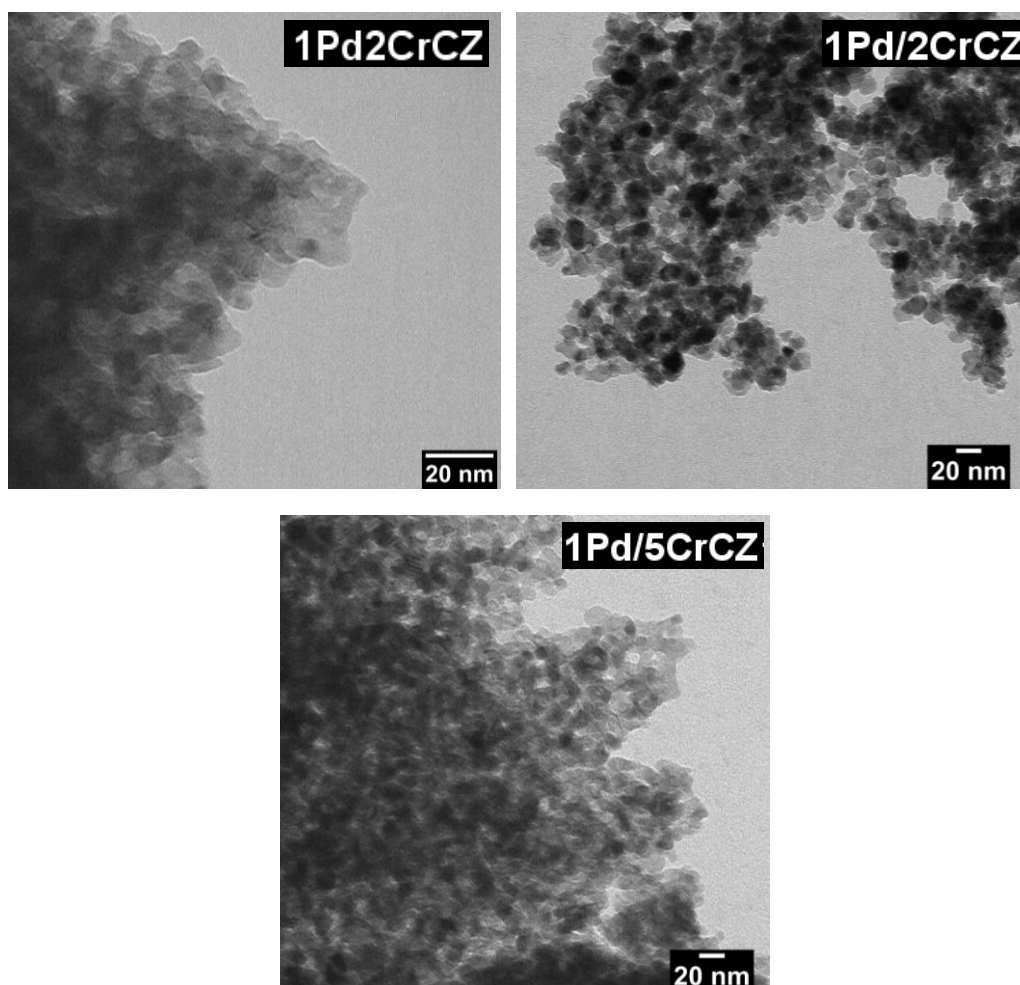
Figure S5: TEM images of Pd-Cr based catalysts.

Figure S5 shows that nanometer-sized particles could be obtained via the polymer-assisted sol-gel method, and which are responsible for the broad peaks observed in the XRD patterns shown in Figure S3. No segregated Pd or Cr oxide phases were visible in these images, which is consistent with the XRD measurements. However, it should be noted that Pd or Cr oxide clusters might be present, but which are too small or finely dispersed to be seen by TEM or to be detected by XRD.

3. BET surface area and ICP-OES

Table S1 shows the BET surface area (m^2/g) and Pd, Cr and Fe weight loadings as determined by ICP-OES analysis of some of the catalysts tested in the CO oxidation and NO reduction reactions. The actual metal loadings were close to the theoretical loadings.

Table S1: BET surface area (m^2/g) and Pd, Cr and Fe weight loadings as determined by ICP-OES analysis. The theoretical weight loading of Pd in all samples was 1 wt.%.

Sample	BET surface area (m^2/g)	wt. % Cr or Fe (theoretical)	wt. % Cr or Fe (ICP)	wt. % Pd (ICP)
1PdCZ	71	/	/	0.948 ± 0.013
1Pd/CZ	61	/	/	0.979 ± 0.013
1Pd2CrCZ	66	0.990	0.996 ± 0.063	0.968 ± 0.013
1Pd/2CrCZ	50	0.990	1.00 ± 0.01	0.9333 ± 0.013
1Pd/11CrCZ	80	4.176	4.06 ± 0.01	0.922 ± 0.013
1Pd5FeCZ	63	2.156	2.19 ± 0.05	0.961 ± 0.013
1Pd11FeCZ	73	4.440	4.38 ± 0.05	0.907 ± 0.013

It was observed from Table S1 that the surface areas of 1Pd/2CrCZ (50 m^2/g) and 1Pd/11CrCZ (80 m^2/g) were lower than these of 2CrCZ (62 m^2/g) and 11CrCZ (87 m^2/g) reported in Chapter 2. These results appear to be logical, as Pd deposited on the surface might block and cover the pores and adsorption sites for the probe molecule (N_2) resulting in a lower surface area that can be measured by N_2 physisorption.

4. Flame Spray Pyrolysis (FSP)

4.1 Experimental

FSP-CeZrO$_4$ and FSP-Ce$_{0.7}$Zr$_{0.3}$O$_2$ was synthesized with a Tethis NPS10 FSP setup. Ce(acac)$_3$ (acac = acetylacetonate; Sigma Aldrich, 99.9% purity) and Zr(acac)$_4$ (Sigma Aldrich, 97% purity) were dissolved in a 1:1 (w/w) mixture of glacial acetic acid and lauric acid with the appropriate precursor amount to obtain Ce:Zr ratios of 1:1 and 0.7:0.3. In addition, different total metal precursor concentrations (0.1 M and 0.2 M) were also used. The precursors were dissolved in the solvent mixture under stirring on a heating plate at 80 °C. The solution was injected through a syringe in the nozzle of the FSP setup at a flow rate of 5 ml/min. The flame was fed with a 1.5 L/min (STP) methane flow and a 3.0 L/min (STP) oxygen flow. An additional 5.0 L/min (STP) oxygen dispersion flow was also used, and the overpressure was kept at 2.5 bar. The same procedure was used for synthesizing FSP-Ce$_{0.7}$Zr$_{0.3}$O$_2$ doped with 1 wt.% Pd (FSP-1PdCZ), simply adding Pd(acac)$_2$ (Sigma Aldrich, 99%) to the solvent mixture in the first step of the synthesis procedure.

4.2 X-ray Diffraction (XRD)

The XRD patterns of the FSP-synthesized samples were measured and compared with the XRD pattern of sol-gel synthesized $CeZrO_4$. These results are shown in Figure S6.
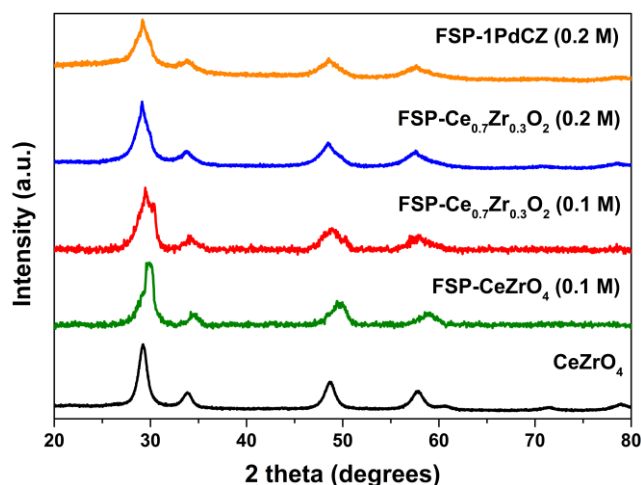

Figure S6: XRD patterns of $CeZrO_4$, FSP-$Ce_{1-x}Zr_xO_2$ and FSP-1PdCZ using different metal precursor concentrations and Ce:Zr ratios.

It can be seen from the figure that sol-gel-synthesized $CeZrO_4$ exhibited superior phase homogeneity compared to the FSP-synthesized ceria-zirconia samples. Using a total metal precursor concentration of 0.1 M for preparing FSP-$CeZrO_4$ resulted in an extremely low phase homogeneity, as can be derived from the partial peak splitting due to the formation of a CeO_2- and ZrO_2-rich phase. It was found that decreasing the Zr dopant concentration to 30 mol% and increasing the metal precursor concentration to 0.2 M could improve the phase homogeneity significantly. The small shoulder that is still visible indicates the phase separation of a small amount of ZrO_2 from CeO_2. Furthermore, this shoulder was also visible for FSP-1PdCZ. Hence, this could explain why FSP-1PdCZ performs worse than the sol-gel synthesized 1PdCZ in the $CO + O_2$ reaction. However, attributing this difference solely to the lower phase homogeneity might not fully explain this result. Thus, more investigation is needed to establish the reason for this activity difference. Promising results have already been obtained for FSP-CeO_2 using 2-ethylhexanoic acid as the solvent in combination with glacial acetic acid, and therefore the use of this solvent mixture can only be seen as a logical next step for synthesizing highly homogeneous $CeZrO_4$ with FSP.

5. Catalyst stability tests

5.1 CO + NO reaction

The stability of some of the key samples was investigated by probing their NO reduction activity for three consecutive catalytic activity tests. Before the first and the third run, the samples were pretreated by calcining them *in situ* for 2h at 300 °C in a 25/75 (v/v) O_2/He flow. No pretreatment was used for the second run. The NO conversion curves for the different catalysts are shown in Figure S7.

96
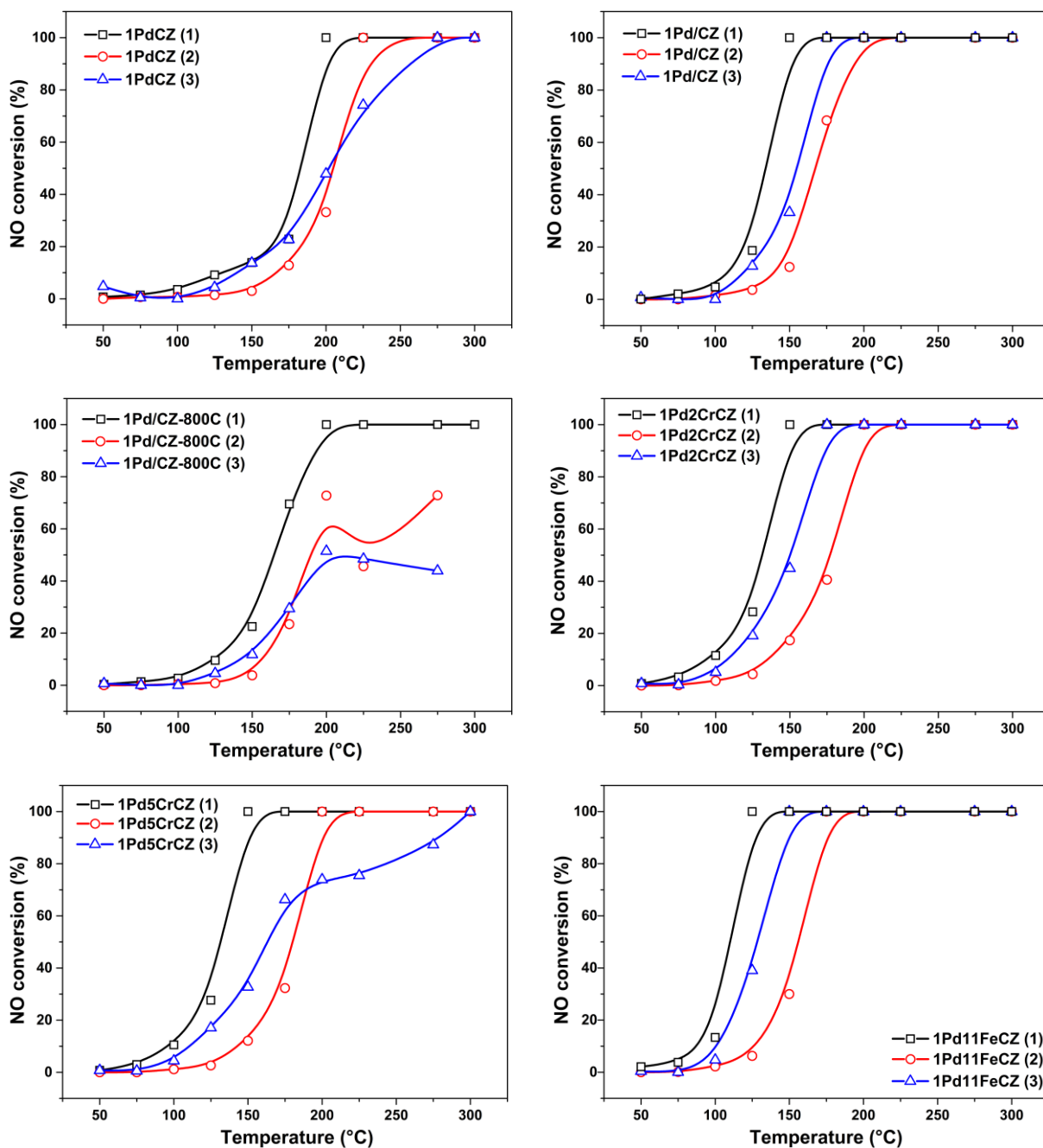
Figure S7: Catalyst stability tests for the Pd-, Cr- and Fe-based catalysts.

Figure S7 shows that the NO reduction activity decreases significantly for the second run. Pretreating the samples after the second run could not restore the initial catalytic activity. In Chapter 3, we speculated that for the Pd-Cr-based catalysts a Pd-Cr mixed oxide phase was formed during the reaction process which is favorable for the CO oxidation, but detrimental for the NO reduction. For 1Pd2CrCZ, it is difficult to conclude whether this phase was formed during the process, as it shows a similar stability behavior as 1Pd/CZ and 1Pd11FeCZ. For 1Pd5CrCZ, however, a concave feature was observed around 175 °C, and this could mean several things. One possibility is that a lattice disintegration or CeO_2-ZrO_2 phase separation has occurred, which is plausible considering the high Cr dopant concentration that is used.

Alternatively, it could be that a Pd-Cr mixed oxide phase was formed, which is more favorable to occur in 1Pd5CrCZ than in 1Pd2CrCZ due to its higher Cr dopant concentration. Finally, it was observed that the catalytic activity of 1Pd/CZ-800C decreased significantly for the second and third run. This could be attributed to the deactivation of the active noble metal phase by severe sintering or clustering into a new phase that is less active for the reduction of NO.

5.2 CO + O$_2$ reaction

The catalyst stability was also investigated for the Pd-Cr-based samples that showed high activity for the CO + O$_2$ reaction. These results were already shown in Chapter 3 (Figure 3.17). Additionally, the CO oxidation activity of these samples was also probed after first testing them two times in the CO + NO reaction, for which the reaction conditions are slightly more reducing than for the CO + O$_2$ reaction due to the absence of gas phase oxygen. The results of this stability test are shown in Figure S8.
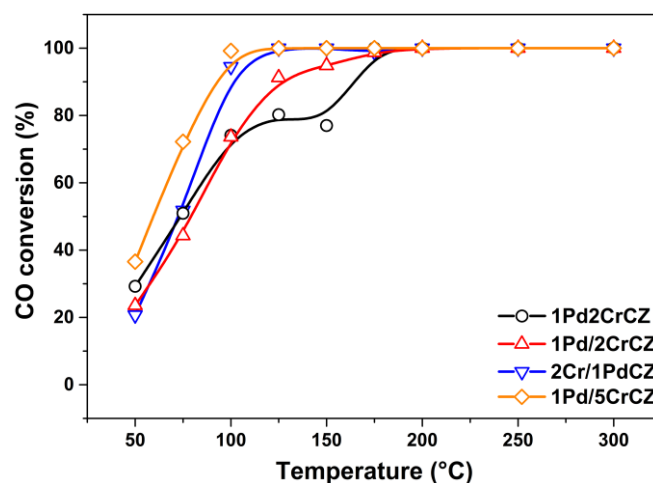
Figure S8: Catalyst stability test for Pd-Cr-based catalysts after 2x CO + NO .

It can be seen from the figure that the catalysts show exceptionally high CO oxidation activity after they were first tested in the CO + NO reaction. All catalysts displayed a CO conversion higher than 20% at 50 °C. Further, it was observed that the catalyst with the highest Cr dopant concentration (1Pd/5CrCZ) showed the highest CO oxidation activity. Therefore, it can be concluded that the presence of Cr can enhance the activity towards the oxidation of CO. However, it should also be noted that the presence of more oxygen vacancies in 1Pd/5CrCZ compared to 1Pd/2CrCZ can also positively influence the oxidation of CO. Further, it was assumed that the slightly more reducing conditions of the CO + NO reaction could somehow favor the formation of a Pd-Cr mixed phase, which could then explain the high CO conversions observed in the CO + O$_2$ reaction. On the other hand, these results should be interpreted carefully. Attributing the enhanced CO oxidation solely to the formation of more Pd-Cr mixed oxide might not fully explain the enormous difference compared to the activity of the same catalysts reported in Chapter 3, where the formation of the mixed oxide was also suggested.

References

[1]   Morad M 2014 *Development of new highly active nano gold catalysts for selective oxidation reactions*

[2]   Erkens I J M 2014 Understanding and controlling atomic layer deposition of platinum and platinum oxide

[3]   Fernández J L, Walsh D A and Bard A J 2005 Thermodynamic guidelines for the design of bimetallic catalysts for oxygen electroreduction and rapid screening by scanning electrochemical microscopy. M− Co (M: Pd, Ag, Au) *J. Am. Chem. Soc.* **127** 357–65

[4]   Engel T and Ertl G 1978 A molecular beam investigation of the catalytic oxidation of CO on Pd (111) *J. Chem. Phys.* **69** 1267–81

[5]   Li J, Liu X, Zhan W, Guo Y, Guo Y and Lu G 2016 Preparation of high oxygen storage capacity and thermally stable ceria–zirconia solid solution *Catal. Sci. Technol.* **6** 897–907

[6]   Trovarelli A and Llorca J 2017 Ceria Catalysts at Nanoscale: How Do Crystal Shapes Shape Catalysis? *ACS Catal.* **7** 4716–35

[7]   Anon, Surfaces of metal oxides 2015 @ https://www.slideshare.net/SBPMat/surfaces-of-metal-oxides

[8]   Shinjoh H, Hatanaka M, Nagai Y, Tanabe T, Takahashi N, Yoshida T and Miyake Y 2009 Suppression of noble metal sintering based on the support anchoring effect and its application in automotive three-way catalysis *Top. Catal.* **52** 1967–71

[9]   Nagai Y, Hirabayashi T, Dohmae K, Takagi N, Minami T, Shinjoh H and Matsumoto S 2006 Sintering inhibition mechanism of platinum supported on ceria-based oxide and Pt-oxide-support interaction *J. Catal.* **242** 103–9

[10]   Shelef M and McCabe R W 2000 Twenty-five years after introduction of automotive catalysts: what next? *Catal. Today* **62** 35–50

[11]   Twigg M V. 2007 Progress and future challenges in controlling automotive exhaust gas emissions *Appl. Catal. B Environ.* **70** 2–15

[12]   Guillén Hurtado N, Rico Pérez V, Garcia-Garcia A, Lozano Castelló D and Bueno López A 2012 Three-way catalysts: past, present and future

[13]   Gandhi H S, Piken A G, Shelef M and Delosh R G 1976 Laboratory evaluation of three-way catalysts *SAE Trans.* 901–12

[14]   Heck R M and Farrauto R J 2001 Automobile exhaust catalysts **221** 443–57

[15]   Dvořák F, Camellone M F, Tovt A, Tran N-D, Negreiros F R, Vorokhta M, Skála T, Matolínová I, Mysliveček J and Matolín V 2016 Creating single-atom Pt-ceria catalysts by surface step decoration *Nat. Commun.* **7** 10801

[16]   Jones J, Xiong H, DeLaRiva A T, Peterson E J, Pham H, Challa S R, Qi G, Oh S, Wiebenga M H and Hernández X I P 2016 Thermally stable single-atom platinum-on-ceria catalysts via atom trapping *Science (80-.).* **353** 150–4

[17]   She Y, Zheng Q, Li L, Zhan Y, Chen C, Zheng Y and Lin X 2009 Rare earth oxide modified CuO/CeO2 catalysts for the water–gas shift reaction *Int. J. Hydrogen Energy* **34** 8929–36

[18]   Muhammed M 1998 Total Oxidation of Methane Over Doped Nanophase Cerium Oxides Total oxidation of methane over doped nanophase cerium oxides

[19]   Fornasiero P, Graziani M and Kas J 1999 Use of CeO2-based oxides in the three-way catalysis **50**

[20]   Gandhi H S, Graham G W and Mccabe R W 2003 Automotive exhaust catalysis **216** 433–42

[21]   Graham G W, Potter T, Baird R J, Gandhi H S and Shelef M 1986 Surface composition of polycrystalline Pd15Rh following high temperature oxidation in air *J. Vac. Sci. Technol. A Vacuum, Surfaces, Film.* **4** 1613–6

[22]   Muraki H, Shinjoh H and Fujitani Y 1986 Effect of lanthanum on the NO reduction over palladium catalysts *Appl. Catal.* **22** 325–35

[23]   Murota T, Hasegawa T, Aozasa S, Matsui H and Motoyama M 1993 Production method of cerium oxide with high storage capacity of oxygen and its mechanism *J. Alloys Compd.* **193** 298–9

[24]   Baidya T, Bera P, Mukri B D, Parida S K, Kröcher O, Elsener M and Hegde M S 2013 DRIFTS studies on CO and NO adsorption and NO+ CO reaction over Pd2+-substituted CeO2 and Ce0. 75Sn0. 25O2 catalysts *J. Catal.* **303** 117–29

[25]   Portmann R W, Daniel J S and Ravishankara A R 2012 Stratospheric ozone depletion due to nitrous oxide: Influences of other gases *Philos. Trans. R. Soc. B Biol. Sci.* **367** 1256–64

[26]   Ravishankara AR, Daniel JS and Portmann RW 2009 Nitrous oxide (N2O): the dominant ozone-depleting substance emitted in the 21st century *Science (80-.).* **326** 123–125

[27]   Bouwman L, Daniel J S, Davidson E A, de Klein C, Holland E, Ju X, Kanter D, Oenema O, Ravishankara A R and Skiba U M 2013 *Drawing down N2O to protect climate and the ozone layer. A UNEP Synthesis Report* (United Nations Environment Programme (UNEP))

[28]   Konsolakis M 2015 Recent Advances on Nitrous Oxide (N2O) Decomposition over Non-Noble-Metal Oxide Catalysts: Catalytic Performance, Mechanistic Considerations, and Surface Chemistry Aspects *ACS Catal.* **5** 6397–421

[29]   Wang Y, Oord R, van den Berg D, Weckhuysen B M and Makkee M 2017 Oxygen Vacancies in Reduced Rh/ and Pt/Ceria for Highly Selective and Reactive Reduction of NO into N2 in excess of O2 *ChemCatChem* **9** 2935–8

[30]   Yao X, Tang C and Dong L 2014 Catalysis Science & Technology over supported metal-oxide catalysts 2814–29

[31]   Grzybowska-Świerkosz B 2000 Thirty years in selective oxidation on oxides: what have we learned? *Top. Catal.* **11** 23–42

[32]   Ren Y, Ma Z and Bruce P G 2012 Ordered mesoporous metal oxides: synthesis and applications *Chem. Soc. Rev.* **41** 4909–27

[33]   Trifiro F 1998 The chemistry of oxidation catalysts based on mixed oxides *Catal. today* **41** 21–35

[34]   Yuan C, Wu H Bin, Xie Y and Lou X W 2014 Mixed transition-metal oxides: design, synthesis, and energy-related applications *Angew. Chemie Int. Ed.* **53** 1488–504

[35]   Gawande M B, Pandey R K and Jayaram R V 2012 Role of mixed metal oxides in catalysis science—versatile applications in organic synthesis *Catal. Sci. Technol.* **2** 1113–25

[36]   Yakovlev A L, Zhidomirov G M and Santen R A Van 2001 N 2 O decomposition catalysed by transition metal ions **75** 45–8

[37]   Stambouli A B and Traversa E 2002 Solid oxide fuel cells (SOFCs): a review of an environmentally clean and efficient source of energy *Renew. Sustain. energy Rev.* **6** 433–55

100

[38]   Liu J, Dai M, Wang T, Sun P, Liang X, Lu G, Shimanoe K and Yamazoe N 2016 Enhanced gas sensing properties of SnO2 hollow spheres decorated with CeO2 nanoparticles heterostructure composite materials *ACS Appl. Mater. Interfaces* **8** 6669–77

[39]   Chen C-Y and Liu C-L 2011 Doped ceria powders prepared by spray pyrolysis for gas sensing applications *Ceram. Int.* **37** 2353–8

[40]   Escribano V S, López E F, Panizza M, Resini C, Amores J M G and Busca G 2003 Characterization of cubic ceria–zirconia powders by X-ray diffraction and vibrational and electronic spectroscopy *Solid State Sci.* **5** 1369–76

[41]   Piumetti M, Andana T, Bensaid S, Russo N, Fino D and Pirone R 2016 Study on the CO oxidation over ceria-based nanocatalysts *Nanoscale Res. Lett.* **11** 165

[42]   Gruy F and Pijolat M 1994 Kinetics of CeO2 Surface Area Reduction in a Mixture of HCl, H2O, and O2 *J. Am. Ceram. Soc.* **77** 1537–44

[43]   Perrichon V, Laachir A, Abouarnadasse S, Touret O and Blanchard G 1995 Thermal stability of a high surface area ceria under reducing atmosphere *Appl. Catal. A Gen.* **129** 69–82

[44]   R. M. Heck and R. J. Farrauto, Van Nostrand Reinhold 1995 *Catalytic air pollution control: commercial technology* (New York (N.Y.), USA)

[45]   Yashima M, Arashi H, Kakihana M and Yoshimura M 1994 Raman Scattering Study of Cubic–Tetragonal Phase Transition in Zr1−xCexO2 Solid Solution *J. Am. Ceram. Soc.* **77** 1067–71

[46]   Trovarelli A 1999 Structural and Oxygen Storage/Release Properties of CeO2-Based Solid Solutions *Comments Inorg. Chem.* **20** 263–84

[47]   Trovarelli A and Fornasiero P 2013 *Catalysis by ceria and related materials* vol 12 (World Scientific)

[48]   Vlaic G, Fornasiero P, Geremia S, Kašpar J and Graziani M 1997 Relationship between the Zirconia-Promoted Reduction in the Rh-Loaded Ce0.5Zr0.5O2Mixed Oxide and the Zr–O Local Structure *J. Catal.* **168** 386–92

[49]   Fornasiero P, Dimonte R, Rao G R, Kaspar J, Meriani S, Trovarelli A-0307 and Graziani M 1995 Rh-loaded CeO2-ZrO2 solid-solutions as highly efficient oxygen exchangers: dependence of the reduction behavior and the oxygen storage capacity on the structural-properties *J. Catal.* **151** 168–77

[50]   Wang H-F, Gong X-Q, Guo Y-L, Guo Y, Lu G Z and Hu P 2009 A model to understand the oxygen vacancy formation in Zr-doped CeO2: electrostatic interaction and structural relaxation *J. Phys. Chem. C* **113** 10229–32

[51]   Trovarelli A, Leitenburg C de and Dolcetti G 1997 Design better cerium-based oxidation catalysts *Chemtech* **27**

[52]   Cuif J-P, Blanchard G, Touret O, Seigneurin A, Marczi M and Quéméré E 1997 *(Ce, Zr) O2 solid solutions for three-way catalysts* (SAE Technical Paper)

[53]   Kaspar J, Fornasiero P, Balducci G, Di Monte R, Hickey N and Sergo V 2003 Effect of ZrO2 content on textural and structural properties of CeO2–ZrO2 solid solutions made by citrate complexation route *Inorganica Chim. Acta* **349** 217–26

[54]   Sun Y and Sermon P A 1996 Surface reactivity and bulk properties of ZrO2. Part 2.—Importance of homogeneity in the stabilisation of high surface area CeO2–ZrO2 aerogels *J. Mater. Chem.* **6** 1025–9

[55]   Rohart E, Larcher O, Deutsch S, Hedouin C, Aimin H, Fajardie F, Allain M and Macaudiere P 2004 From Zr-rich to Ce-rich: thermal stability of OSC materials on the whole range of

composition *Top. Catal.* **30** 417–23

[56]   Egami T, Dmowski W and Brezny R 1997 *Characterization of the Local Structure of CeO2/ZrO2 by Pulsed Neutron Scattering* (SAE Technical Paper)

[57]   Devaiah D, Reddy L H, Park S E and Reddy B M 2018 Ceria–zirconia mixed oxides: Synthetic methods and applications *Catal. Rev. - Sci. Eng.* **60** 177–277

[58]   Ranga Rao G, Kaspar J, Meriani S, Monte R di and Graziani M 1994 NO decomposition over partially reduced metallized CeO2-ZrO2 solid solutions *Catal. Letters* **24** 107–12

[59]   de Leitenburg C, Trovarelli A, Llorca J, Cavani F and Bini G 1996 The effect of doping CeO2 with zirconium in the oxidation of isobutane *Appl. Catal. A Gen.* **139** 161–73

[60]   Ozawa M, Kimura M and Isogai A 1993 The application of Ce☐ Zr oxide solid solution to oxygen storage promoters in automotive catalysts *J. Alloys Compd.* **193** 73–5

[61]   Balducci G, Fornasiero P, Di Monte R, Kaspar J, Meriani S and Graziani M 1995 An unusual promotion of the redox behaviour of CeO 2-ZrO 2 solid solutions upon sintering at high temperatures *Catal. Letters* **33** 193–200

[62]   Nagarajan V S and Rao K J 1992 Characterization of sol-gel derived zirconia with additions of yttria and ceria. Origin of high fracture toughness in ceria-stabilized samples *Philos. Mag. A* **65** 771–81

[63]   Liang Q, Wu X, Weng D and Lu Z 2008 Selective oxidation of soot over Cu doped ceria/ceria–zirconia catalysts *Catal. Commun.* **9** 202–6

[64]   Li S, Wang N, Yue Y, Wang G, Zu Z and Zhang Y 2015 Copper doped ceria porous nanostructures towards a highly efficient bifunctional catalyst for carbon monoxide and nitric oxide elimination *Chem. Sci.* **6** 2495–500

[65]   Saranya J, Ranjith K S, Saravanan P, Mangalaraj D and Rajendra Kumar R T 2014 Cobalt-doped cerium oxide nanoparticles: Enhanced photocatalytic activity under UV and visible light irradiation *Mater. Sci. Semicond. Process.* **26** 218–24

[66]   Tan Q, Du C, Sun Y, Du L, Yin G and Gao Y 2014 Nickel-doped ceria nanoparticles for promoting catalytic activity of Pt/C for ethanol electrooxidation *J. Power Sources* **263** 310–4

[67]   Li G, Wang Q, Zhao B, Shen M and Zhou R 2011 Effect of iron doping into CeO2–ZrO2 on the properties and catalytic behaviour of Pd-only three-way catalyst for automotive emission control *J. Hazard. Mater.* **186** 911–20

[68]   Pachatouridou E, Papista E, Delimitis A, Vasiliades M A, Efstathiou A M, Amiridis M D, Alexeev O S, Bloom D, Marnellos G E, Konsolakis M and Iliopoulou E 2016 N2O decomposition over ceria-promoted Ir/Al2O3 catalysts: The role of ceria *Appl. Catal. B Environ.* **187** 259–68

[69]   Konsolakis M, Carabineiro S A C, Papista E, Marnellos G E, Tavares P B, Moreira J A, Romaguera-Barcelay Y and Figueiredo J L 2015 Effect of preparation method on the solid state properties and the deN2O performance of CuO–CeO2 oxides *Catal. Sci. Technol.* **5** 3714–27

[70]   Ilieva L, Pantaleo G, Ivanov I, Zanella R, Venezia A M and Andreeva D 2009 A comparative study of differently prepared rare earths-modified ceria-supported gold catalysts for preferential oxidation of CO *Int. J. Hydrogen Energy* **34** 6505–15

[71]   Papavasiliou J, Avgouropoulos G and Ioannides T 2007 Effect of dopants on the performance of CuO–CeO2 catalysts in methanol steam reforming *Appl. Catal. B Environ.* **69** 226–34

[72]   Aranzabal A, González-marcos M P, González-marcos J A, López-fonseca R and González-velasco J R 2014 State of the art in catalytic oxidation of chlorinated volatile organic compounds

68 1169–86

[73]   Yang P, Yang S, Shi Z, Meng Z and Zhou R 2015 Applied Catalysis B : Environmental Deep oxidation of chlorinated VOCs over CeO2-based transition metal mixed oxide catalysts "*Applied Catal. B, Environ.* **162** 227–35

[74]   Myers S J, Ball D J, Ciosek S M, Doud J M, Schaffer J C and Turek A G 1999 Advancements in Converter Durability to Enable Close Mounted Converters for Stringent Emissions Regulations

[75]   Collins N R, Chandler G R, Brisley R J, Andersen P J, Shady P J and Roth S A 1996 *Catalyst improvements to meet European Stage III and ULEV emissions criteria* (SAE Technical Paper)

[76]   Saurat M and Bringezu S 2008 Platinum group metal flows of Europe, part I: Global supply, use in industry, and shifting of environmental impacts *J. Ind. Ecol.* **12** 754–67

[77]   Xin Y, Wang H and Law C K 2014 Kinetics of catalytic oxidation of methane, ethane and propane over palladium oxide *Combust. Flame* **161** 1048–54

[78]   Toso A, Colussi S, Llorca J and Trovarelli A 2019 The dynamics of PdO-Pd phase transformation in the presence of water over Si-doped Pd/CeO2 methane oxidation catalysts *Appl. Catal. A Gen.* **574** 79–86

[79]   Colussi S, Gayen A, Farnesi Camellone M, Boaro M, Llorca J, Fabris S and Trovarelli A 2009 Nanofaceted Pd☐O Sites in Pd☐Ce Surface Superstructures: Enhanced Activity in Catalytic Combustion of Methane *Angew. Chemie Int. Ed.* **48** 8481–4

[80]   Beck D D, Sommers J W and DiMaggio C L 1997 Axial characterization of oxygen storage capacity in close-coupled lightoff and underfloor catalytic converters and impact of sulfur *Appl. Catal. B Environ.* **11** 273–90

[81]   Graham G W, Jen H-W, Chun W and McCabe R W 1999 High-temperature-aging-induced encapsulation of metal particles by support materials: comparative results for Pt, Pd, and Rh on cerium–zirconium mixed oxides *J. Catal.* **182** 228–33

[82]   Xu, Q. , Kharas, K. C., Croley, B. J. and Datye A K 2011 The Sintering of Supported Pd Automotive Catalysts *ChemCatChem* **3** 1004–14

[83]   Adijanto L, Bennett D A, Chen C, Yu A S, Cargnello M, Fornasiero P, Gorte R J and Vohs J M 2013 Exceptional thermal stability of Pd@ CeO2 core–shell catalyst nanostructures grafted onto an oxide surface *Nano Lett.* **13** 2252–7

[84]   Tauster S J, Fung S C and Garten R L 1978 Strong metal-support interactions. Group 8 noble metals supported on titanium dioxide *J. Am. Chem. Soc.* **100** 170–5

[85]   Kašpar J, Fornasiero P and Hickey N 2003 Automotive catalytic converters: current status and some perspectives *Catal. Today* **77** 419–49

[86]   Spezzati G, Su Y, Hofmann J P, Benavidez A D, DeLaRiva A T, McCabe J, Datye A K and Hensen E J M 2017 Atomically Dispersed Pd–O Species on CeO2 (111) as Highly Active Sites for Low-Temperature CO Oxidation *ACS Catal.* **7** 6887–91

[87]   Qiao B, Liang J-X, Wang A, Liu J and Zhang T 2016 Single atom gold catalysts for low-temperature CO oxidation *Chinese J. Catal.* **37** 1580–6

[88]   Yang M, Li S, Wang Y, Herron J A, Xu Y, Allard L F, Lee S, Huang J, Mavrikakis M and Flytzani-Stephanopoulos M 2014 Catalytically active Au-O (OH) x-species stabilized by alkali ions on zeolites and mesoporous oxides *Science (80-.).* **346** 1498–501

[89]   Lang R, Li T, Matsumura D, Miao S, Ren Y, Cui Y, Tan Y, Qiao B, Li L and Wang A 2016 Hydroformylation of olefins by a rhodium single-atom catalyst with activity comparable to RhCl

(PPh3) 3 *Angew. Chemie Int. Ed.* **55** 16054–8

[90] Sun Q, Dai Z, Liu X, Sheng N, Deng F, Meng X and Xiao F-S 2015 Highly Efficient Heterogeneous Hydroformylation over Rh-Metalated Porous Organic Polymers: Synergistic Effect of High Ligand Concentration and Flexible Framework *J. Am. Chem. Soc.* **137** 5204–9

[91] Vilé G, Albani D, Nachtegaal M, Chen Z, Dontsova D, Antonietti M, López N and Pérez-Ramírez J 2015 A Stable Single-Site Palladium Catalyst for Hydrogenations *Angew. Chemie Int. Ed.* **54** 11265–9

[92] Corma A, Salnikov O G, Barskiy D A, Kovtunov K V and Koptyug I V 2015 Single-Atom Gold Catalysis in the Context of Developments in Parahydrogen-Induced Polarization *Chem. Eur. J.* **21** 7012–5

[93] Xing J, Chen J F, Li Y H, Yuan W T, Zhou Y, Zheng L R, Wang H F, Hu P, Wang Y and Zhao H J 2014 Stable isolated metal atoms as active sites for photocatalytic hydrogen evolution *Chem. Eur. J.* **20** 2138–44

[94] Cheng N, Stambula S, Wang D, Banis M N, Liu J, Riese A, Xiao B, Li R, Sham T-K and Liu L-M 2016 Platinum single-atom and cluster catalysis of the hydrogen evolution reaction *Nat. Commun.* **7** 13638

[95] Wang L, Huang L, Liang F, Liu S, Wang Y and Zhang H 2017 Preparation, characterization and catalytic performance of single-atom catalysts *Chinese J. Catal.* **38** 1528–39

[96] Su Y-Q, Liu J-X, Filot I A W and Hensen E J M 2017 Theoretical Study of Ripening Mechanisms of Pd Clusters on Ceria *Chem. Mater.* **29** 9456–62

[97] Farmer J A and Campbell C T 2010 Ceria maintains smaller metal catalyst particles by strong metal-support bonding *Science (80-.).* **329** 933–6

[98] Wang R, Gardner J A, Evenson W E and Sommers J A 1993 Oxygen-vacancy complexes in cerium oxide studied by $^{111}\mathrm{In}$ time-differential perturbed-angular-correlation spectroscopy *Phys. Rev. B* **47** 638–51

[99] Addou R, Senftle T P, O'Connor N, Janik M J, van Duin A C T and Batzill M 2014 Influence of Hydroxyls on Pd Atom Mobility and Clustering on Rutile TiO2(011)-2 × 1 *ACS Nano* **8** 6321–33

[100] Hegde M S and Bera P 2015 Noble metal ion substituted CeO2 catalysts: Electronic interaction between noble metal ions and CeO2 lattice *Catal. Today* **253** 40–50

[101] O'Neill B J, Jackson D H K, Lee J, Canlas C, Stair P C, Marshall C L, Elam J W, Kuech T F, Dumesic J A and Huber G W 2015 Catalyst design with atomic layer deposition *Acs Catal.* **5** 1804–25

[102] Sun S, Zhang G, Gauquelin N, Chen N, Zhou J, Yang S, Chen W, Meng X, Geng D and Banis M N 2013 Single-atom catalysis using Pt/graphene achieved through atomic layer deposition *Sci. Rep.* **3** 1775

[103] Li G, Li L, Yuan Y, Shi J, Yuan Y, Li Y, Zhao W and Shi J 2014 Highly efficient mesoporous Pd/CeO2catalyst for low temperature CO oxidation especially under moisture condition *Appl. Catal. B Environ.* **158**–**159** 341–7

[104] Bisht A, Gangwar B P, Anupriya T and Sharma S 2014 Understanding the electrochemical differences of Pt doped and Pt supported over CeO2 *J. Solid State Electrochem.* **18** 197–206

[105] Wang B, Weng D, Wu X and Fan J 2010 Influence of H2/O2 redox treatments at different temperatures on Pd-CeO2 catalyst: Structure and oxygen storage capacity *Catal. Today* **153** 111–7

[106]   Trusova E A, Khrushcheva A A and Vokhmintcev K V 2012 Sol–gel synthesis and phase composition of ultrafine ceria-doped zirconia powders for functional ceramics *J. Eur. Ceram. Soc.* **32** 1977–81

[107]   Liotta L F, Macaluso A, Longo A, Pantaleo G, Martorana A and Deganello G 2003 Effects of redox treatments on the structural composition of a ceria–zirconia oxide for application in the three-way catalysis *Appl. Catal. A Gen.* **240** 295–307

[108]   Hajizadeh-Oghaz M, Shoja Razavi R and Ghasemi A 2015 Synthesis and characterization of ceria–yttria co-stabilized zirconia (CYSZ) nanoparticles by sol–gel process for thermal barrier coatings (TBCs) applications *J. Sol-Gel Sci. Technol.* **74** 603–12

[109]   Le Gal A, Abanades S and Flamant G 2011 CO2 and H2O Splitting for Thermochemical Production of Solar Fuels Using Nonstoichiometric Ceria and Ceria/Zirconia Solid Solutions *Energy & Fuels* **25** 4836–45

[110]   Si R, Zhang Y-W, Li S-J, Lin B-X and Yan C-H 2004 Urea-Based Hydrothermally Derived Homogeneous Nanostructured Ce1-xZrxO2 (x = 0−0.8) Solid Solutions: A Strong Correlation between Oxygen Storage Capacity and Lattice Strain *J. Phys. Chem. B* **108** 12481–8

[111]   Rodriguez J A, Hanson J C, Kim J-Y, Liu G, Iglesias-Juez A and Fernández-García M 2003 Properties of CeO2 and Ce1-xZrxO2 Nanoparticles: X-ray Absorption Near-Edge Spectroscopy, Density Functional, and Time-Resolved X-ray Diffraction Studies *J. Phys. Chem. B* **107** 3535–43

[112]   Brinker C J and Scherer G W 2013 *Sol-gel science: the physics and chemistry of sol-gel processing* (Academic press)

[113]   Rossignol S, Madier Y and Duprez D 1999 Preparation of zirconia–ceria materials by soft chemistry *Catal. Today* **50** 261–70

[114]   Gash A E, Tillotson T M, Satcher J H, Poco J F, Hrubesh L W and Simpson R L 2001 Use of Epoxides in the Sol−Gel Synthesis of Porous Iron(III) Oxide Monoliths from Fe(III) Salts *Chem. Mater.* **13** 999–1007

[115]   Danks A E, Hall S R and Schnepp Z 2016 The evolution of 'sol–gel'chemistry as a technique for materials synthesis *Mater. Horizons* **3** 91–112

[116]   Ravel B and Newville M 2005 ATHENA, ARTEMIS, HEPHAESTUS: data analysis for X-ray absorption spectroscopy using IFEFFIT *J. Synchrotron Radiat.* **12** 537–41

[117]   Bozo C, Gaillard F and Guilhaume N 2001 Characterisation of ceria–zirconia solid solutions after hydrothermal ageing *Appl. Catal. A Gen.* **220** 69–77

[118]   Montini T, Melchionna M, Monai M and Fornasiero P 2016 Fundamentals and Catalytic Applications of CeO2-Based Materials *Chem. Rev.* **116** 5987–6041

[119]   Zhenhua G, Xiuli S, Hua W and Kongzhai L 2014 Structure and catalytic property of CeO2-ZrO2-Fe2O3 mixed oxide catalysts for diesel soot combustion: Effect of preparation method *J. Rare Earths* **32** 817–23

[120]   Gu Z, Li K, Qing S, Zhu X, Wei Y, Li Y and Wang H 2014 Enhanced reducibility and redox stability of Fe2O3 in the presence of CeO2 nanoparticles *RSC Adv.* **4** 47191–9

[121]   Liang C, Ma Z, Lin H, Ding L, Qiu J, Frandsen W and Su D 2009 Template preparation of nanoscale CexFe1−xO2 solid solutions and their catalytic properties for ethanol steam reforming *J. Mater. Chem.* **19** 1417–24

[122]   Mukherjee D, Rao B G and Reddy B M 2016 CO and soot oxidation activity of doped ceria: Influence of dopants *Appl. Catal. B Environ.* **197** 105–15

[123]   Wang X, Rodriguez J A, Hanson J C, Gamarra D, Martínez-Arias A and Fernández-García M 2005 Unusual Physical and Chemical Properties of Cu in Ce1-xCuxO2 Oxides *J. Phys. Chem. B* **109** 19595–603

[124]   Pino L, Vita A, Cipitì F, Lagana M and Recupero V 2008 Catalytic performance of Ce 1− x Ni x O 2 catalysts for propane oxidative steam reforming *Catal. Letters* **122** 121–30

[125]   Barrio L, Kubacka A, Zhou G, Estrella M, Martínez-Arias A, Hanson J C, Fernández-García M and Rodriguez J A 2010 Unusual Physical and Chemical Properties of Ni in Ce1−xNixO2−y Oxides: Structural Characterization and Catalytic Activity for the Water Gas Shift Reaction *J. Phys. Chem. C* **114** 12689–97

[126]   Bera P, Priolkar K R, Sarode P R, Hegde M S, Emura S, Kumashiro R and Lalla N P 2002 Structural Investigation of Combustion Synthesized Cu/CeO2 Catalysts by EXAFS and Other Physical Techniques: Formation of a Ce1-xCuxO2-δ Solid Solution *Chem. Mater.* **14** 3591–601

[127]   Luo J-Y, Meng M, Yao J-S, Li X-G, Zha Y-Q, Wang X and Zhang T-Y 2009 One-step synthesis of nanostructured Pd-doped mixed oxides MOx-CeO2 (M=Mn, Fe, Co, Ni, Cu) for efficient CO and C3H8 total oxidation *Appl. Catal. B Environ.* **87** 92–103

[128]   Wang X, Rodriguez J A, Hanson J C, Gamarra D, Martínez-Arias A and Fernández-García M 2006 In Situ Studies of the Active Sites for the Water Gas Shift Reaction over Cu−CeO2 Catalysts: Complex Interaction between Metallic Copper and Oxygen Vacancies of Ceria *J. Phys. Chem. B* **110** 428–34

[129]   Shan W, Shen W and Li C 2003 Structural Characteristics and Redox Behaviors of Ce1-xCuxOy Solid Solutions *Chem. Mater.* **15** 4761–7

[130]   Hočevar S, Krašovec U O, Orel B, Aricó A S and Kim H 2000 CWO of phenol on two differently prepared CuO–CeO2 catalysts *Appl. Catal. B Environ.* **28** 113–25

[131]   Bao H, Chen X, Fang J, Jiang Z and Huang W 2008 Structure-activity relation of Fe 2 O 3–CeO 2 composite catalysts in CO oxidation *Catal. Letters* **125** 160–7

[132]   Pérez-Alonso F J, López Granados M, Ojeda M, Terreros P, Rojas S, Herranz T, Fierro J L G, Gracia M and Gancedo J R 2005 Chemical Structures of Coprecipitated Fe−Ce Mixed Oxides *Chem. Mater.* **17** 2329–39

[133]   Wen Q-Y, Zhang H-W, Song Y-Q, Yang Q-H, Zhu H and Xiao J Q 2007 Room-temperature ferromagnetism in pure and Co doped CeO2 powders *J. Phys. Condens. Matter* **19** 246205

[134]   Hegde M S, Madras G and Patil K C 2009 Noble Metal Ionic Catalysts *Acc. Chem. Res.* **42** 704–12

[135]   Shannon R D 1976 Revised effective ionic radii and systematic studies of interatomic distances in halides and chalcogenides *Acta Crystallogr. Sect. A Cryst. physics, diffraction, Theor. Gen. Crystallogr.* **32** 751–67

[136]   Scanlon D O, Morgan B J and Watson G W 2011 The origin of the enhanced oxygen storage capacity of Ce 1− x (Pd/Pt) x O 2 *Phys. Chem. Chem. Phys.* **13** 4279–84

[137]   Hiley C I, Fisher J M, Thompsett D, Kashtiban R J, Sloan J and Walton R I 2015 Incorporation of square-planar Pd 2+ in fluorite CeO 2: hydrothermal preparation, local structure, redox properties and stability *J. Mater. Chem. A* **3** 13072–9

[138]   HUANG M, WANG S, LI L, ZHANG H, SHI Z and CHEN Y 2017 Effect of high temperature pretreatment on the thermal resistance properties of Pd/CeO2/Al2O3 close-coupled catalysts *J. Rare Earths* **35** 149–57

[139]   Crist B V 2005 Handbooks of Monochromatic XPS Spectra. Volume 2—Commercially pure binary oxides *XPS Int. LLC, Mt. View*

[140]   Nelson A E and Schulz K H 2003 Surface chemistry and microstructural analysis of CexZr1−xO2−y model catalyst surfaces *Appl. Surf. Sci.* **210** 206–21

[141]   Shang D, Cai W, Zhao W, Bu Y and Zhong Q 2014 Catalytic Oxidation of NO to NO2 Over Co–Ce–Zr Solid Solutions: Enhanced Performance of Ce–Zr Solid Solution by Co *Cat. Letters* **144** 538–44

[142]   Moretti E, Storaro L, Talon A, Riello P, Molina A I and Rodríguez-Castellón E 2015 3-D flower like Ce–Zr–Cu mixed oxide systems in the CO preferential oxidation (CO-PROX): Effect of catalyst composition *Appl. Catal. B Environ.* **168–169** 385–95

[143]   Ghodselahi T, Vesaghi M A, Shafiekhani A, Baghizadeh A and Lameii M 2008 XPS study of the Cu@Cu2O core-shell nanoparticles *Appl. Surf. Sci.* **255** 2730–4

[144]   Cai W, Zhong Q, Zhang S and Zhang J 2013 Effects of Cr on the NO oxidation over the ceria–zirconia solid solution *RSC Adv.* **3** 7009–15

[145]   Grosvenor A P, Biesinger M C, Smart R S C and McIntyre N S 2006 New interpretations of XPS spectra of nickel metal and oxides *Surf. Sci.* **600** 1771–9

[146]   Liu X, Zhou K, Wang L, Wang B and Li Y 2009 Oxygen Vacancy Clusters Promoting Reducibility and Activity of Ceria Nanorods *J. Am. Chem. Soc.* **131** 3140–1

[147]   Boronin A I, Slavinskaya E M, Danilova I G, Gulyaev R V, Amosov Y I, Kuznetsov P A, Polukhina I A, Koscheev S V, Zaikovskii V I and Noskov A S 2009 Investigation of palladium interaction with cerium oxide and its state in catalysts for low-temperature CO oxidation *Catal. Today* **144** 201–11

[148]   Nandi M and Talukdar A K 2016 Ceria–zirconia solid solution loaded hierarchical MFI zeolite: An efficient catalyst for solvent free oxidation of ethyl benzene *Arab. J. Chem.*

[149]   Bensalem A, Bozon-Verduraz F, Delamar M and Bugli G 1995 Preparation and characterization of highly dispersed silica-supported ceria *Appl. Catal. A Gen.* **121** 81–93

[150]   Zaytseva Y A, Panchenko V N, Simonov M N, Shutilov A A, Zenkovets G A, Renz M, Simakova I L and Parmon V N 2013 Effect of Gas Atmosphere on Catalytic Behaviour of Zirconia, Ceria and Ceria–Zirconia Catalysts in Valeric Acid Ketonization *Top. Catal.* **56** 846–55

[151]   Schwidder M, Kumar M S, Klementiev K, Pohl M M, Brückner A and Grünert W 2005 Selective reduction of NO with Fe-ZSM-5 catalysts of low Fe content: I. Relations between active site structure and catalytic performance *J. Catal.* **231** 314–30

[152]   Reddy A S, Chen C-Y, Chen C-C, Chien S-H, Lin C-J, Lin K-H, Chen C-L and Chang S-C 2010 Synthesis and characterization of Fe/CeO2 catalysts: Epoxidation of cyclohexene *J. Mol. Catal. A Chem.* **318** 60–7

[153]   Shimokawabe M, Asakawa H and Takezawa N 1990 Characterization of copper/zirconia catalysts prepared by an impregnation method *Appl. Catal.* **59** 45–58

[154]   Kappis K, Papadopoulos C, Papavasiliou J, Vakros J, Georgiou Y, Deligiannakis Y and Avgouropoulos G 2019 Tuning the Catalytic Properties of Copper-Promoted Nanoceria via a Hydrothermal Method *Catal.* **9**

[155]   Hai Z, Gao L, Zhang Q, Xu H, Cui D, Zhang Z, Tsoukalas D, Tang J, Yan S and Xue C 2016 Facile synthesis of core–shell structured PANI-Co3O4 nanocomposites with superior electrochemical performance in supercapacitors *Appl. Surf. Sci.* **361** 57–62

[156]   Deori K and Deka S 2013 Morphology oriented surfactant dependent CoO and reaction time dependent Co 3 O 4 nanocrystals from single synthesis method and their optical and magnetic properties *CrystEngComm* **15** 8465–74

[157]   Li, Yan Z F, Lu G Q and Zhu Z H 2006 Synthesis and Structure Characterization of Chromium Oxide Prepared by Solid Thermal Decomposition Reaction *J. Phys. Chem. B* **110** 178–83

[158]   Zhang L D, Mo C M, Cai W L and Chen G 1997 Characterizations of optical absorption in porous Al2O3/Cr2O3 nanocomposites *Nanostructured Mater.* **9** 563–6

[159]   Li X, Zhang X, Li Z and Qian Y 2006 Synthesis and characteristics of NiO nanoparticles by thermal decomposition of nickel dimethylglyoximate rods *Solid State Commun.* **137** 581–4

[160]   Adler D and Feinleib J 1970 Electrical and Optical Properties of Narrow-Band Materials *Phys. Rev. B* **2** 3112–34

[161]   Rives V and Kannan S 2000 Layered double hydroxides with the hydrotalcite-type structure containing Cu2+, Ni2+ and Al3+ *J. Mater. Chem.* **10** 489–95

[162]   Rao P V R, Kumar V P, Rao G S and Chary K V R 2012 Vapor phase selective hydrogenation of acetone to methyl isobutyl ketone (MIBK) over Ni/CeO 2 catalysts *Catal. Sci. Technol.* **2** 1665–73

[163]   Feio L S F, Hori C E, Mattos L V, Zanchet D, Noronha F B and Bueno J M C 2008 Partial oxidation and autothermal reforming of methane on Pd/CeO2–Al2O3 catalysts *Appl. Catal. A Gen.* **348** 183–92

[164]   Nagai Y, Yamamoto T, Tanaka T, Yoshida S, Nonaka T, Okamoto T, Suda A and Sugiura M 2002 X-ray absorption fine structure analysis of local structure of CeO2–ZrO2 mixed oxides with the same composition ratio (Ce/Zr=1) *Catal. Today* **74** 225–34

[165]   Kašpar J, Fornasiero P and Graziani M 1999 Use of CeO2-based oxides in the three-way catalysis *Catal. Today* **50** 285–98

[166]   Di Monte R and Kašpar J 2005 Heterogeneous environmental catalysis – a gentle art: CeO2–ZrO2 mixed oxides as a case history *Catal. Today* **100** 27–35

[167]   Zhang S-M, Huang W-P, Qiu X-H, Li B-Q, Zheng X-C and Wu S-H 2002 Comparative Study on Catalytic Properties for Low-Temperature CO Oxidation of Cu/CeO2 and CuO/CeO2 Prepared via Solvated Metal Atom Impregnation and Conventional Impregnation *Catal. Letters* **80** 41–6

[168]   Zhu H, Chen Y, Wang Z, Liu W and Wang L 2018 Catalytic oxidation of CO over mesoporous copper-doped ceria catalysts via a facile CTAB-assisted synthesis *RSC Adv.* **8** 14888–97

[169]   Luo M-F, Ma J-M, Lu J-Q, Song Y-P and Wang Y-J 2007 High-surface area CuO–CeO2 catalysts prepared by a surfactant-templated method for low-temperature CO oxidation *J. Catal.* **246** 52–9

[170]   YANG Z, MAO D, GUO X and LU G 2014 CO oxidation over CuO catalysts supported on CeO2-ZrO2 prepared by microwave-assisted co-precipitation: The influence of CuO content *J. Rare Earths* **32** 117–23

[171]   Enguo W and Songying C 2002 Structure and Catalytic Behavior of CuO-ZrO-CeO~ 2 Mixed Oxides *J. Rare Earths* **20** 533–7

[172]   Magnacca G, Cerrato G, Morterra C, Signoretto M, Somma F and Pinna F 2003 Structural and Surface Characterization of Pure and Sulfated Iron Oxides *Chem. Mater.* **15** 675–87

[173]   Wang J, Zhang B, Shen M, Wang J, Wang W, Ma J, Liu S and Jia L 2011 Effects of Fe-doping of ceria-based materials on their microstructural and dynamic oxygen storage and release properties *J. Sol-Gel Sci. Technol.* **58** 259–68

[174]   Nedyalkova R, Niznansky D and Roger A-C 2009 Iron–ceria–zirconia fluorite catalysts for methane selective oxidation to formaldehyde *Catal. Commun.* **10** 1875–80

[175]   WANG J, SHEN M, WANG J, GAO J, MA J and LIU S 2012 Effect of cobalt doping on ceria-zirconia mixed oxide: Structural characteristics, oxygen storage/release capacity and three-way catalytic performance *J. Rare Earths* **30** 878–83

[176]   Liotta L F, Pantaleo G, Carlo G Di, Marc G and Deganello G 2004 Structural and morphological investigation of a cobalt catalyst supported on alumina-baria : effects of redox treatments on the activity in the NO reduction by CO **52** 1–10

[177]   Yang P, Meng Z, Yang S, Shi Z and Zhou R 2014 Highly active behaviors of CeO2–CrOx mixed oxide catalysts in deep oxidation of 1,2-dichloroethane *J. Mol. Catal. A Chem.* **393** 75–83

[178]   Ma R, Hu P, Jin L, Wang Y, Lu J and Luo M 2011 Characterization of CrOx/Al2O3 catalysts for dichloromethane oxidation *Catal. Today* **175** 598–602

[179]   Yang P, Yang S, Shi Z, Tao F, Guo X and Zhou R 2016 Accelerating effect of ZrO2 doping on catalytic performance and thermal stability of CeO2–CrOx mixed oxide for 1,2-dichloroethane elimination *Chem. Eng. J.* **285** 544–53

[180]   Liu Y, Hayakawa T, Ishii T, Kumagai M, Yasuda H, Suzuki K, Hamakawa S and Murata K 2001 Methanol decomposition to synthesis gas at low temperature over palladium supported on ceria–zirconia solid solutions *Appl. Catal. A Gen.* **210** 301–14

[181]   Baidya T, Marimuthu A, Hegde M S, Ravishankar N and Madras G 2007 Higher Catalytic Activity of Nano-Ce1-x-yTixPdyO2-δ Compared to Nano-Ce1-xPdxO2-δ for CO Oxidation and N2O and NO Reduction by CO: Role of Oxide Ion Vacancy *J. Phys. Chem. C* **111** 830–9

[182]   Adams B D and Chen A 2011 The role of palladium in a hydrogen economy *Mater. Today* **14** 282–9

[183]   Priolkar K R, Bera P, Sarode P R, Hegde M S, Emura S, Kumashiro R and Lalla N P 2002 Formation of $Ce_{1-x}Pd_xO_{2-\delta}$ Solid Solution in Combustion-Synthesized Pd/CeO $_2$ Catalyst: XRD, XPS, and EXAFS Investigation *Chem. Mater.* **14** 2120–8

[184]   Anon, 7 million premature deaths annually linked to air pollution @ https://www.who.int/mediacentre/news/releases/2014/air-pollution/en/

[185]   Kampa M and Castanas E 2008 Human health effects of air pollution *Environ. Pollut.* **151** 362–7

[186]   Anon, Emissions of the main air pollutants in Europe — European Environment Agency @ https://www.eea.europa.eu/data-and-maps/indicators/main-anthropogenic-air-pollutant-emissions/assessment-4

[187]   Carslaw D C, Beevers S D, Tate J E, Westmoreland E J and Williams M L 2011 Recent evidence concerning higher NOx emissions from passenger cars and light duty vehicles *Atmos. Environ.* **45** 7053–63

[188]   Anon, EU action to curb air pollution by cars: Questions and Answers 2017 @ europa.eu

[189]   Baidya T, Marimuthu A, Hegde M S, Ravishankar N and Madras G 2007 Higher Catalytic Activity of Nano-Ce1-x-y Ti x Pd y O2-δ Compared to Nano-Ce1-x Pd x O2-δ for CO Oxidation and N2O and NO Reduction by CO: Role of Oxide Ion Vacancy *J. Phys. Chem. C* **111** 830–9

[190]   Granger P, Lamonier J F, Sergent N, Aboukais A, Leclercq L and Leclercq G 2001 Investigation of the intrinsic activity of ZrxCe1− xO2 mixed oxides in the CO+ NO reactions: influence of Pd incorporation *Top. Catal.* **16** 89–94

[191]   Dujardin C, Mamede A-S, Payen E, Sombret B, Huvenne J-P and Granger P 2004 Influence of the oxidation state of rhodium in three-way catalysts on their catalytic performances: an in situ FTIR and catalytic study *Top. Catal.* **30** 347–52

[192]   Granger P, Dujardin C, Paul J-F and Leclercq G 2005 An overview of kinetic and spectroscopic investigations on three-way catalysts: mechanistic aspects of the CO+ NO and CO+ N2O reactions *J. Mol. Catal. A Chem.* **228** 241–53

[193]   Granger P, Dhainaut F, Pietrzik S, Malfoy P, Mamede A-S, Leclercq L and Leclercq G 2006 An overview: Comparative kinetic behaviour of Pt, Rh and Pd in the NO+ CO and NO+ H 2 reactions *Top. Catal.* **39** 65–76

[194]   Vesecky S M, Rainer D R and Goodman D W 1996 Basis for the structure sensitivity of the CO+ NO reaction on palladium *J. Vac. Sci. Technol. A Vacuum, Surfaces, Film.* **14** 1457–63

[195]   Pisanu A M and Gigola C E 1999 NO decomposition and NO reduction by CO over Pd/α-Al2O3 *Appl. Catal. B Environ.* **20** 179–89

[196]   Rainer D R, Koranne M, Vesecky S M and Goodman D W 1997 CO + O2 and CO + NO Reactions over Pd/Al2O3 Catalysts *J. Phys. Chem. B* **101** 10769–74

[197]   Almusaiteer K A, Chuang S S C and Tan C-D 2000 Reactivity of Rh+(CO)2 during the NO–CO and CO–O2 Reactions over Rh/Al2O3 *J. Catal.* **189** 247–52

[198]   Chafik T, Kondarides D I and Verykios X E 2000 Catalytic Reduction of NO by CO over Rhodium Catalysts: 1. Adsorption and Displacement Characteristics Investigated by In Situ FTIR and Transient-MS Techniques *J. Catal.* **190** 446–59

[199]   Hecker W C and Bell A T 1983 Reduction of NO by CO over silica-supported rhodium: Infrared and kinetic studies *J. Catal.* **84** 200–15

[200]   Ertl G, Knözinger H and Weitkamp J 1999 *Environmental catalysis* (Wiley-VCH Weinheim)

[201]   Montini T, Melchionna M, Monai M and Fornasiero P 2016 Fundamentals and Catalytic Applications of CeO 2 - Based Materials

[202]   Ranga Rao G, Fornasiero P, Di Monte R, Kašpar J, Vlaic G, Balducci G, Meriani S, Gubitosa G, Cremona A and Graziani M 1996 Reduction of NO over partially reduced metal-loaded CeO2-ZrO2 solid solutions *J. Catal.* **162** 1–9

[203]   Taylor K C 1993 Nitric oxide catalysis in automotive exhaust systems *Catal. Rev. Eng.* **35** 457–81

[204]   Elhamdaoui A, Bergeret G, Massardier J, Primet M and Renouprez A 1994 CO and NO Interaction with Pd-Ag and Pd-Cr Bimetallic Catalysts .: 1. X-Ray-Diffraction, Infrared-Spectroscopy, and Thermoreaction *J. Catal.* **148** 47–55

[205]   Fernández-García M, Martínez-Arias A, Iglesias-Juez A, Hungría A B, Anderson J A, Conesa J C and Soria J 2003 Behavior of bimetallic Pd–Cr/Al2O3 and Pd–Cr/(Ce,Zr)Ox/Al2O3 catalysts for CO and NO elimination *J. Catal.* **214** 220–33

[206]   Fernández-Garcı&́a M, Martı&́nez-Arias A, Belver C, Anderson J A, Conesa J C and Soria J 2000 Behavior of palladium–copper catalysts for CO and NO elimination *J. Catal.* **190** 387–95

[207]   Fernandez-García M, Martínez-Arias A, Anderson J A, Conesa J C and Soria J 2000 CO and NO elimination over Pd-Cu catalysts *12th International Congress on Catalysis* vol 130, ed A Corma, F V Melo, S Mendioroz and J L G B T-S in S S and C Fierro (Elsevier) pp 1325–30

[208]   Hungría A B, Iglesias-Juez A, Martínez-Arias A, Fernández-García M, Anderson J A, Conesa J C and Soria J 2002 Effects of Copper on the Catalytic Properties of Bimetallic Pd–Cu/(Ce,Zr)Ox/Al2O3 and Pd–Cu/(Ce,Zr)Ox Catalysts for CO and NO Elimination *J. Catal.* **206** 281–94

[209]   Schmal M, Baldanza M A S and Vannice M A 1999 Pd-xMo/Al2O3 catalysts for NO reduction by CO *J. Catal.* **185** 138–51

[210] Trillat J F, Massardier J, Moraweck B, Praliaud H and Renouprez A J 1998 Reduction of NO by CO on Manganese promoted Palladium Catalysts *Catalysis and Automotive Pollution Control IV* vol 116, ed N Kruse, A Frennet and J-M B T-S in S S and C Bastin (Elsevier) pp 103–12

[211] Bradley J S, Via G H, Bonneviot L and Hill E W 1996 Infrared and EXAFS study of compositional effects in nanoscale colloidal palladium− copper alloys *Chem. Mater.* **8** 1895–903

[212] Yin Z, Gao D, Yao S, Zhao B, Cai F, Lin L, Tang P, Zhai P, Wang G, Ma D and Bao X 2016 Highly selective palladium-copper bimetallic electrocatalysts for the electrochemical reduction of CO2 to CO *Nano Energy* **27** 35–43

[213] Fernández-García M, Conesa J C, Clotet A, Ricart J M, López N and Illas F 1998 Study of the Heterometallic Bond Nature in PdCu(111) Surfaces *J. Phys. Chem. B* **102** 141–7

[214] Zhang L, Filot I A W, Su Y-Q, Liu J-X and Hensen E J M 2018 Transition metal doping of Pd(111) for the NO + CO reaction *J. Catal.* **363** 154–63

[215] Neitzel A, Figueroba A, Lykhach Y, Skála T, Vorokhta M, Tsud N, Mehl S, Ševčíková K, Prince K C, Neyman K M, Matolín V and Libuda J 2016 Atomically Dispersed Pd, Ni, and Pt Species in Ceria-Based Catalysts: Principal Differences in Stability and Reactivity *J. Phys. Chem. C* **120** 9852–62

[216] Gabasch H, Unterberger W, Hayek K, Klötzer B, Kleimenov E, Teschner D, Zafeiratos S, Hävecker M, Knop-Gericke A, Schlögl R, Han J, Ribeiro F H, Aszalos-Kiss B, Curtin T and Zemlyanov D 2006 In situ XPS study of Pd(111) oxidation at elevated pressure, Part 2: Palladium oxidation in the 10−1mbar range *Surf. Sci.* **600** 2980–9

[217] Kurnatowska M, Kepinski L and Mista W 2012 Structure evolution of nanocrystalline Ce1−xPdxO2−y mixed oxide in oxidizing and reducing atmosphere: Reduction-induced activity in low-temperature CO oxidation *Appl. Catal. B Environ.* **117**–**118** 135–47

[218] Du C, Lu G, Guo Y, Guo Y and Gong X 2016 Surfactant-Mediated One-Pot Method To Prepare Pd–CeO2 Colloidal Assembled Spheres and Their Enhanced Catalytic Performance for CO Oxidation *ACS Omega* **1** 118–26

[219] Zhou Y, Lawrence N J, Wu T, Liu J, Kent P, Soo Y and Cheung C L 2014 Pd/CeO2− x Nanorod catalysts for CO oxidation: insights into the origin of their regenerative ability at room temperature *ChemCatChem* **6** 2937–46

[220] Ali M A, Kimura T, Suzuki Y, Al-Saleh M A, Hamid H and Inui T 2002 Hydrogen spillover phenomenon in noble metal modified clay-based hydrocracking catalysts *Appl. Catal. A Gen.* **227** 63–72

[221] Prins R 2012 Hydrogen Spillover. Facts and Fiction *Chem. Rev.* **112** 2714–38

[222] Su Y-Q, Liu J-X, Filot I A W, Zhang L and Hensen E J M 2018 Highly Active and Stable CH4 Oxidation by Substitution of Ce4+ by Two Pd2+ Ions in CeO2(111) *ACS Catal.* **8** 6552–9

[223] Xu J, Ouyang L, Mao W, Yang X-J, Xu X-C, Su J-J, Zhuang T-Z, Li H and Han Y-F 2012 Operando and Kinetic Study of Low-Temperature, Lean-Burn Methane Combustion over a Pd/γ-Al2O3 Catalyst *ACS Catal.* **2** 261–9

[224] Meng L, Jia A-P, Lu J-Q, Luo L-F, Huang W-X and Luo M-F 2011 Synergetic Effects of PdO Species on CO Oxidation over PdO–CeO2 Catalysts *J. Phys. Chem. C* **115** 19789–96

[225] Pykavy M, Staemmler V, Seiferth O and Freund H-J 2001 Adsorption of CO on Cr2O3(0001) *Surf. Sci.* **479** 11–25

[226] Ma L, Luo M-F and Chen S-Y 2003 Redox behavior and catalytic properties of CuO/Ce0.8Zr0.2O2 catalysts *Appl. Catal. A Gen.* **242** 151–9

[227]   Hu Y, Dong L, Shen M, Liu D, Wang J, Ding W and Chen Y 2001 Influence of supports on the activities of copper oxide species in the low-temperature NO+CO reaction *Appl. Catal. B Environ.* **31** 61–9

[228]   Liotta L F, Pantaleo G, Di Carlo G, Marcì G and Deganello G 2004 Structural and morphological investigation of a cobalt catalyst supported on alumina-baria: effects of redox treatments on the activity in the NO reduction by CO *Appl. Catal. B Environ.* **52** 1–10

[229]   Savereide L, Nauert S L, Roberts C A and Notestein J M 2018 The effect of support morphology on CoOX/CeO2 catalysts for the reduction of NO by CO *J. Catal.* **366** 150–8

[230]   Zhang S, Li Y, Huang J, Lee J, Kim D H, Frenkel A I and Kim T 2019 Effects of Molecular and Electronic Structures in CoOx/CeO2 Catalysts on NO Reduction by CO *J. Phys. Chem. C* **123** 7166–77

[231]   Chen J, Zhan Y, Zhu J, Chen C, Lin X and Zheng Q 2010 The synergetic mechanism between copper species and ceria in NO abatement over Cu/CeO2 catalysts *Appl. Catal. A Gen.* **377** 121–7

[232]   Martínez-Arias A, Fernández-García M, Iglesias-Juez A, Hungría A B, Anderson J A, Conesa J C and Soria J 2001 New Pd/CexZr1−xO2/Al2O3 three-way catalysts prepared by microemulsion: Part 2. In situ analysis of CO oxidation and NO reduction under stoichiometric CO+NO+O2 *Appl. Catal. B Environ.* **31** 51−60

[233]   Song W, Su Y and Hensen E J M 2015 A DFT Study of CO Oxidation at the Pd–CeO2(110) Interface *J. Phys. Chem. C* **119** 27505–11

[234]   Cargnello M, Doan-Nguyen V V T, Gordon T R, Diaz R E, Stach E A, Gorte R J, Fornasiero P and Murray C B 2013 Control of metal nanocrystal size reveals metal-support interface role for ceria catalysts *Science (80-.).* **341** 771–3

[235]   Chen Y, Chen J, Qu W, George C, Aouine M, Vernoux P and Tang X 2018 Well-defined palladium–ceria interfacial electronic effects trigger CO oxidation *Chem. Commun.* **54** 10140–3

[236]   Priolkar K R, Bera P, Sarode P R, Hegde M S, Emura S, Kumashiro R and Lalla N P 2002 Formation of Ce1-xPdxO2-δ Solid Solution in Combustion-Synthesized Pd/CeO2 Catalyst: XRD, XPS, and EXAFS Investigation *Chem. Mater.* **14** 2120–8

[237]   Hegde M S, Madras G and Patil K C 2009 Noble Metal Ionic Catalysts

[238]   Baidya T, Dutta G, S Hegde M and Waghmare U 2009 *Noble metal ionic catalysts: Correlation of increase in CO oxidation activity with increasing effective charge on Pd ion in Pd ion substituted Ce1−xMxO2−Δ (M = Ti, Zr and Hf)* vol 3

[239]   Roberts C A, Prieto-Centurion D, Nagai Y, Nishimura Y F, Desautels R D, van Lierop J, Fanson P T and Notestein J M 2015 In Situ Characterization of Highly Dispersed, Ceria-Supported Fe Sites for NO Reduction by CO *J. Phys. Chem. C* **119** 4224–34

[240]   Perez-Alonso F J, Melián-Cabrera I, López Granados M, Kapteijn F and Fierro J L G 2006 Synergy of FexCe1−xO2 mixed oxides for N2O decomposition *J. Catal.* **239** 340–6

[241]   Di Monte R, Fornasiero P, Kašpar J, Rumori P, Gubitosa G and Graziani M 2000 Pd/Ce0.6Zr0.4O2/Al2O3 as advanced materials for three-way catalysts: Part 1. Catalyst characterisation, thermal stability and catalytic activity in the reduction of NO by CO *Appl. Catal. B Environ.* **24** 157–67

[242]   Chen X, Lyu Y, Nwabara U and Schwank J W 2019 Reactivity study of CO+NO reaction over Pd/Al2O3 and Pd/CeZrO2 catalysts *Catal. Today* **323** 148–58

[243]   Jansson J, Skoglundh M, Fridell E and Thormählen P 2001 A mechanistic study of low temperature CO oxidation over cobalt oxide *Top. Catal.* **16** 385–9

[244]   Jansson J, Palmqvist A E C, Fridell E, Skoglundh M, Österlund L, Thormählen P and Langer V 2002 On the Catalytic Activity of Co3O4 in Low-Temperature CO Oxidation *J. Catal.* **211** 387–97

[245]   Lukashuk L, Föttinger K, Kolar E, Rameshan C, Teschner D, Hävecker M, Knop-Gericke A, Yigit N, Li H, McDermott E, Stöger-Pollach M and Rupprechter G 2016 Operando XAS and NAP-XPS studies of preferential CO oxidation on Co3O4 and CeO2-Co3O4 catalysts *J. Catal.* **344** 1–15

[246]   Wan H, Wang Z, Zhu J, Li X, Liu B, Gao F, Dong L and Chen Y 2008 Influence of CO pretreatment on the activities of CuO/γ-Al2O3 catalysts in CO+ O2 reaction *Appl. Catal. B Environ.* **79** 254–61

[247]   Zeng S, Bai X, Wang X, Yu W and Liu Y 2006 Valence state of active copper in CuOx/CeO2 catalysts for CO oxidation *J. Rare Earths* **24** 177–81

[248]   Teoh W Y, Amal R and Mädler L 2010 Flame spray pyrolysis: An enabling technology for nanoparticles design and fabrication *Nanoscale* **2** 1324–47

[249]   Miki T, Ogawa T, Haneda M, Kakuta N, Ueno A, Tateishi S, Matsuura S and Sato M 1990 Enhanced oxygen storage capacity of cerium oxides in cerium dioxide/lanthanum sesquioxide/alumina containing precious metals *J. Phys. Chem.* **94** 6464–7

[250]   Martínez-Arias A, Fernández-García M, Salamanca L N, Valenzuela R X, Conesa J C and Soria J 2000 Structural and Redox Properties of Ceria in Alumina-Supported Ceria Catalyst Supports *J. Phys. Chem. B* **104** 4038–46

[251]   Bera P, Patil K C, Jayaram V, Subbanna G N and Hegde M S 2000 Ionic dispersion of Pt and Pd on CeO2by combustion method: Effect of metal-ceria interaction on catalytic activities for NO reduction and CO and hydrocarbon oxidation *J. Catal.* **196** 293–301

[252]   Vayssilov G N, Lykhach Y, Migani A, Staudt T, Petrova G P, Tsud N, Skála T, Bruix A, Illas F, Prince K C, Matolı́n V, Neyman K M and Libuda J 2011 Support nanostructure boosts oxygen transfer to catalytically active platinum nanoparticles *Nat. Mater.* **10** 310

[253]   Pacchioni G 2013 Electronic interactions and charge transfers of metal atoms and clusters on oxide surfaces *Phys. Chem. Chem. Phys.* **15** 1737–57

[254]   Liu L and Corma A 2018 Metal Catalysts for Heterogeneous Catalysis: From Single Atoms to Nanoclusters and Nanoparticles *Chem. Rev.* **118** 4981–5079

[255]   Harrison P G, Allison F J and Daniell W 2002 Effect of Preparation Route and Thermal Treatment on the Nature of Copper and Chromium Doubly Promoted Ceria Catalysts *Chem. Mater.* **14** 499–507

[256]   Yoshida H, Yamashita N, Ijichi S, Okabe Y, Misumi S, Hinokuma S and Machida M 2015 A Thermally Stable Cr–Cu Nanostructure Embedded in the CeO2 Surface as a Substitute for Platinum-Group Metal Catalysts *ACS Catal.* **5** 6738–47